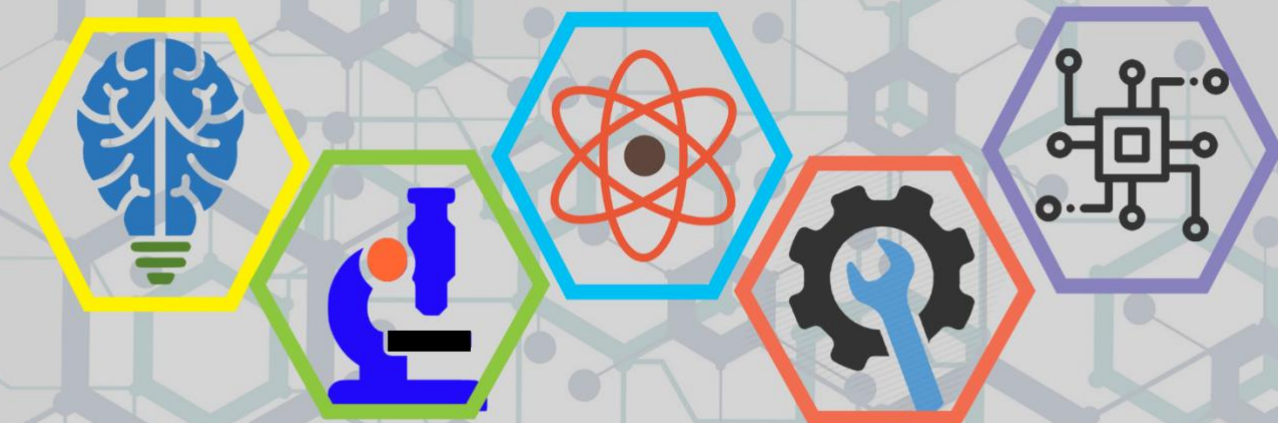


ISSN: 2687-2153

IJEIR

International Journal of Engineering & Innovative Research



Volume: 5 Issue: 2

International Journal of Engineering and Innovative Research (IJEIR)

Year: 2023

Volume: 5

Issue: 2

Editor in Chief

Assoc. Dr. Ahmet Ali SÜZEN
Isparta University of Applied Sciences

Asst. Prof. Dr. Burhan DUMAN
Isparta University of Applied Sciences

Editorial Board Secretaries

Osman Can ÇETLENBİK
Isparta University of Applied Sciences

Correspondence Address

International Journal of Engineering and Innovative Research (IJEIR)
Secretaries Office
Isparta University of Applied Sciences
Isparta / Turkey

Phone and e-mail

Tel: +90 0246 211 08 68

E-mail: ijeirturkey@gmail.com

e-ISSN: 2687-2153

International Journal of Engineering and Innovative Research (IJEIR)

Year: 2023

Volume: 5

Issue: 2

Editorial Board

Prof. Dr. Narita Md Norwawi Universiti Sains Islam Malaysia University- MALAYSIAN
Prof. Dr. Shivam Mishra Dr. A.P.J. Abdul Kalam Technical University- INDIA
Assoc. Dr. Melda Alkan ÇAKIROĞLU Applied Sciences University of Isparta – TURKEY
Asst. Prof. Dr. Ali Nadi KAPLAN Applied Sciences University of Isparta – TURKEY
Asst. Prof. Dr. Özdemir Deniz, Applied Sciences University of Isparta – TURKEY
Dr. Remzi Gürfidan, Applied Sciences University of Isparta – TURKEY

Advisory Board

Prof. Dr. Kamaruzzaman Seman Universiti Sains Islam Malaysia University- MALAYSIAN
Prof. Dr. David HUI University of New Orleans- USA
Prof. Dr. Vladimir Jotsov University of Library Studies and IT - BULGARIA
Assoc. Prof Dr. Madihah MOHD SAUDI Universiti Sains Islam Malaysia - MALAYSIAN
Assoc. Prof Dr. Azni Haslizan Ab Halim Universiti Sains Islam Malaysia - MALAYSIAN
Asst. Prof. Dr. Ali Dinç American University of Middle East - KUWAIT
Dr. Fotis Kokkoras Technological Educational Inst. of Thessaly – GREECE

Reviewers for this issue

Abdullah GENÇ
Adem DALCALI
Bekir AKSOY
Burhan DUMAN
Erman ERKAN
Fatih Ahmet ŞENEL
Gürçan ÇETİN
Özlem ŞENGÖZ ŞİRİN
Sinan Uğuz

Kadri AKÇALI
Kamil DELİKANLI
Mahmut Ahmet GÖZEL
Seyit AKPANCAR
Olimjon TOİROV
Osman Özkaraca
Orhan ARMAĞAN
Şükrü ÖZEN

International Journal of Engineering and Innovative Research (IJEIR)

Year: 2023

Volume: 5

Issue: 2

CONTENTS

PAGE

Research Articles

TUNABLE RADIO FREQUENCY (RF) RECEIVER (RX) INTEGRATED CIRCUIT (IC)

Özgür KAZANCI, Okan ORAL..... 90-94

OPTIMUM SIGNALIZATION ALGORITHM SUGGESTION WITH THE INTERSECTION DELAY OPTIMIZATION

Abdülkadir Çıldır, Mesud Kahriman, Mesut Tığdemir.....95-103

EVALUATION OF WHOLE BODY VIBRATION IN WEAVING FACTORY

Murat KODALOĞLU, Feyza AKARSLAN KODALOĞLU.....104-111

UTILIZING DEEP LEARNING AND DATA AUGMENTATION FOR EARLY DETECTION OF EYE DISEASES IN PETS

Nilgün Şengöz112-122

Designing a Solar PV–Battery based on Electric Vehicle Charging Station

Samatar ABDI YONIS, Ziyodulla YUSUPOV, Muhammet Tahir GÜNEŞER.....123-136

THERMAL BEHAVIOR OF DIFFERENT FLUIDS IN ELECTROMAGNETIC INDUCTION

Mustafa ÇATAK, Tuncay AYDOĞAN, RamazanSELVER.....137-149

BROAD PHASE RESPONSE UNIT CELL AND HIGH GAIN REFLECTARRAY ANTENNA DESIGN WITH CIRCLE-MINKOWSKI STRUCTURES

Samet Yalçın, Tuna GÖKSU, Selami KESLER, Okan BİNGÖL150-160

BI-DIRECTIONAL CLASSIFICATION OF ROMAN PERIOD COINS BY DEEP LEARNING METHODS

Kıyas KAYAALP, Fehmi ÖZKANER.....161-169

Review

EXAMINING THE IMPORTANCE OF ARTIFICIAL INTELLIGENCE IN THE SINGULARIZATION OF BIG DATA WITH THE DEVELOPMENT OF CLOUD COMPUTING

Serkan KESKİN, Ali Hakan IŞIK170-180



Research Article

TUNABLE RADIO FREQUENCY (RF) RECEIVER (RX) INTEGRATED CIRCUIT (IC)

Authors: Özgür Kazancı , Okan ORAL 

To cite to this article: Kazancı, Ö., Oral, O., (2023). TUNABLE RADIO FREQUENCY (RF) RECEIVER (RX) INTEGRATED CIRCUIT (IC). International Journal of Engineering and Innovative Research , 5(2), p:90-94 . DOI: 10.47933/ijeir.1156769

DOI: 10.47933/ijeir.1156769

To link to this article: <https://dergipark.org.tr/tr/pub/ijeir/archive>



TUNABLE RADIO FREQUENCY (RF) RECEIVER (RX) INTEGRATED CIRCUIT (IC)

Özgür Kazancı¹ , Okan ORAL^{2*} 

¹Akdeniz University, Engineering Faculty, Department of Biomedical Engineering, Antalya, Türkiye.

²Akdeniz University, Engineering Faculty, Department of Mechatronics Engineering, Antalya, Türkiye.

*Corresponding Author: okan@akdeniz.edu.tr
(Received: 05.08.2022; Accepted: 07.02.2023)

<https://doi.org/10.47933/ijeir.1156769>

ABSTRACT: In this work tunable radio frequency (RF) receiver (Rx) integrated circuit (IC) was demonstrated. TSMC 65 nm technology node was selected to implement IC. RF technique has some advantages over biomedical optic molecule investigation methods since it is easy to design, implement. Experimental measurement on live tissue is much easier than optic methods. Nanoscopic creatures have specific binding structures. Their elements construct their shapes and neighborhood conformation between their own atoms. Based on this work differential RF waves will be used to investigate the nanoscopic creatures. Since the investigation of nanoscopic creatures will require to use electromagnetic wave phase shift and scan of different RF frequencies, ultra-wide band (UWB) tunable receiver circuit topology was designed and simulated. For this purpose, Rx block was designed, and simulation work was demonstrated here. In the circuit simulations, off-chip antenna was connected to the low-noise amplifier (LNA) circuit. Specific frequency was around 30 GHz. Frequency tuning was adjusted by changing the source and bias voltages at the active inductor voltage-controlled oscillator (VCO) circuit block. The same VCO block was also used at the Tx circuit before. Antenna signal was modeled by using 33 GHz alternative sinusoidal signal. Antenna signal and 30 GHz active-inductor VCO voltage output were mixed at the mixer circuit block, 3 GHz envelope signal was extracted in this work. Layout implementation of Rx receiver IC was demonstrated.

Keywords: Biomedical diagnosis, Tunable RF Receiver (Rx), Integrated Circuit (IC), Transceiver.

1. INTRODUCTION

Novel inventions are necessary to scan and investigate possible virus threats such as Co-Vid19 virus by using non-invasive methods. Existing biomedical optic and photonic methods require to syringe blood samples from live organism and then scan process is taking long time. It has also high spread risk to the environment. Emerging non-invasive technological tools are necessary. Radio frequency (RF) method might be easy to setup and measure device tool since the emerging microelectronic technology can give us design, implement, apply, and observe opportunity very quickly. For this purpose, new tunable RF receiver integrated circuit (IC) was designed, and simulation waveform output was shown. Since RF receiver is tunable, it has novelty over traditional receiver RF circuits. The circuit gives us an opportunity to be able to scan different frequencies. Researchers demonstrated us one possible RF application methodology to detect some well-known microbial instances at around 10 GHz source signal frequency [1]. They used waveguide and applied around 10 GHz frequency source signal, they observed frequency versus temperature change depend on the virus existence. They show us RF signals can interact and depend on the nanoscopic creatures' atomic shape back reflected or

transmitted RF signal intensity, frequency and phase might be shifted. Based on this knowledge, emerging microelectronic RF integrated circuit (IC) technologies can be used. With the help of emerging microelectronic RF IC technology, ICs would be designed and developed. Transmitter (Tx) and receiver (Rx) circuit blocks are thought to be applied to live-tissue non-invasively. For this purpose, receiver (Rx) RF IC circuit schematic block was designed and simulated at this work. Different virus and bacterial identification and destruction studies were done by using RF and terahertz (THz) techniques [2-7]. RF resonance method was used to destroy the virus [2]. THz technique was used to detect virus [3]. SARS-CoV-2 virus inactivation by using electromagnetic waves at the resonance frequencies was tested [4]. THz metamaterials were used to detect viruses [5]. 95 GHz millimeter wave exposure was used to kill coronavirus 229E, and poliovirus [6]. DNA and RNA viruses' resonance with millimeter waves was summarized in review article [7]. The philosophy like on differential photon waves imaging philosophy [2] will also be applied for RF signals. Differential photon waves imaging relies based on the sequential wave interactions with the interested nanoscopic creature. Nanoscopic creatures' atomic sizes and binding distances with each other neighbor atom can be linked with the sequential waves. Nanometric wave differences can be linked with the nanoscopic creatures' physical shape and binding distances. This natural relation can help to investigate the interested nanoscopic creature by sending time resolved sequential waves into live tissue. According to the paper [2] which explains the differential photon waves imaging philosophy, 26 nanometers (nm) phase shift can be realized by generating almost 14 attoseconds time delay. For example, let us say in a homogeneous environment, if 2 sequential waves were sent through live tissue from source position with the 14 attosecond (as) delay, and then if non-of them can reach to the detector position, it would be said that there exists specific creature. In the future, instead of using differential photon waves, it is aimed to use differential RF waves. For this purpose, receiver Rx RF IC block was designed and simulated in this work. Ka electromagnetic wave band spectrum was selected which mostly focused on 30 GHz and around it.

2. METHODS

The whole Rx circuit consists of off-chip antenna, impedance matching network (IMN) I, low-noise amplifier (LNA), IMN II, active inductor voltage-controlled oscillator (VCO), Mixer, IMN III, and output stage. The active inductor was studied [9]. The active inductor schematic was designed and simulated based on the literature work [10]. components and their values were selected appropriately. In the literature, there are also other active inductor analyses and design studies [11-14]. Low noise amplifier (LNA) designs were demonstrated for TSMC 65 nm technology node in the literature [15, 16]. 24-30 GHz band LNA schematic was also proposed in the literature [17]. LNA was designed according to the single stage common source double nMOS transistor structure like in the literature work [18] except transformer and separately second nMOS driver transistor was diode connected. The mixer designed according to the balanced Gilbert mixer cell topology [19].

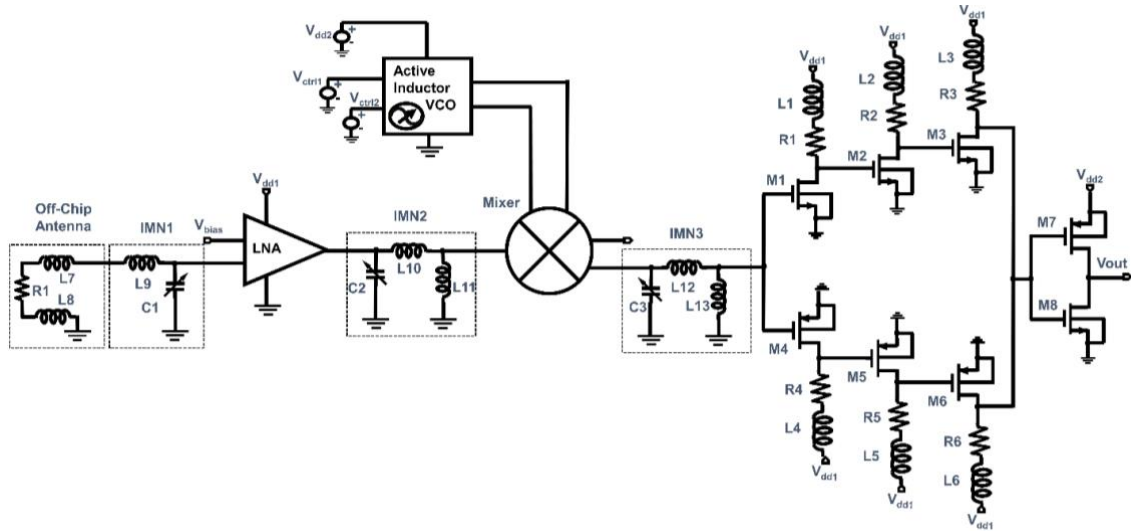


Figure 1. The receiver (Rx) circuit topology.

The whole Rx schematic circuit is shown in Figure 1. Impedance matching networks (IMNs) were added between each block. Totally 3 IMNs were added to the Rx circuit. 30 GHz Active inductor voltage output signals were generated by adjusting the control bias voltages. 33 GHz antenna signal was applied. Both antenna and active inductor VCO signal were mixed at the mixer circuit and 3 GHz envelope signal was extracted.

2. DISCUSSION AND RESULT

Simulation result was shown in Figure 2. Envelope signal is demonstrated in the Figure 2. Different control bias voltages were applied to the active inductor, by this way different VCO frequencies were generated and applied to the mixer circuit then envelope signals were extracted correctly.

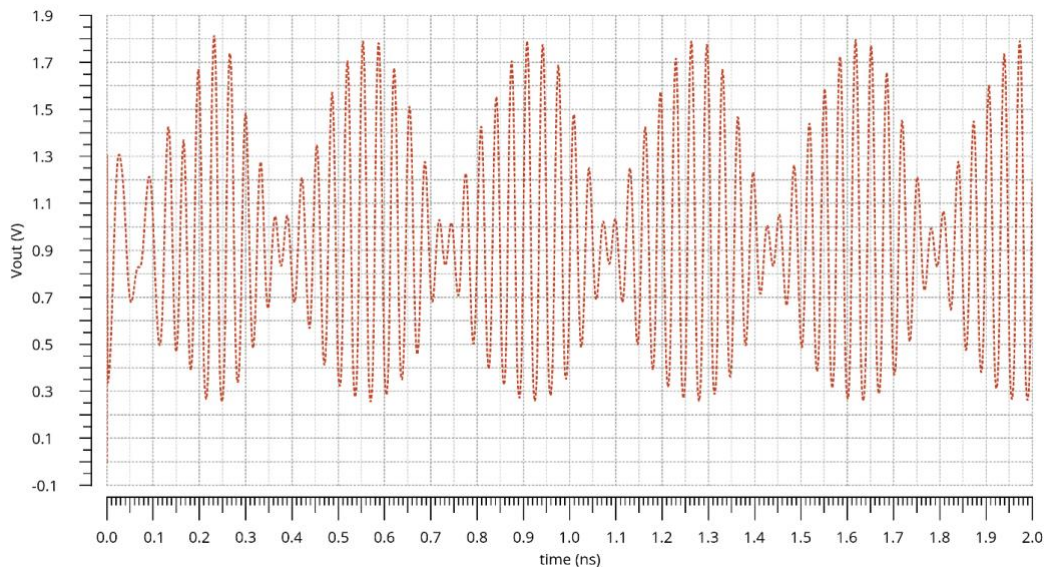


Figure 2. Extracted 3 GHz envelope signal voltage output.

In this work, Ka-band RF integrated receiver Rx circuit was designed, analyzed, and implemented at the TSMC 65 nm technology node. All processes include simulation, design rule check (DRC), electrical rule check (ERC), and layout-versus-schematic (LVS) were done

successfully. Antenna signal was modeled as 33 GHz RF signal. It was simulated that there is off-chip antenna, and this off-chip antenna is receiving 33 GHz RF signal. At the receiving side 30 GHz active inductor voltage-controlled oscillator (VCO) circuit is generating mixer input signal. This active inductor has tunable oscillator input control voltages: v_{ctrl1} , v_{ctrl2} , v_{dd1} . By changing the oscillator control voltages, it is possible to change the 30 GHz frequency output. In this work, for the simplicity 30 GHz signal frequency was generated and connected to Gilbert-cell mixer input. The other mixer cell input is the 33 GHz antenna signal. On the mixer circuit, these two different signals were mixed then finally 3 GHz envelope signal as an output waveform was extracted successfully. In the test and measurement setup it is aimed to tune 30 GHz active inductor signal frequency. By changing the 30 GHz signal frequency, mixer output envelope signal frequencies are changed. By using this method, it will be possible to detect the nanoscopic or microscopic creatures on transmission through geometry. On one side of the tissue specimen, 33 GHz transmitting source signal will be placed, on the other side of specimen receiving circuit will be placed. Similar studies were done in the literature. A 30–40 GHz CMOS receiver circuit which has high conversion gain was designed and implemented [20]. A 60 GHz CMOS receiver circuit was designed and implemented [21]. There is no tunable RF receiver in literature as in our study. We can change oscillator output frequency which is around 30 GHz. By changing the control voltages, we generate different oscillator frequencies than 30 GHz. By mixing the received signal with tunable oscillator frequency, different output envelope signal can be extracted.

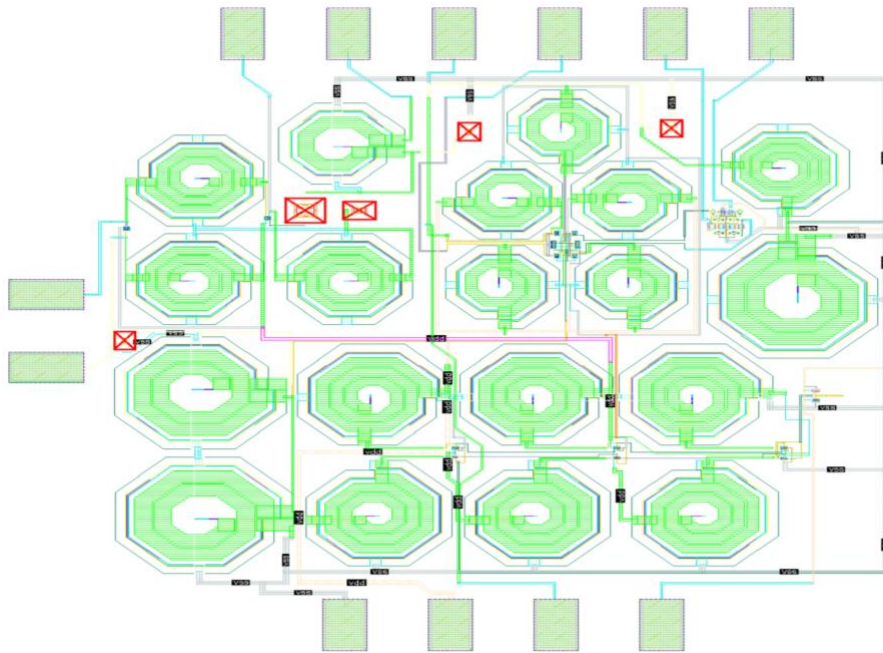


Figure 3. Layout implementation of Rx receiver IC.

4. CONCLUSIONS

Rx RF IC circuit was designed and simulated at this work for future differential wave imaging usage. Required circuit blocks were designed and connected appropriately. Off-chip antenna and wire bonding were modeled. Off-chip antenna was connected to the LNA circuit. Active inductor voltage-controlled oscillator (VCO) circuit generated 30 GHz frequency signal for demonstration purpose. Frequency tuning was adjusted by changing the source and bias voltages at the active inductor voltage-controlled oscillator (VCO) circuit block. The same VCO block was also used at the Tx circuit. Antenna signal was modeled by using 33 GHz

alternative sinusoidal signal. Antenna signal and 30 GHz active-inductor VCO signal were mixed at the mixer circuit block and 3 GHz envelope signal was extracted and demonstrated in this work. The layout implementation of Rx Ic was demonstrated in Figure 3. The receiver circuit was implemented based on to realize the 3 GHz envelope signal which was demonstrated in the Figure 2. 30 GHz, active-inductor VCO signal was generated. The mixer circuit was designed according to the balanced Gilbert mixer cell topology. Extracted 3 GHz envelope signal is demonstrating important signal output. On layout, 12 I/O pads were placed around circuit borders. These signals are: vdd1, vdd2, vctrl1, vctrl2, vbias, vout. GDSII file format circuit layout was demonstrated in Figure 3. Inductors are spiral inductors and capacitors are mimCap capacitors. PADs were designed from metal1 to metal9.

REFERENCES

1. Al Ahmad, M., & Rizvi, T. A. (2016, August). Virus detection by monitoring its radio frequency response versus temperature. *In 2016 Progress in Electromagnetic Research Symposium (PIERS)*, 4649-4655. IEEE.
2. Meessen, A. (2020). Virus Destruction by Resonance. *Journal of Modern Physics*, 11(12), 2011.
3. Di Fabrizio, M., Lupi, S., & D'Arco, A. (2021). Virus recognition with terahertz radiation: drawbacks and potentialities. *Journal of Physics: Photonics*, 3(3), 032001.
4. Calabrò, E., & Magazù, S. (2021). Viruses Inactivation Induced by Electromagnetic Radiation at Resonance Frequencies: Possible Application on SARS-CoV-2. *World*, 10(1), 1-4.
5. Park, S. J., Cha, S. H., Shin, G. A., & Ahn, Y. H. (2017). Sensing viruses using terahertz nano-gap metamaterials. *Biomedical optics express*, 8(8), 3551-3558.
6. Kaczmarczyk, L. S., Marsay, K. S., Shevchenko, S., Pilosof, M., Levi, N., Einat, M., Oren, M., & Gerlitz, G. (2021). Corona and polio viruses are sensitive to short pulses of W-band gyrotron radiation. *Environmental Chemistry Letters*, 19(6), 3967-3972.
7. Ikhlov, B. L. (2022). On the effect of millimeter waves on DNA and RNA of viruses. *International Journal of Clinical Virology*, 6(2), 029-033.
8. Kazancı, H. O. (2021). Differential photon waves imaging. *International Journal of Imaging Systems and Technology*, 31(2), 718-728.
9. Razavi, B. (2020). The active inductor [A circuit for all seasons]. *IEEE Solid-State Circuits Magazine*, 12(2), 7-11.
10. Lu, L. H., Hsieh, H. H., & Liao, Y. T. (2006). A wide tuning-range CMOS VCO with a differential tunable active inductor. *IEEE Transactions on Microwave Theory and Techniques*, 54(9), 3462-3468.
11. Cheng, K. H., Hung, C. L., Gong, C. S. A., Liu, J. C., Jiang, B. Q., & Sun, S. Y. (2014). A 0.9-to 8-GHz VCO with a differential active inductor for multistandard wireline SerDes. *IEEE Transactions on Circuits and Systems II: Express Briefs*, 61(8), 559-563.
12. Fillaud, M., & Barthélemy, H. (2008, June). Design of a wide tuning range VCO using an active inductor. *In 2008 Joint 6th International IEEE Northeast Workshop on Circuits and Systems and TAIASA Conference* (pp. 13-16). IEEE.
13. Reja, M. M., Filanovsky, I. M., & Moez, K. (2008). Wide tunable CMOS active inductor. *Electronics Letters*, 44(25), 1461-1463.
14. Kao, H. L., Lee, P. C., & Chiu, H. C. (2015). A wide tuning-range CMOS VCO with a tunable active inductor. *Mathematical Problems in Engineering*, 2015.
15. J. Xu, J., Yan, N., Chen, Q., Gao, J., & Zeng, X. (2013, May). A 3.4 dB NF k-band LNA in 65nm CMOS technology. *In 2013 IEEE International Symposium on Circuits and Systems (ISCAS)*, (pp. 1123-1126). IEEE.
16. Wu, Y. Y., Jin, J., & El-Sankary, K. (2017, December). A linearized wideband low noise amplifier in 65nm CMOS for multi-standard RF communication applications. *In 2017 3rd IEEE International Conference on Computer and Communications (ICCC)*, (pp. 812-815). IEEE.
17. Zhou, J., Zhang, X., Yu, Y., Zhang, L., Zhao, C., Liu, H., & Kang, K. (2018, May). A 24–30 GHz CMOS LNA with 2.05 dB NF and 0.6 dB in-band gain ripple for 5G-applications. *In 2018 IEEE MTT-S International Wireless Symposium (IWS)*, (pp. 1-3). IEEE.
18. Feng, Y., Takemura, G., Kawaguchi, S., & Kinget, P. (2008, June). A high performance 2-GHz direct-conversion front end with single-ended RF input in 0.13 um CMOS. *In 2008 IEEE Radio Frequency Integrated Circuits Symposium* (pp. 339-342). IEEE.
19. Bekkaoui, M. O. (2017, April). Gilbert cell Mixer design in 65nm CMOS technology. *In 2017 4th International Conference on Electrical and Electronic Engineering (ICEEE)*, (pp. 67-72). IEEE.



Research Article

OPTIMUM SIGNALIZATION ALGORITHM SUGGESTION WITH THE INTERSECTION DELAY OPTIMIZATION

Authors: Abdülkadir ıldır , Mesud Kahriman , Mesut Tiğdemir 

To cite to this article: ıldır, A., Kahriman, M., Tiğdemir, M., (2023). OPTIMUM SIGNALIZATION ALGORITHM SUGGESTION WITH THE INTERSECTION DELAY OPTIMIZATION. International Journal of Engineering and Innovative Research , 5(2), p:95-103 . DOI: 10.47933/ijeir.1189981

DOI: 10.47933/ijeir.1189981

To link to this article: <https://dergipark.org.tr/tr/pub/ijeir/archive>



International Journal of Engineering and Innovative Research

<http://dergipark.gov.tr/ijeir>

OPTIMUM SIGNALIZATION ALGORITHM SUGGESTION WITH THE INTERSECTION DELAY OPTIMIZATION

Abdülkadir Çıldır^{1*}, Mesud Kahrıman², Mesut Tığdemir³

¹Trakya University, Vocational College of Technical Sciences, Department of Electronic and Automation, Edirne, Turkey.

²Suleyman Demirel University, Faculty of Engineering, Department of Electrical-Electronics, Isparta, Turkey.

³Suleyman Demirel University, Faculty of Engineering, Department of Civil, Isparta, Turkey.

*Corresponding Author: abdulkadircildir@trakya.edu.tr
(Received: 16.10.2022; Accepted: 21.02.2023)

<https://doi.org/10.47933/ijeir.1189981>

ABSTRACT: In this study, a sample has been carried out in order to discharge the current vehicle flow in minimum time at the intersection. The sample has been carried out at an isolated and lossless four-legged intersection. An ideal traffic signaling algorithm have been presented by simultaneously calculating the minimum total intersection delay at this intersection. The suggested algorithm that is actuated method have been compared with classical and different actuated methods. It has been observed that the presented algorithm reduces the intersection delay by 65 % compared to the classical method and 51 % compared to some actuated methods.

Keywords: Isolated and lossless intersection, intersection delay, actuated method, optimum traffic signalization.

1. INTRODUCTION

Today, with the increase in population, especially in big cities, the number of vehicles in traffic is also increasing. Air pollution caused by the increasing number of vehicles causes serious health problems [1, 2]. At the same time, negativities such as the increase in the number of vehicle accidents with traffic density, high fuel costs, travel stress, environmental problems; pushes countries to seek solutions to reduce traffic density [3]. Some of the solutions found: In order to reduce the use of private vehicles, public transportation usage fees have been reduced, road works have been carried out for better public transportation [4, 5], and in some countries, citizens have been encouraged to use the shared vehicles instead of private vehicles [6, 7]. In addition, there have been some attempts to introduce some new methods to traffic systems in order to find a solution to the increasing traffic density [8-10]. In order to provide efficient transportation with less time loss and reduce fuel consumption, studies have also been carried out on vehicle engine control [11].

Although some specific solutions have been presented due to problems that are caused from traffic density, more permanent and general solutions are still seeking for. Different studies have been performed for managing of intersections. Some of those are as follows: Vehicle delay at intersections have been work with fuzzy logic method to be modeled [12]. A different fuzzy logic study have been done to reduce vehicle delays at the three-legged intersection [13]. There are also studies with the artificial neural networks at the intersections in addition to fuzzy logic ones in which the reduction of vehicle delays at the intersections targeted [14]. While there are

studies on creating a network and sharing the data collected by vehicles with each other to reduce accidents that increase waiting times at intersections and roads [15], there are also studies on preventing motorcycle accidents that will reduce delay times by reducing traffic volume [16]. In the another performed study, intersection possibilities and jams were endeavored to be minimized with average delay and cross-blocking methods [17].

Arrangement of traffic signal times carry great importance for the intersection be dynamically managed. Various studies with different methods for the reduction of vehicle delay and arrangement of signalization times in the intersection management have been performed. Studies for the arrangement of somehow actuated traffic signals somehow actuated have been performed [18]. In addition to this, some other studies presenting cooperative method for traffic signalization and adaptively changing signalization methods have also been brought about [19-22].

With the studies that carried out the aim of this study is to bring about ideal traffic signalization by reducing the intersection density for the best using of the current road capacity.

2. MATERIAL AND METHODS

The intersection studied in this field is an isolated one. And at that study, losses in the vehicles and roads have been ruled out. Vehicles queue on the road are assumed to be completely discharged at a signal cycle time. There are a lot of methods to minimize the vehicle delay at the intersection. Among the most used methods, there are Australia (Akcelik) [23], HCM [24] and Webster methods [25]. In this study, intersection vehicle delay formulas that belong to Australia have been used. With Formula 1, average queue length formula which takes part in the intersection delay formula of Akcelik (Australia) has been given.

$$N_0 = \frac{QT_f}{4} \left(z + \sqrt{\frac{12(x+x_0)}{QT_f}} \right) \quad (1)$$

The abbreviations for Formula 1 are as follows:

N_0 is the average queue length (vehicle/h), Q is the capacity (Vehicle/h), T_f is the flow time (s), QT_f is the max number of vehicles during T_f (vehicle), x is the degree of saturation, q is the flow (vehicle/s) z is equal to x minus one, x_0 is the max degree of saturation at which its queue is approximately zero.

$$x_0 = 0.67 + sg/6000 \quad (2)$$

g is the effective green time (s), s is the saturation flow (vehicle/s),

Total delay at the intersection is showed with Formula 3.

$$D = \frac{qc(1-u)^2}{2(1-y)} + N_0x \quad (3)$$

The abbreviations for Formula 3 are as follows:

D the total intersection delay (s), qc : the number of average vehicles in each signal cycles (vehicle), q the flow (vehicle/s), u is the green time rate, y is the flow rate (q/s).

$$D = \frac{\lambda r^2}{2(1-q)} \quad (4)$$

Formula 4 is a simpler version of Formula 3, which can be used at lossless intersections.

The definitions of abbreviations in Formula 4 are as follows:

D is the total intersection delay (s), λ is the arrival vehicle to the intersection (vehicle/s), r is the red light time on the each road, q is the ratio of arriving vehicles to outgoing vehicles.

$$\frac{\partial D}{\partial (c-u)} = 0 \quad (5)$$

In this study, Formula 1, which is defined as average delay formula at the total delay one of Formula 3, has not been used since it is as worthless as to neglect. The total intersection delay calculation has been calculated with Formula 4. The total conclusion has been equalized by getting the differentiation of Formula 4 with respect to r. So, the minimum intersection delay has been obtained for the total intersection. This formula has been showed with Formula 5. The intersection optimization has been performed with the calculated minimum intersection delays. The algorithm example presented to calculate the optimum signalization time has synchronously been performed with the intersection delay times in Matlab (Matrix Laboratory).

3. INTERSECTION OPTIMIZATION

This study has been performed on the intersection type in Figure 1. Only straight and right turns allowed as two phases at the intersection. Signalization time is accepted equal on the opposing roads at the intersection. Min. vehicle delay calculated at the intersection. An algorithm has been offered for the traffic signalization time optimization on the basis of minimum intersection delays. Intersection delay calculations, the algorithm and its confirmation have been carried out on the Matlab program.

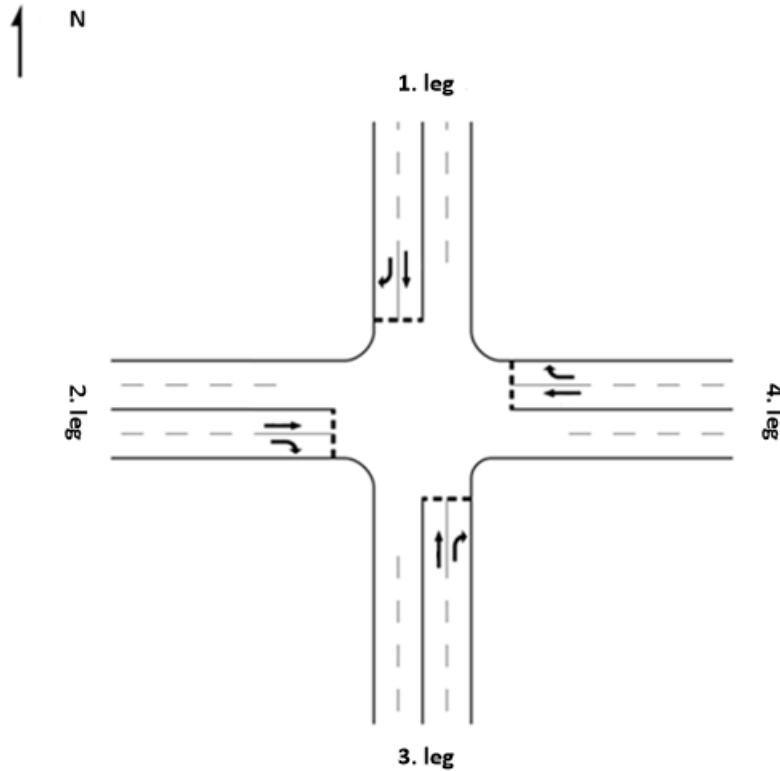


Figure 1. The Studied intersection

In this study, with random vehicle flows, which have been supposed to be obtained from any sensor, have been performed to all legs at the intersection. There are single flow with current value 170 at a single leg, and nine different flows (100,170, 200, 400, 500, 600, 700, 800, 900, 1000), which are randomly selected, at the other three-legged of an isolated and lossless four-legged intersection. The calculations of this example study conducted with the 10 flows, one is 170 current value others are 9 different flows explained / detailed in the previous sentence.

In this example, the most suitable algorithm offered by comparing different algorithms which are traffic signalization classic system independent from environment and actuated method. The intersection saturation flow of this example, leg flow values and the period of the system flow have been given all together in Figure 2.

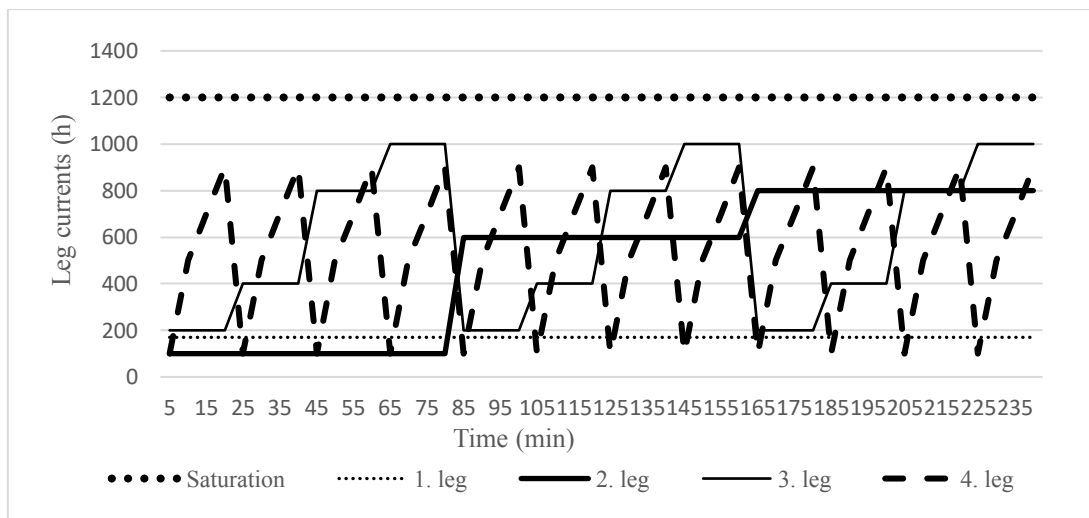


Figure 2. Leg flows on the example

Vehicle flows at the legs have changed in each five minutes. This study consisting of 48 cycles lasted 240 minute in total.

Study comparisons carried out on seven different methods have been showed with Table 1. Traffic signalization cycle times have been decided on 120 s in these studies. Each studies in this table according to 48 different leg flows that be given with Figure 2 have been performed. There is a classical method operating the fixed signalization time in Status 1. Status 2, 3, 4, 5, 6, 7 shows different algorithms of the actuated method.

Status 2 is an algorithm that is instantly defined traffic signalization times with vehicle flows at legs. Although this status is hard to carry out at the intersection, it has been included to compare with the other statuses in the table.

In Status 3, the signalization and the delay time of vehicles has been defined according to previous leg vehicle flows.

At fourth status that is the decimal-cycle algorithm has been calculated traffic signalization times by being considered the leg averages of the past ten cycles. Statuses of sixth and seventh contain algorithm that studies similar to each other. These statuses consist of algorithms that have been proposed in times that require instant intervention like the forth status. This instant intervention: It performs if the instantaneous incoming vehicle flows exceeds 1.5, 2 or 3 times of flow average of the past decimal vehicles. That is, if the instantaneous vehicle flow is at least 1.5, 2 or 3 times of the average determine; the instantaneous vehicle flow instead of the average vehicle flow is used and the traffic signalization time is determined for the delay time calculation. Instant interventions can only study for a single leg at the intersection. If the immediate response studies in all legs. It will lead to confusion in the determination of signalization time.

If it is considered the efficiency obtained the intersection delay times of the statuses compared with Table 1, it is seen that the most efficient algorithm is in the sixth status, which have been suggested within the scope of this study. The classical signalization method has the highest delay time or the lowest efficiency. The methods with the highest efficiency are the last three statuses, which are the methods with immediate intervention. In these last three statuses, the most efficient algorithm is the recommended algorithm and its efficiency exceeds 65%.

Table 1. Intersection delay and efficiency comparisons in the seven different intersection optimizations

Status	Method/Algorithm (loop)	Cycle Time (s)	Cycle Number	D (Total intersection vehicle delay) (s)	Efficiency %
1	Classical	120	48	166132	0
2	Instant interference	120	48	94420	43.16
3	Single-cycle transfer	120	48	119101	28.30
4	Decimal-cycle transfer	120	48	67647	59.28
5	1.5-fold instant transfer	120	48	66435	60.01
6	2-fold instant transfer	120	48	57851	65.17
7	3-fold instant transfer	120	48	65552	60.54

The suggested algorithm flowchart has been given in Figure 3. This algorithm calculates the average of past ten vehicle flows at each legs. If a vehicle flow of twice the average or more comes in, has been used it instead of decimal average in the intersection delay calculation.

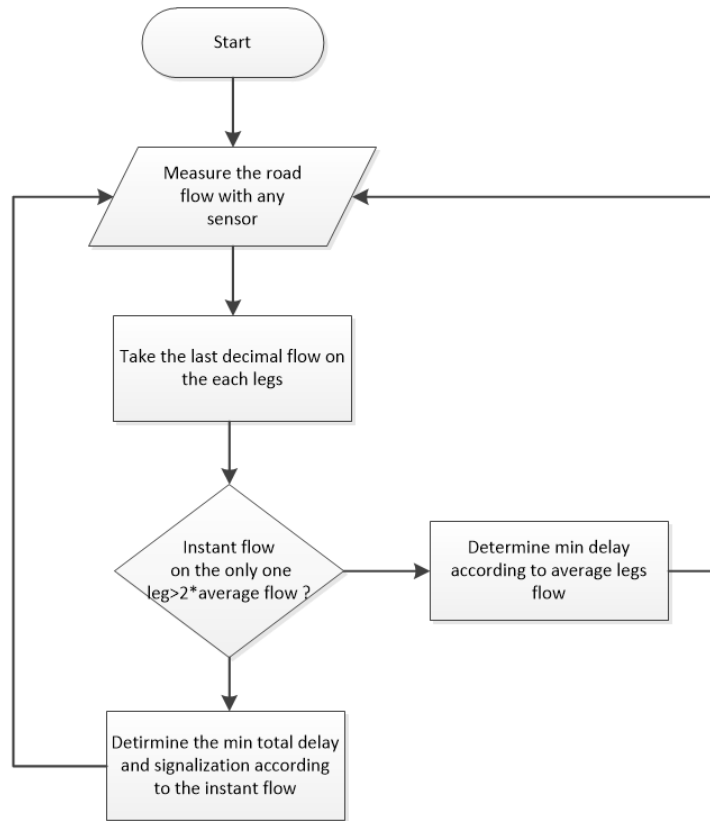


Figure 3. The suggested algorithm flowchart

Total intersection delay that belong to only the actuated method have been given their efficiency in Table 2 without the classical method. All efficiency calculations in this table have been done according to the first status.

Status 4 that is the best efficiency algorithm has 51.42 % efficiency and to minimize the vehicle delays which is clearly seen in Table 2.

Table 1. The actuated method delay time and efficiency comparisons

Status	Method/Algorithm (cycle transfer)	Cycle Time (s)	Cycle Number	D (Total intersection vehicle delay) (s)	Efficiency %
1	Single	120	48	119101	0
2	Decimal average	120	48	67647	43.20
3	1.5-fold instant	120	48	66435	44.21
4	2-fold instant	120	48	57851	51.42
5	3-fold instant	120	48	65552	44.91

With Figure 4 has been given efficiency comparisons of vehicle delays that belong to the actuated method in Table 2.

The superiority of the suggested 2-fold algorithm is clearly seen when it is compared to the other algorithms.

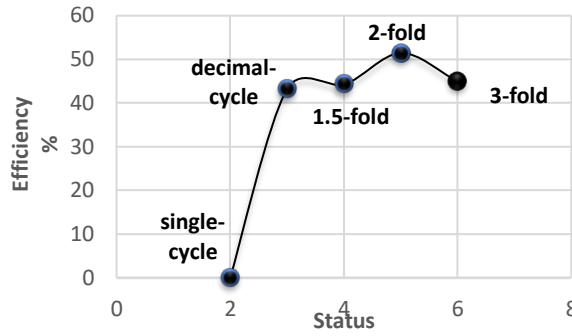


Figure 4. The actuated method delay efficiency comparisons

4. CONCLUSION AND EVALUATION

In this study, with the intersection vehicle delay flow parameters supposed to have been imported from sensors the intersection signalization time optimization have been realized in Matlab. In the study done on an example a new algorithm propounded by being compared different ones submitted.

Comparison between algorithms of actuated signalization that is dependent to the environment and classical signalization method that is independent from environment have been conducted. It has been showed how much the proposed algorithm reduces the vehicle delays at the intersection and how high its efficiency is compared to other methods with the tables and graphs. The proposed 2-fold actuated method according to the classical method has reduced % 65 the intersection delay. The 2-fold actuated method has become more and more successful among others. The 2-fold actuated method has been % 51 more successful than the single method that is define next traffic cycle. In other words, it has reduced vehicle delay at the rate of %51 at the intersection. Other methods, which are the closest to this rate, have become % 44 more successful than single-method.

Table 3. Literature comparisons

Studies	Intersection type	Proposed algorithm	Compared method	Delay efficiency %
<i>This study</i>	<i>Isolated</i>	<i>2-fold Instant (Akcelik)</i>	<i>Classical (fixed-time)</i>	<i>65.17</i>
[21]	Isolated	Signal control scheme	Akcelik	16.24
[26]	Isolated and Multiple	Adaptive Traffic Signal Control Model (Deep Learning)	Webster	35.1
[27]	<i>Isolated</i>	Recurrent Q-learning (Deep Learning)	Classical (fixed-time)	44.35
[28]	<i>Isolated</i>	Optimization Method (Artificial Intelligence)	Webster	27.5
[29]	<i>Isolated</i>	Signal control optimization	Akcelik	36.9
[30]	<i>Isolated</i>	Genetic	Webster	15
[31]	<i>Multiple</i>	Improved	Standard Genetic	34.57

The comparisons of this study and the literature studies on similar subjects are given in Table 3. These studies have been examined in terms of the intersection type, the proposed method, the compared method and the percentages of reducing the intersection delay times of the proposed methods. It is clearly seen that this study is successful and much more efficient in reducing the intersection delay time compared to other studies in Table 3.

The performed study has been carried out on a single intersection. Each study has been compared with different methods in term of reducing the delay time of the vehicles at the intersection delay and transferred to table as percent efficiency. The carried out study has been compared with classic method using the formulate of Akcelik and showed in Table 3 that 65.17 % efficiency has been obtained compared to the classic method in the intersection delay.

On different algorithms for the intersection management might be conducted in the sequel of this study. The different studies may be engineered for the determination of signalization time by the instant intersection vehicle density. In the meantime, this algorithm may be engineered at the lossy intersections.

REFERENCES

- [1] Cai, M., Yin, Y., Xie, M., (2009). Prediction of hourly air pollutant concentrations near urban arterials using artificial neural network approach. *Transportation Research Part D: Transport Environment*, 14, pp. 32-41.
- [2] Sharma, A. R., Kharol, S. K., Badarinath, K., (2010). Influence of vehicular traffic on urban air quality—A case study of Hyderabad, India. *Transportation Research Part D: Transport Environment*, 15, pp. 154-159.
- [3] Akanbi, Olajubu, (2012). A fuzzy-based intelligent traffic control system for managing VIP-induced chaos at road intersections. *African Journal of Computing ICT*, 5, pp. 109-119.
- [4] Nuzzolo, A., Comi, A., (2016). Advanced public transport and intelligent transport systems: new modelling challenges. *Transportmetrica A: Transport Science*, 12, pp. 674-699.
- [5] Ding, J., Zhang, Y., Li, L., (2018). Accessibility measure of bus transit networks. *IET Intelligent Transport Systems*, 12, pp. 682-688.
- [6] Nie, Y. M., (2017). How can the taxi industry survive the tide of ridesourcing? Evidence from Shenzhen, China. *Transportation Research Part C: Emerging Technologies*, 79, pp. 242-256.
- [7] Dong, Y., Wang, S., Li, L., Zhang, Z., (2018). An empirical study on travel patterns of internet based ride-sharing. *Transportation research part C: emerging technologies*, 86, pp. 1-22.
- [8] Wang, F.-Y., (2010). Parallel control and management for intelligent transportation systems: Concepts, architectures, and applications. *IEEE Transactions on Intelligent Transportation Systems*, 11, pp. 630-638.
- [9] Hamilton, A., Waterson, B., Cherrett, T., Robinson, A., Snell, I., (2013). The evolution of urban traffic control: changing policy and technology. *Transportation planning technology*, 36, pp. 24-43.
- [10] Li, L., Wang, F.-Y., (2018). A review of past 100-year and perspective of next 50-year development of ground traffic control. *Autom. Sin.* 44 (4), 101, pp. 577–583.
- [11] Chen, H., Zuo, C., Yuan, Y., (2013), Control strategy research of engine smart start/stop system for a micro car. in *SAE Technical Paper 2013-01-0585*, Detroit Michigan, United States.
- [12] Murat, Y. Ş., (2006). Sinyalize kavşaklardaki taşıt gecikmelerinin bulanık mantık ile modellenmesi. *Teknik Dergi*, 17, pp. 3903-3916.
- [13] Akgüngör, A. P., E., D., (2016). Bulanık mantık ile diğer sinyal denetim sistemlerinin karşılaştırılması: üç kollu sinyalize kavşak örneği. *El-Cezeri Journal of Science and Engineering* . 3, pp. 110-117.
- [14] Mutlu E., E., Y. M., (2008). Bulanık Mantık ve Yapay Sinir Ağı ile Sinyalize Kavşaklardaki Taşıt Gecikmelerinin Modellenmesi. *Elec Lett Sci Eng*, 4, pp. 11-18.
- [15] Zekri, D., Defude, B., Delot, T., (2010). Summarizing sensors data in vehicular ad hoc networks. *RAIRO-Operations Research*, 44, pp. 345-364.
- [16] Ospina-Mateus, H., Quintana Jimenez, L. A., Lopez-Valdes, F. J., Sankar Sana, S., (2021). Prediction of motorcyclist traffic crashes in Cartagena (Colombia): development of a safety performance function. *RAIRO-Operations Research*, 55, pp. 1257 - 1278.
- [17] Arel, I., C. Liu, T. Urbanik and A. Kohls, (2010). Reinforcement learning-based multi-agent system for network traffic signal control. *IET Intelligent Transport Systems.*, 4, pp. 128-135.
- [18] R. P. Roess, E. S. P., and W. R. McShane, (2004). *Traffic Engineering*. Pearson, NJ, USA: Prentice-Hall.

- [19] Robertson, D. I., Bretherton, R. D., (1991). Optimizing networks of traffic signals in real time-the SCOOT method. *IEEE Transactions on vehicular technology*, 40, pp. 11-15.
- [20] Mirchandani, P., Head, L., (2001). A real-time traffic signal control system: architecture, algorithms, and analysis. *Transportation Research Part C: Emerging Technologies.*, 9, pp. 415-432.
- [21] Ren, Y., Wang, Y., Yu, G., Liu, H., Xiao, L., (2016). An adaptive signal control scheme to prevent intersection traffic blockage. *IEEE Transactions on Intelligent Transportation Systems*, 18, pp. 1519-1528.
- [22] Xu, B., Ban, X. J., Bian, Y., Li, W., Wang, J., Li, S. E., Li, K., (2018). Cooperative method of traffic signal optimization and speed control of connected vehicles at isolated intersections. *IEEE Transactions on Intelligent Transportation Systems*, 20, pp. 1390-1403.
- [23] Akcelik, R., (1981). *Traffic signals: capacity and timing analysis*. ARRB Transport Research Ltd., Greythorn Victoria 3104, Australia.
- [24] Wachs, M., Samuels, J. M., Skinner, R. E., (2000). *Highway capacity manual*. TRB Business Office, United States of America.
- [25] Webster, F. V., (1958). *Traffic signal settings*. Road Research Technical Paper, Road Research Laboratory, Her Majesty Stationary Office, London, UK.
- [26] Li, D., Wu, J., Xu, M., Wang, Z., Hu, K., (2020). Adaptive traffic signal control model on intersections based on deep reinforcement learning. *Journal of Advanced Transportation*, 2020, pp. 1-14, DOI: 10.1155/2020/6505893.
- [27] Zeng, J., Hu, J., Zhang, Y., "Adaptive traffic signal control with deep recurrent Q-learning." pp. 1215-1220.
- [28] Chang, Y. L., Zhou, Y. Y., "Research of signalized intersection delay model by using optimization method." pp. 2742-2746.
- [29] Li, Z., Elefteriadou, L., Ranka, S., (2014). Signal control optimization for automated vehicles at isolated signalized intersections. *Transportation Research Part C: Emerging Technologies*, 49, pp. 1-18.
- [30] R. Qian, Z. L., Y. Wenchen, and Z. Meng, (2013). A traffic emission saving signal timing model for urban isolated intersections. *Procedia Socia Behavioral Sciences*, 96, pp. 2404–2413.
- [31] X. Li, Z. Z., L. Liu, Y. Liu, and P. Li, (2017). An optimization model of multi-intersection signal control for trunk road under collaborative information. *J. Control Sci. Eng.*, 2017, pp. 1-11.



Research Article

EVALUATION OF WHOLE BODY VIBRATION IN WEAVING FACTORY

Authors: Murat KODALOĞLU , Feyza AKARSLAN KODALOĞLU 

To cite to this article: Kodaloğlu, M. & Akarslan Kodaloğlu, F. (2023). EVALUATION OF WHOLE BODY VIBRATION IN WEAVING FACTORY . International Journal of Engineering and Innovative Research ,5(2) , p:104-111 . DOI: 10.47933/ijeir.1192799

DOI: 10.47933/ijeir.1192799

To link to this article: <https://dergipark.org.tr/tr/pub/ijeir/archive>



International Journal of Engineering and Innovative Research

<http://dergipark.gov.tr/ijeir>

EVALUATION OF WHOLE BODY VIBRATION IN WEAVING FACTORY

Murat KODALOĞLU^{1*}, Feyza AKARSLAN KODALOĞLU²

¹Isparta University of Applied Sciences, Vocational School of Technical Sciences, Occupational Health and Safety Program, Isparta, Turkey.

²Suleyman Demirel University Engineering Faculty, Textile Engineering, Isparta, Turkey.

*Corresponding Author: muratkodaloglu@isparta.edu.tr
(Received: 21.10.2022; Accepted: 14.12.2022)

<https://doi.org/10.47933/ijeir.1192799>

ABSTRACT: Mankind in the century we left behind technological developments with the development of mechanization although he succeeded in adapting, such constructive like the vibration that the developments threaten their own health. inability to cope with side elements It's true to say. Vibration; people in the short run stress and stress that causes fatigue and loss of attention burdens, and in the long run, serious health causes problems.

In this study, detailed information was obtained about whole body examinations in sampling. For this purpose, first of all, it was evaluated in relation to being examined, and a detailed examination was made in its evaluation by evaluating it to be measured. In order to benefit from the exposure by the weaving process, it is tried to eliminate the deficiency in the literature used without using it.

Keywords: Vibration, Weaving, Whole Body, Exposure

1. INTRODUCTION

The fact that the weaving industry has an important place in employment in our country means that the responsibilities of employees and employers increase in direct proportion to this. As is the case with other sector workers, textile sector workers are also faced with many occupational health and safety threats today. Since relatively large industrial machines are used in the weaving sector, many accidents occur due to these machines, resulting in loss of limbs. And also; occupational diseases occur due to vibration.

Vibration effect both in terms of human health and working comfort as well as in terms of work efficiency, work quality and work safety is important. In determining the vibration magnitude, exposure action and exposure limit values are taken into account is taken. Exposure action value; exceeded in this case, from the worker's exposure to vibration. controlling the risks that may arise from if the required value is the exposure limit value, employees should definitely not feel a vibration above this value represents the value that should not be exposed[1-4].



Figure 1. Weaving machine

Vibration; describes oscillatory motions in a mechanical system. In other words; It is the conversion of potential energy into kinetic energy and kinetic energy into potential energy. Vibration in the working environment adversely affects the working efficiency, health and safety of the person. Two types of vibration are mentioned in the industry. The first is hand-arm vibration, the second is whole-body vibration.

Whole body vibration; It is a form of vibration that, when transferred to the whole body, poses a risk to the health and safety of workers, causing discomfort especially in the lumbar region and trauma to the spine. There are three different components of vibration. These; exposure

surface, frequency of vibration and exposure time to vibration. Depending on these factors, the vibration exposure of the person also varies.

Vibration causes mental and physical fatigue. Due to the negative effects it has on the nervous system, digestive and circulatory systems, it causes decreases in work efficiency. There are also occupational diseases caused by vibration. The most known of the occupational diseases caused by exposure to hand-arm vibration for a long time is 'white finger' disease. White finger disease is mainly caused by mining, forestry, construction, etc. It occurs as a result of vibration in work lines, especially when working with vibrating/power tools. The disease, which causes numbness and loss of function in the hand, can progress to gangrene[5-9].

2. METHOD and DEVICE USED in MEASUREMENT

In vibration measurements, TS EN 1032+A1 standards were used for Testing Moving Machines for the Determination of Vibration Emission Value, one of the standards prepared by the relevant technical committee established by the Engineering Services Preparation Group of the Turkish Standards Institute[5]. In the evaluation, the Regulation of the Ministry of Labor and Social Security on the Protection of Employees from Vibration-Related Risks, which was published in the Official Gazette dated 22.08.2013 and numbered 28743, was taken into consideration[10-13].

2.1. General Principles of Measurement

- During the vibration measurements, care is taken not to create any artificial vibrations that will affect the measurements of the device.
- During the vibration measurement, care is taken not to change the working conditions of the measuring device.
- Risk analyzes, if any, should be used in determining the points or sections to be measured[9-10].

In Figure 2-3-4, the average values of the operator during a shift are shown graphically and the peak values are examined.

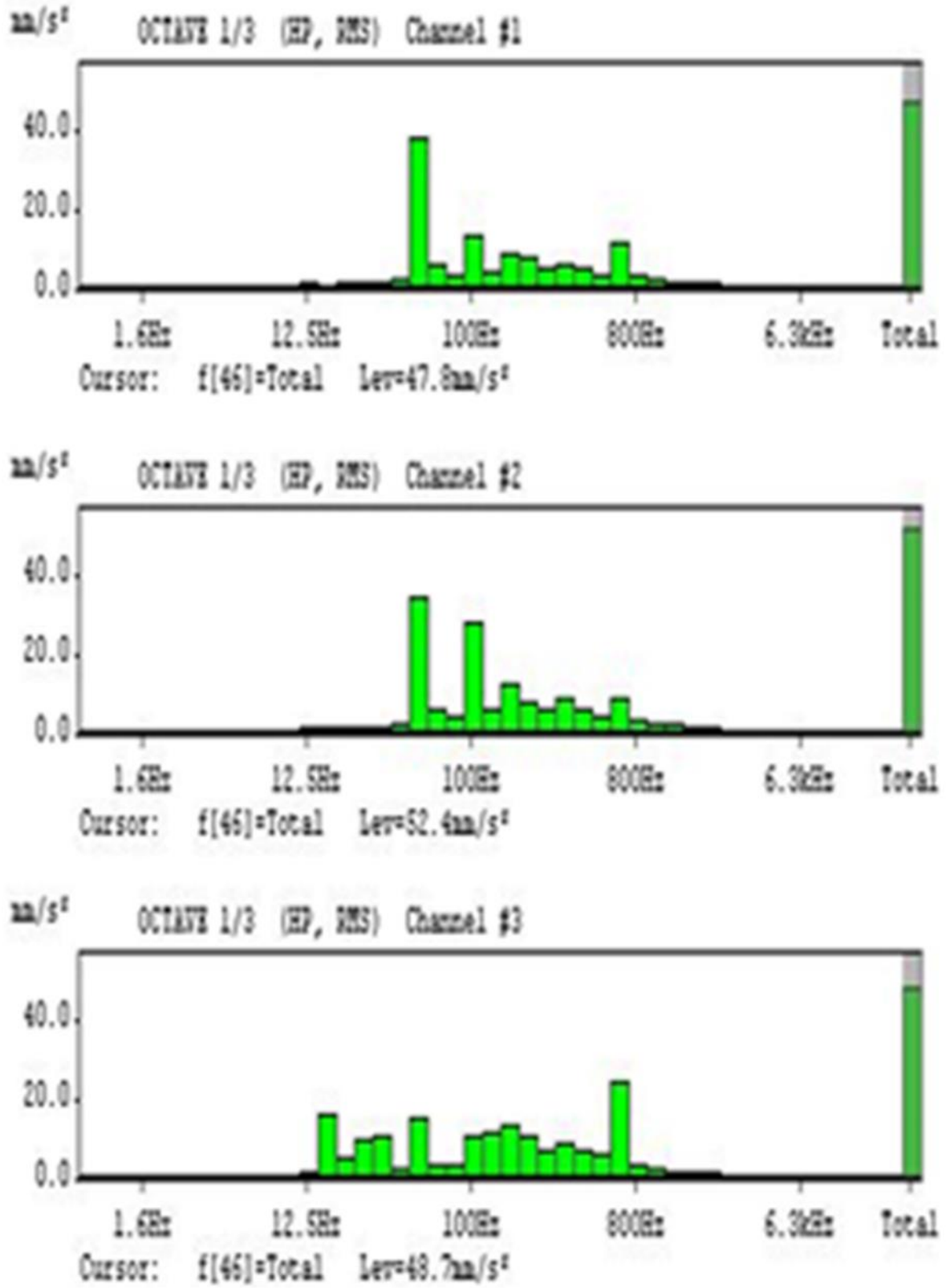


Figure 2. X, Y, Z Axis 1st measurement

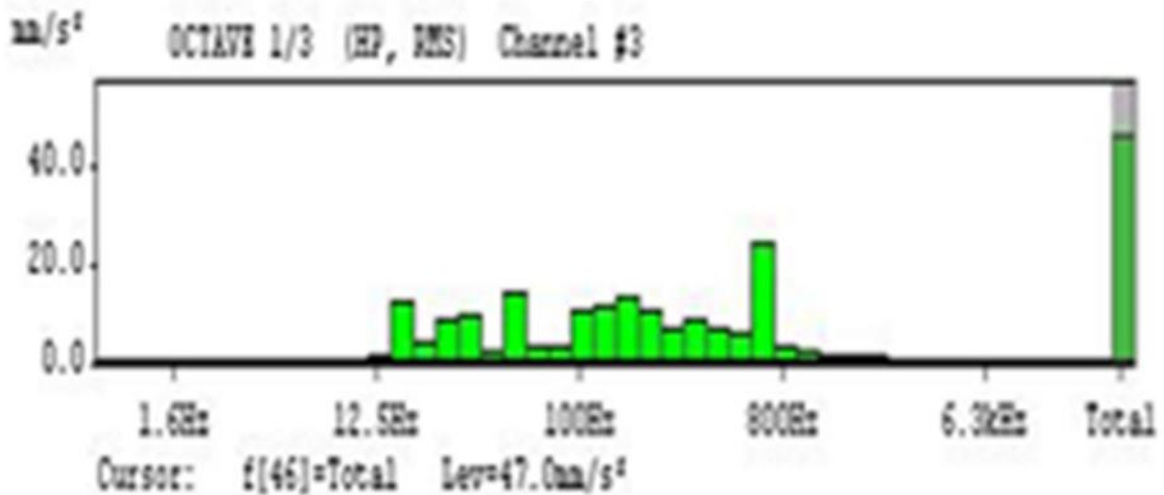
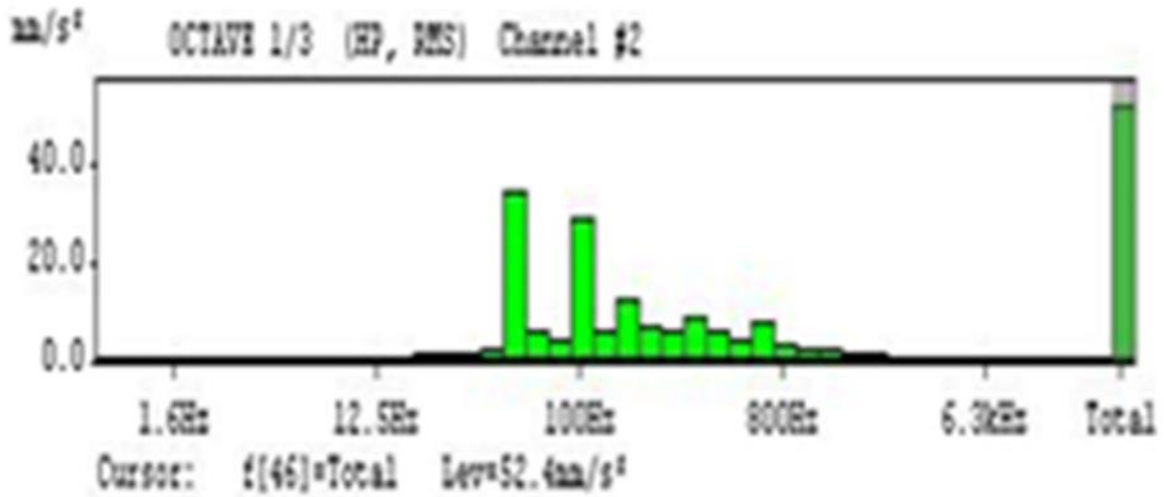
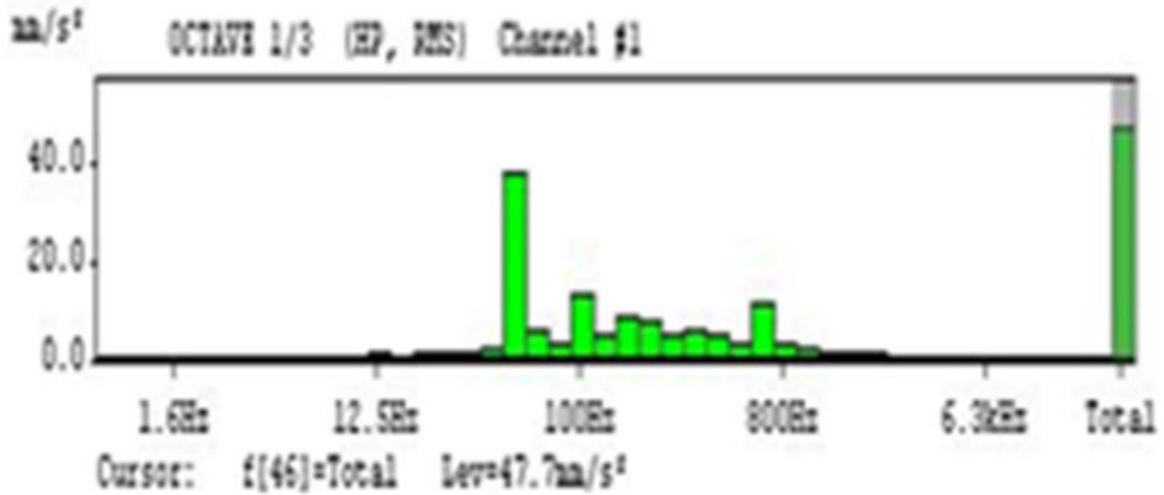


Figure 3. X, Y, Z Axis 2st measurement

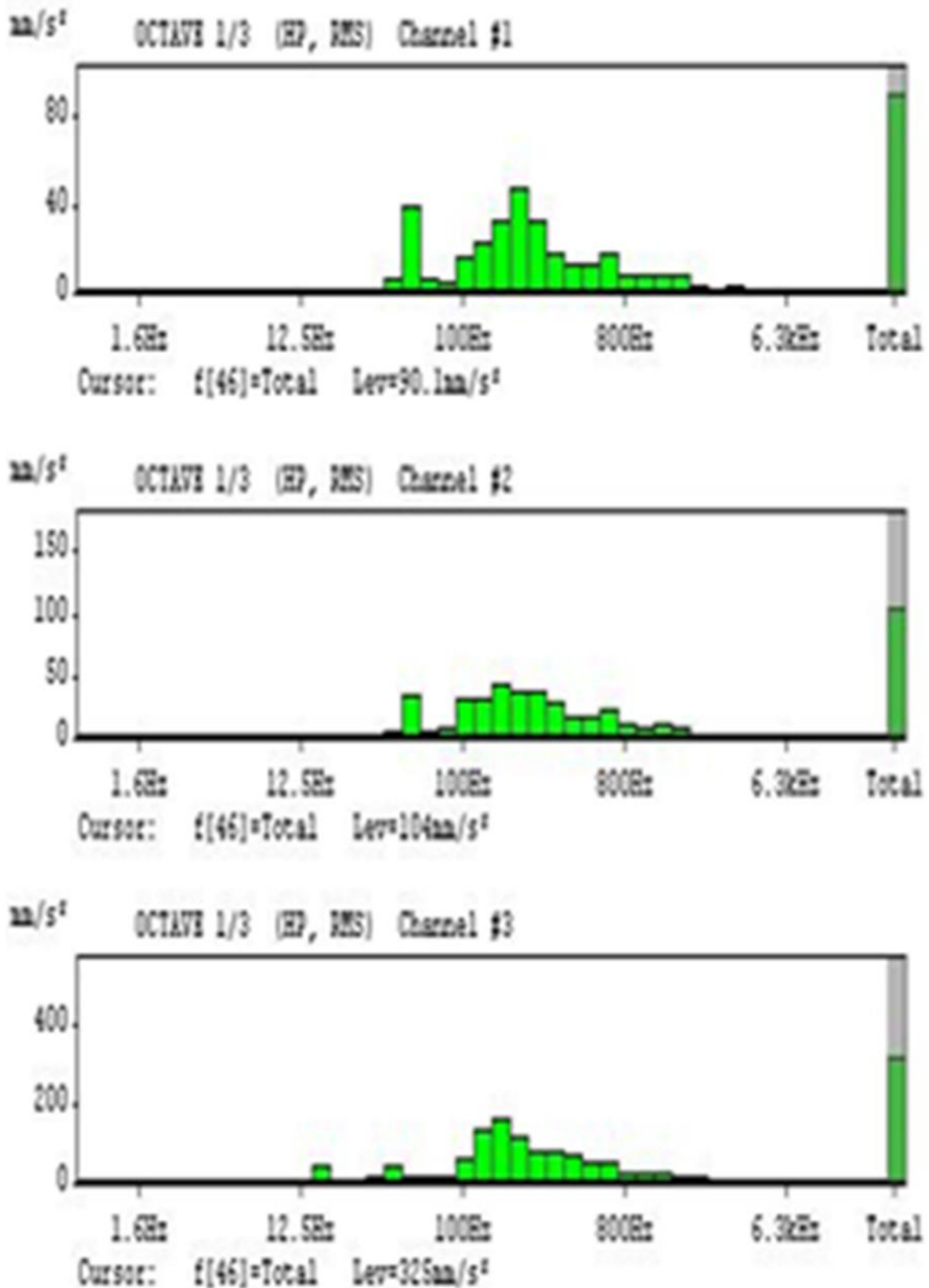


Figure 4. X, Y, Z Axis 3st measurement

After the necessary adjustments made on the device, the intensity of the vibration was measured for all three axes and the raw data were recorded on the device. Then, these data were taken from the device memory in the computer environment and evaluated by calculating time-weighted averages within the working and exposure times of the device with its own package program. The task-based vibration value obtained as a result of the measurements is given in the form of a table.

Table 1. Whole body vibration values (m/s²) and calculated daily exposure [(a(8) (m/s²)] value at workplace

Measuring Instrument	Measuring time (min)	Vibration levels of the axes (m/s ²)	Duration of Work (min)	Personal Exposure (A(8)) [m/s ²]
Weaving machine	3	*X:0,147 *Y:0,167 Z: 0,311	420	0,3105

*Values obtained by multiplying a factor of 1.4

In accordance with the provisions of the regulation on the protection of employees from risks related to vibration, the daily exposure limit value and daily exposure action value are not exceeded.

5. CONCLUSIONS

Vibration is a very important occupational health and safety factor in the weaving sector, as in all other sectors. In this study, personal vibration exposure values of weaving factory workers serving in the weaving branch of the textile industry were examined.

Weaving machines are complex machines consisting of moving parts and can be operated at 600 revolutions per minute depending on the type of work done. Regularly lubricating the moving parts of a machine that operates at such high speeds and three shifts a day, 24 hours a day, will reduce friction and reduce the amount of vibration that will occur.

Weaving machines are large machines. A significant amount of vibration may occur due to their operation at very high rotational speeds. Failure to fix the machines to the floor securely and not placing shock absorbing wedges between the machine and the floor during fixation may lead to an increase in the daily whole body vibration exposure of the employees due to the vibration that will occur.

As the statistical analyzes and graphics show, there are serious correlations between the dimensions of the place where the weaving machines are located and the daily personal vibration exposure of the workers. In this context, the design of the space where the weaving machines will be located should be carefully considered while it is still under construction. Spring systems can be used to prevent vibration at its source. The use of rubber equipment with shock absorbing properties other than spring systems is one of the effective methods for reducing vibration.

Risks that may arise from exposure to mechanical vibration are eliminated or minimized at the source, taking into account the feasibility of combating risks at their source and technical developments.

If it is determined that the exposure action values are exceeded; The employer establishes and implements an action plan that includes technical and organizational measures to minimize exposure to mechanical vibration and the risks it may cause, taking into account in particular the following: Appropriate ergonomically designed work equipment should be selected, taking into account the work done, appropriate ergonomically designed work equipment should be selected, provide seating and auxiliary equipment that effectively reduce whole body vibration to reduce exposure to vibration, appropriate for the workplace, workplace systems and work equipment apply maintenance programs, design the workplace and working environment appropriately, provide employees with the necessary information and training to use work equipment correctly and safely in order to reduce their exposure to mechanical vibration, Limit exposure time and level, arrange working times with adequate rest breaks, exposure limit determines the reasons for exceeding the value, and in order to prevent its recurrence, necessary measures should be taken for protection and prevention.

REFERENCES

- [1]. Armstrong T.J., Marshall M.M., Martin B.J., Foulke J.A., Grieshaber D.C., Malone G., (2002). Exposure to forceful exertions and vibration in a foundry, *International Journal of Industrial Ergonomics* 163–179.
- [2]. Barot R.S., Patel J., Sharma B., Rathod B., Solanki H., Patel Y., (2020). Lean six sigma feasibility and implementation aspect in cast iron foundry, *Materials Today: Proceedings*, Volume 28, Part 2, Pages 1084-1091.
- [3]. Burström L., Neely G., Lunström R., Lilsson T., (2019). Occupational exposure to vibration from hand-held tools: a teaching guide on health effects, risk assessment and prevention, World Health Organization.
- [4]. Carraa S., Monicca L., Vignali G., (2019). Reduction of workers' hand-arm vibration exposure through optimal machine design: AHP methodology applied to a case study. *Safety Science* 120, 706–727, 201
- [5]. ÇSGB, (2013). Çalışanların titreşimle ilgili risklerden korunmalarına dair yönetmelik.
- [6]. Gerhardsson L., Ahlstrand C., Ersson P., Jonsson P., Gustafsson E., (2021). Vibration related symptoms and signs in quarry and foundry workers, *International Archives of Occupational and Environmental Health*, 94(3):1-8.
- [7]. Lindell H., Grétarsson S.L., Macheys M., (2015). High frequency shock vibrations and implications of ISO 5349 – Measurement of vibration, simulating pressure propagation, risk assessment and preventive measures, *Hand-arm vibration: Exposure to isolated and repeated shock vibrations –Review of the International Expert Workshop 2015 in Beijing*, p: 18-30.
- [8]. Mgonja, C.A., (2017). A Review on Effects of Hazards in Foundries to Workers and Environment, *IJISSET International Journal of Innovative Science, Engineering & Technology*, Vol. 4 Issue 6, page 324-336.
- Shen S.C., House R.A., 2017. Hand-arm vibration syndrome, What family physicians should know, *Can Fam Physician*, p:206-210.
- [9]. Vihlborg P., Bryngelsson LI., Lindgren B., Gunnarsson GL., Graff P., (2017). Association between vibration exposure and hand-arm vibration symptoms in a Swedish mechanical industry, *International Journal of Industrial Ergonomics* p:1-5.
- [10]. Xie X.S., Qi C, Du X.Y., Shi W.W., Zhang M., (2016). Measurement and analysis of hand-transmitted vibration of vibration tools in workplace for automobile casting and assembly, *Zhonghua Lao Dong Wei Sheng Zhi Ye Bing Za Zhi*, 34(2):107-10.
- [11]. Kodaloğlu, M., Kodaloğlu, Akarlan F., (2022). Noise Evaluation In Terms Of Occupational Health And Safety On The Ring Spinning Machine. *International Journal of Engineering and Innovative Research*, Cilt 4, Sayı 2, 67 - 75
- [12]. Kodaloğlu M., (2022). Evaluation of Particular Material And Exposure Measurements In Terms of Occupational Health And Safety In A Yarn And Weaving Factory In Denizli Organized Industry Region, *Teknik Bilimler Dergisi*, 12
- [13]. Health and Safety Executive, (2005). The Control of Vibration at Work, Regulations Guidance on Regulations, Hand-Arm Vibration



Research Article

THERMAL BEHAVIOR OF DIFFERENT FLUIDS IN ELECTROMAGNETIC INDUCTION

Authors: Mustafa ÇATAK , Tuncay AYDOĞAN  Ramazan SELVER 

To cite to this article: Çatak, M. , Aydoğın, T. & Selver, R. (2023). THERMAL BEHAVIOR OF FLUIDS IN ELECTROMAGNETIC INDUCTION . International Journal of Engineering and Innovative Research ,5(2),p137-149 . DOI: 10.47933/ijeir.1255096

DOI: 10.47933/ijeir.1255096

To link to this article: <https://dergipark.org.tr/tr/pub/ijeir/archive>



THERMAL BEHAVIOR OF DIFFERENT FLUIDS IN ELECTROMAGNETIC INDUCTION

Mustafa ÇATAK^{1*}, Tuncay AYDOĞAN², Ramazan SELVER³

¹Mehmet Akif Ersoy University, Ağlasun Vocational School, Computer Programming, Burdur, Türkiye.

²Isparta University of Applied Sciences, Faculty of Technology, Computer Engineering, Isparta, Türkiye.

³Süleyman Demirel University, Engineering Faculty, Mechanical Engineering, Isparta, Türkiye.

*Corresponding Author: mustafacatak@mehmetakif.edu.tr

(Received: 22.02.2023; Accepted: 12.05.2023)

<https://doi.org/10.47933/ijeir.1255096>

ABSTRACT: In this study, the thermal behavior of different fluids in electromagnetic induction heating was investigated. For research, induction coil, heat exchanger and control circuit designs were made. An experimental setup was created by using a temperature gauge, tachometer, DC motor and circulation pump. The thermal behavior of 650 ml of boron oil, pure water, olive oil, sunflower oil, motor oil and boron–pure water composition fluids after their circulation at 700 rpm and 92 minutes from the experimental setup was investigated. The heat exchanger surface temperature, circulation channel temperature, beaker temperature and ambient temperature were recorded. The specific heat capacity values of the said fluids were also determined experimentally in another experimental setup. At the end of the research, it was observed that the temperature of 92 minutes showed values between 79 °C and 95 °C in the same electromagnetic induction experimental setup and ambient conditions. It has been determined that the most efficient fluid is the engine oil, which has a heating value of 37 °C at the 2nd minute, 85 °C at the 42nd minute and 95 °C at the 92nd minute. It was observed that boron oil, olive oil, sunflower oil, boron–pure water composition and pure water followed, respectively. It has been observed that the specific heat capacity values are inversely proportional to the temperature increase of the fluids.

Keywords: Electromagnetic Induction, Boron Fluid, Boron–Pure Water Fluid, Olive-Oil Fluid, Sunflower Oil Fluid, Specific Heat Capacity, Heating.

1. INTRODUCTION

Electromagnetic induction systems are a technology that is being developed day by day, especially used for heating purposes. Its application areas are rapidly increasing and becoming widespread thanks to its advantages such as very short processing time, no heat dissipation to the environment, high efficiency as well as not allowing events such as combustion and explosion, being a more reliable system than conventional heating systems [1].

Michael Faraday was the first researcher to describe the basic principles of electromagnetic induction in the 1830s. Other well-known physicists have since contributed to this field of research, such as Emil Lenz, who introduced Lenz's law, and Joseph Henry, who discovered the principal inductance. James Clerk Maxwell summed up the finally discovered electromagnetic phenomenon in four differential equations. These early researchers formed the basis of today's common electromagnetic applications, including the ability to use control devices such as relays, to carry electrical energy without high losses using a transformer, and to transmit energy without the need for any other equipment. State-of-the-art design, also called

electromagnetic induction, is a state-of-the-art method for heating, welding and annealing metallic structures [2].

Although predetermined for metals due to their electrical and magnetic properties, induction heating technology has also begun to be adapted to polymeric materials and composites in the last decade. This fitting provides a summary of the state-of-the-art inductive processing of composites and research is ongoing, covering mechanisms, key parameters, simulations, market-ready experimental applications and the latest developments in this field [2]

The electromagnetic induction heating temperature control method is studied against the background of Internet fusion. Electromagnetic induction heating is widely used because of its environmental friendliness, high efficiency and low heat dissipation characteristics, but the control of the heating process has been slowly developed. PID control and intelligent control together make it well suited to unstable systems. By combining these two, a more adaptable controller can be designed with a small data application, indicating broad application prospects. A mathematical model of electric, magnetic, thermal and force multi-domain two-way real-time coupling calculation is established, and a multi-domain two-way real-time coupling calculation method for electricity, magnetism, heat and force is created. The recommended Temperature accuracy is 96.7% and it has been proven in this study that the temperature control efficiency is increased by 10.1% [3].

In the induction heating system, heating is much more efficient than traditional heating elements, since the heat is only produced in the fluid. In other words, with induction heating, heat losses are reduced and thus the overall heating efficiency is increased.

That's why today's industrial world has to adapt quickly to rapidly changing technology and induction heating system creates many innovations and advantages over other traditional heating methods. For example, induction heating is more energy efficient than other heating methods and is naturally environmentally friendly and does not produce carbon dioxide emissions. It contributes to environmental friendliness by significantly reducing the overall heat exposure of the heat production line. With induction heating, businesses in the industry can maximize environmental, process flexibility and electrical efficiency, as well as offer continuous solutions for the production of higher quality products. These possibilities can be listed as: Safe / Reliable Use, High Efficiency and Energy Saving, Accurate and Easy Temperature Control, Long Service Life, Short Heating Time and High Work Efficiency [4].

Basically an induction heating system; consists of power supply, rectifier circuit, inverter and coil [5]. Electrical energy as a heat source; Indirect Heating is by Direct Heating, Induction Heating, Electric Field Heating, Laser and Ultra-Violet Heating, Conduction Heating, Infrared Radiation Heating, and Electron Beam Heating[6]. The most widely used of these systems is the heating method with resistance [7]. This system is based on the relationship between resistance current and voltage in Joule's Law [8].

In this research, it is aimed to examine the heat generation behaviors by revealing the thermal characteristics of different fluids consisting of boron, pure water, olive oil, sunflower oil, metallic motor oil and boron-water mixture in electromagnetic induction. This research is of great importance in terms of energy use and obtaining the best efficiency with this energy.

2. METHODS

Electromagnetic induction was discovered by Michael Faraday in 1831 and this invention formed the basis of induction heating [9]. Michael Faraday, the founder of modern induction heating, put forward the principle that a voltage can be induced in the secondary circuit with a current change in the primary circuit [10].

The electromagnetic induction system experimental setup designed in figure 1 is seen.

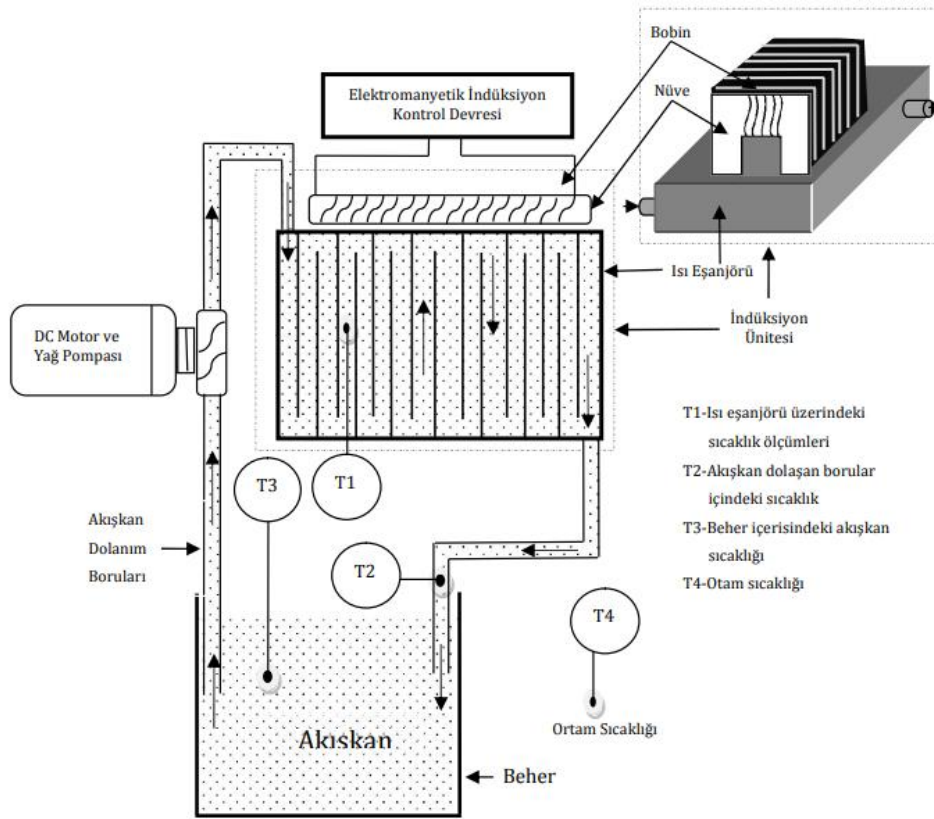


Figure 1. General Structure of Electromagnetic Induction Heating Experiment Equipment.

Figure 1 shows the general structure of the electromagnetic induction heating system designed for this research. The system consists of electromagnetic induction control circuit, induction unit, heat exchanger, DC motor, tachometer, oil pump, temperature measuring unit, thermocouples and fluids.

The induction unit seen in Figure 2 consists of ferrite cores, a coil of 0.25 mm diameter copper wire wrapped around ferrite cores, and a heat exchanger in the form of an iron-based planar plate affected by magnetic induction. Iron-based materials have a higher magnetic induction absorption value than other materials (copper, aluminum, etc.). Therefore, the heat exchanger material was chosen from iron-based material. The magnetic induction absorption of this material also depends on parameters such as the thickness, permeability and volumetric resistance of the material. The calculations of these parameters were calculated with the formula of magnetic flux resistance "Eddy Current" emanations [11].

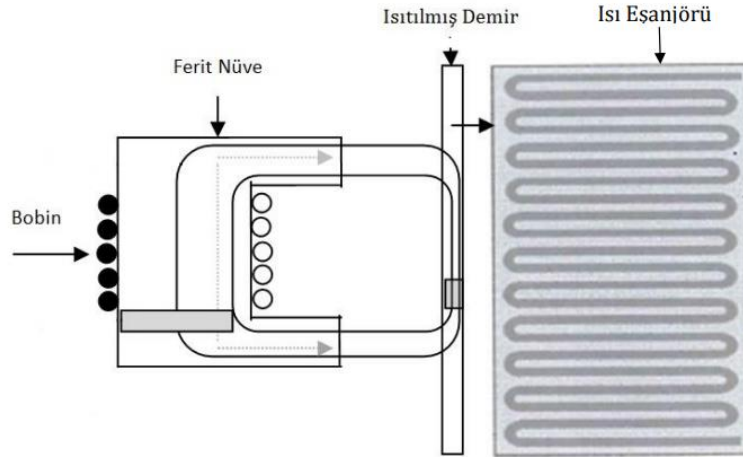


Figure 2. Induction Unit.

In the research, the effect of the specific heat capacities of the fluids whose properties were examined in the electromagnetic induction heating system was also desired to be determined. Specific heat is the energy required to raise the temperature of one gram of a substance by one °C. Each substance has a separate specific heat value [12]. For this, the specific heat is the thermal distinguishing feature of the substance. The unit of specific heat is (J/g °C) [13].

When calculating the specific heat capacities of fluids, the energy changes per unit time are calculated. In the experimental system designed to measure the specific heat capacities of fluids, a new setup was created in which a heating (hot) plate, digital temperature measurement unit, temperature measuring thermocouples and glass beakers were used.

3. EXPERIMENTAL

In this section, the temperature measurement values of the fluids formed by boron oil, pure water, olive oil, sunflower oil, motor oil and boron-water composition and the specific heat capacity measurement values of the fluids are given. The test process for all fluids was considered as follows;

Before electromagnetic induction is given to the system, DC power supply was started and the speed of the fluid was kept constant by adjusting the DC motor speed at 700 rpm. The measurement of the system was controlled with a continuous tachometer in order to keep it at a constant speed. By keeping the speed constant, it is ensured that the fluid circulating in the system is exposed to an equal (constant) amount of electromagnetic induction by keeping the flow rate constant. The temperature values at different points were measured analogously by means of thermocouples placed in the middle of the beaker containing 650 ml of fluid, inside the return pipe coming back from the system and in the middle of the magnetic field surface. Temperatures were obtained in 92 minutes at one-minute intervals. The temperature data obtained were recorded in °C (Celsius).

In the charts below;

- T1: Surface temperature value on the heat exchanger,
- T2: The hot value of the fluid circulating in the system and at the end of the outlet pipe,
- T3: The hot value of the fluid that will enter the system and at the end of the inlet pipe,
- T4: It shows the temperature value of the environment where the test is performed.

3.1. Boron Oil Findings

In our experimental study, boron oil was used first in the electromagnetic induction field according to the above order. The temperature measuring device used in the experiment measures the temperature in Fahrenheit (F) units. The measured values were converted to the C value and used in our research. In the experimental study, in the measurements made before applying electromagnetic induction to the fluid circulating in the system, the heat exchanger surface temperature was recorded as 20 °C, the fluid temperature in the pipe was 20 °C, and the fluid temperature in the beaker was 20 °C. The temperature value of the environment where the experiment was carried out was measured as 16 °C.

Then, electromagnetic induction started to be applied on the experimental system and the temperature of the fluids circulating in the system increased. As a result of the measurements, the temperature value reached 93 °C at the 92nd minute on the heat exchanger from the value of the fluid at 20 °C circulated over the magnetic field. The temperature value did not change in the following times. After this value, the temperature remained constant. The temperature value of the fluid in the pipe has reached from 20 °C to 79 °C and the temperature value of the fluid in the beaker has reached from 20 °C to 78 °C.

3.2. Pure Water Findings

In the experimental study, experiments were carried out by circulating pure water, which is another fluid after boron oil from the electromagnetic induction field, in the experimental system on a different day. Initially, the temperature values, which were equal as at the beginning of the boron fluid, separated from each other during the test period and showed an increase. At the 10th minute, the temperature value obtained from the thermocouple on the heat exchanger surface was measured as 55 °C, the measurement values obtained inside the pipe and inside the beaker were measured as 40 °C. At the 30th minute, the measurement on the heat exchanger surface shows 68 °C, and the measurement results inside the beaker and pipe show 57 °C.

Looking at the measurement results at the 90th minute, the temperature on the surface of the heat exchanger was 79 °C, the temperature inside the pipe was 72 °C and the temperature inside the beaker was 71 °C. As mentioned in this explanation, decreases in temperature values are observed in the parts that come into contact with the atmosphere.

3.3. Olive Oil Findings

As a result of the experiment, the temperature values that were equal at the beginning separated from each other over time and showed an increase in temperature. At the 12th minute, the temperature value obtained from the thermocouple on the magnetic field was measured as 64 °C, the measurement values obtained inside the pipe and inside the beaker were measured as 47 °C. At the 52nd minute, the measurement on the magnetic field shows 85 °C, and the measurement results in the beaker and pipe show 71 °C.

As in the previous experiments, in this experiment, all temperature values were equal at 20 °C, and they showed an increase in temperature by separating from each other over time. At the 12th minute, the temperature value obtained from the thermocouple on the heat exchanger surface was measured as 64 °C, the temperature values obtained inside the pipe and inside the beaker were measured as 47 °C. At the 52nd minute, the temperature on the surface of the heat

exchanger was 85 °C, and the temperature values inside the beaker and pipe were measured as 71 °C.

Looking at the measurement results at the 92nd minute, the temperature on the surface of the heat exchanger was 91 °C, the temperature inside the pipe was 78 °C, and the temperature inside the beaker was 77 °C. It can be seen from here that the temperature values in the parts in contact with the atmosphere differ due to heat loss.

3.4. Sunflower Oil Findings

In our experimental study, sunflower oil belonging to the company "Orkide", which was produced commercially from the electromagnetic induction system, was used as the experimental fluid. The temperature increase that sunflower oil is exposed to in the electromagnetic induction field was measured analogously by means of thermocouples placed in the pipe coming right in the middle of the beaker and in the middle of the heat exchanger surface. The temperature values, which were equal at the beginning, showed an increase by separating from each other over time. At the 12th minute, the temperature value obtained from the thermocouple on the heat exchanger surface was measured as 40 °C, the temperature values obtained inside the pipe and inside the beaker were measured as 23 °C.

At the 62nd minute, the temperature on the heat exchanger surface was measured as 85 °C, and the temperature values in the beaker and pipe were measured as 73 °C. Looking at the measurement results at the 90th minute, the temperature on the surface of the heat exchanger was 89 °C, the temperature inside the pipe was 77 °C and the temperature inside the beaker was 76 °C.

3.5. Engine Oil Findings

In these measurements we made, 10/40 Metallic Engine oil used in engines was added to the beaker. When the flow rate of the fluid circulated in the experimental system setup is fixed, the electromagnetic induction unit is turned on and a magnetic field is given to the system. The temperature values, which were equal at the beginning, showed an increase by separating from each other over time. At the 12th minute, the temperature value obtained from the thermocouple on the heat exchanger surface was measured as 66 °C, the temperature values obtained inside the pipe and inside the beaker were measured as 49 °C. At the 62nd minute, the temperature on the surface of the heat exchanger was 91 °C, and the temperature values inside the beaker and pipe were measured as 77 °C. Looking at the temperature results at the 90th minute, the temperature on the surface of the heat exchanger was 95 °C, the temperature inside the pipe was 77 °C and the temperature inside the beaker was 77 °C.

3.6. Boron-Pure Water Findings

In our experimental study, a compound fluid was obtained by mixing boron oil and pure water at the rate of 50% from the electromagnetic induction field. This compound fluid obtained was used as the final fluid in our experiment system. They are fluids that do not have electrical conductivity of both pure boron oil and pure water; It has been determined that the electrical conductivity of the mixture fluid formed when distilled water, which has no electrical conductivity, is dropped into the boron oil. Pure water and boron oil were placed in a beaker of 325 ml each, and a homogeneous composition fluid with a total volume of 650 ml was obtained.

Thermocouples placed in the middle of the beaker, inside the incoming pipe and in the middle of the heat exchanger surface, analogously, the temperature values that the composition was exposed to in the electromagnetic induction field were measured. While making the measurements, the flow rate of the fluid was determined as 700 rpm and the fluid was circulated through the magnetic field with a constant flow rate.

The temperature value of the fluid in the beaker in the resulting composition fluid is very different from other fluids and the temperature values inside the pipe. While the temperature value inside the beaker was measured as 30 °C at the 32nd minute, it was measured as 68 °C inside the pipe and 73 °C on the heat exchanger surface. It is understood that the composition obtained here also exhibits a different heating characteristic in the atmospheric environment. At the end of the 92nd minute, the temperature value measured on the heat exchanger surface was 88 °C, while it was 81 °C inside the pipe and 63 °C inside the beaker.

3.7. Specific Heat Capacity Values Findings

In the experimental system prepared for the research, the heat changes of the fluids in the electromagnetic induction prepared experimentally were investigated. Boron oil, pure water, olive oil, sunflower oil, metallic motor oil and boron-pure water mixed fluids were used as test fluids in the experiment set prepared under electromagnetic induction in the research, and the values in each fluid were plotted by measuring the temperature values. Table and graphically measured temperature values were compared.

The compared temperature values were found different for each fluid. It has been revealed that the differences in these temperatures are related to the specific heat capacities, which are the physical properties of the fluids. Therefore, the specific heat capacities of each fluid must be known. However, since the specific heat capacities of the fluids we used in the research are not found in the literature, additional research is needed in our research. Due to this requirement, the specific heat capacities of each fluid were experimentally measured by creating an experimental set.

It will be explained that the temperature values of all fluids circulated in the electromagnetic induction experiment set and the differences in time are related to the specific heat capacities, which are the physical properties of the fluids. Each substance has its own specific heat capacity value. For this, the specific heat capacity is a physical property that distinguishes the thermal performance of the material. The specific heat capacity unit is kcal/kg °C.

In the experimental measurements obtained on the experimental set prepared to measure the experimental specific heat capacity values, the compound fluids with known specific heat capacity and unknown specific heat capacity on the same experiment set were placed in the same glass beakers with the same mass weights on a single hot plate. they are heated. These beakers, containing different fluids, were exposed on the Hot plate to increased temperature values over time. The graphs of the specific heat capacity values of the fluid with known and unknown specific heat capacity values were drawn in a graphic program. From this graph, the specific heat capacity values of each fluid were found graphically.

In addition, in the experimental study, the specific heat capacity is calculated analytically as follows, starting from the total amount of heat given to the fluid in a beaker whose specific heat capacity is known.

$$\frac{m_{water} \times C_{p\ water} \times (\Delta T)_{water}}{\text{Heat Value of Fluid with Known Specific Heat Capacity}} = \frac{m_{boron} \times C_{p\ boron} \times (\Delta T)_{boron}}{\text{Heat Value of Fluids with unknown Specific Heat Capacity}} \quad (1)$$

In formula 1, the masses are taken as 75 g for all fluids. The values in Table 1 are the values obtained when the values obtained from the measurements are applied to the 1st formula with water with known specific heat capacity. 75 g of water and 75 g of boron fluid in the beakers placed on the experimental set are placed on the hot plate with the same temperature value at room temperature.

Then, the temperature of the hot plate is gradually increased and the temperature values created by the heat transmitted to the fluids gradually increase the temperature of the fluids in the beaker depending on time.

These temperature values are taken with a datalogger and recorded in a digital environment. When these temperature values reach the desired point in the experiment, the experiment set is stopped.

The specific heat capacity values of all fluids were calculated separately with the help of the above formula (1) by showing the collected data under a graph. In the calculation, the masses (m) are equal and the temperature starting points are the same for each fluid; When the hot plate temperature value was increased gradually, differences were observed in the temperature values in the fluids. These differences are due to the difference in the specific heat capacities of each fluid.

Each different fluid is calculated individually with this method. Calculated specific heat capacity values are given in Table 1.

Table 1. Calculated specific heat capacity values of fluids

Material	Specific Heat [Kcal/kg °C]
Boron	0,53
Water	1
Olive oil	0,860211
Sunflower oil	0,94056
Engine oil	0,5
Boron-Pure water	1,097198

Comparisons of the specific heat capacity values of the fluids we used in our research are shown in Figure 3. The specific heat capacity of the fluids is inversely proportional to the heat values in the heating of the fluids by electromagnetic induction. The temperature value of metallic engine oil with a low specific heat capacity value is obtained at a higher temperature difference value compared to other oils. The lowest temperature difference value belongs to the boron-pure water mixture.

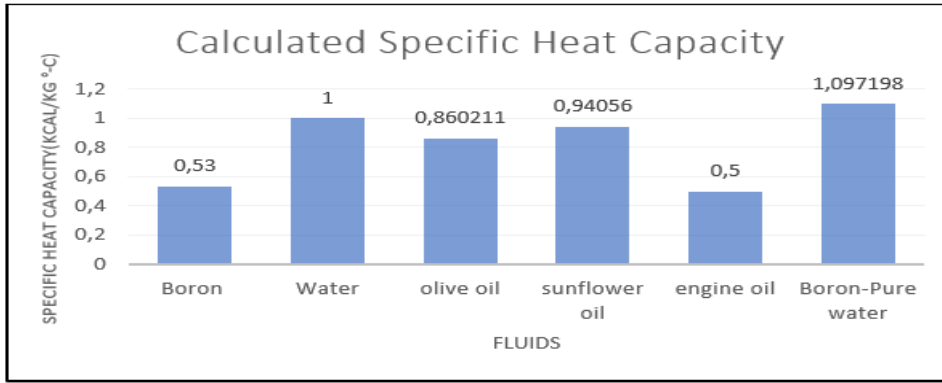


Figure 3. Comparison of specific heats of fluids

For example, in experimental studies with electromagnetic induction, provided that the initial conditions are the same for different fluids; When the above magnetic field temperature values of boron oil and pure water fluids given in Figure 4 are compared, it is seen that the specific heat capacities are inversely proportional.

Considering the numerical values calculated experimentally, the amount of energy required per unit mass is lower in boron fluid, because the amount of heat (heat flux) given to the unit area in our experiment for boron fluid remains the same, so the temperature difference of the boron fluid is high according to the energy balance in the boron fluid.

4. RESULTS

In the curves shown in Figure 4, the heat exchanger surface temperature values obtained by rotating the fluids consisting of boron oil, pure water, olive oil, sunflower oil and motor oils and boron pure water at 700 rpm in the electromagnetic induction system are given comparatively. It is seen in Figure 4 that the heat exchanger surface temperature value in the obtained boron-pure water composition is higher than the heat exchanger surface temperature increase of the pure water forming the composition, and lower than the temperature increase of the boron oil. The boron-pure water composition obtained showed a different feature.

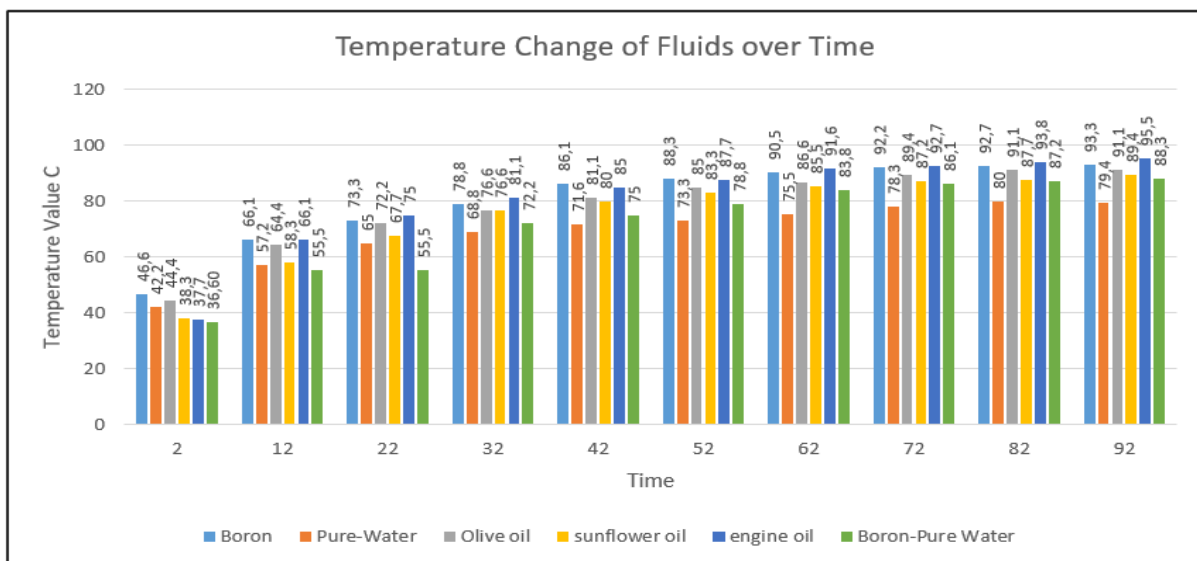


Figure 4. Comparison of the heat exchanger surface temperature values of different fluids.

In Figure 5, the comparison of the inside pipe temperature values returning from the electromagnetic induction system of all fluids including boron oil, pure water, olive oil, sunflower oil, motor oil and boron-pure water composition is shown. Although the boron-pure water composition was lower than the temperature value of other fluids in the 2nd minute time frame, the temperature value reached the temperature values of olive oil and sunflower oil over time and had a value close to them.

If we look at the temperature values of the boron oil and pure water that make up the composition, the temperature value of the boron oil in the 92nd minute was 79 °C, the temperature value of the pure water was 72 °C and the temperature value of the boron-pure water combination obtained was 79 °C.

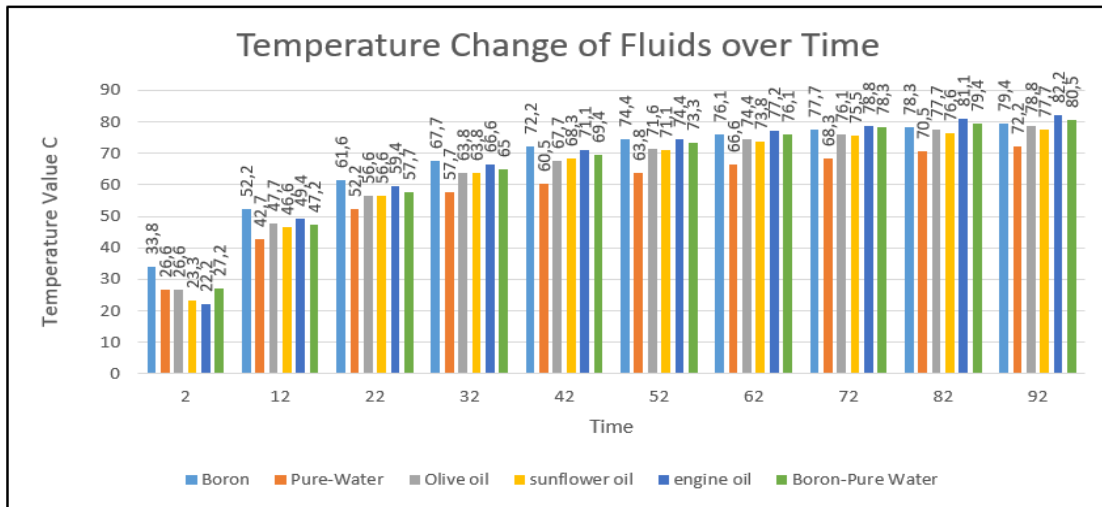


Figure 5. Comparison of in-pipe temperature values of different fluids returning from the electromagnetic induction system

When the above heat exchanger surface temperature values of boron oil, pure water and olive oil fluids given in Figure 6 are compared, it is seen that the physical properties of these fluids are inversely proportional to their specific heat capacities. The specific heat capacity values we found in the experiments are $C_{p \text{ water}} = 1.004 \text{ kcal/kg K}$, $C_{p \text{ boron}} = 0.53 \text{ kcal/kg K}$ and $C_{p \text{ olive oil}} = 0.8607 \text{ kcal/kg K}$. When these values are examined, it is seen that they are ordered according to the amount of energy required per unit mass, according to the specific heat capacity value, which is one of the physical properties of the fluids.

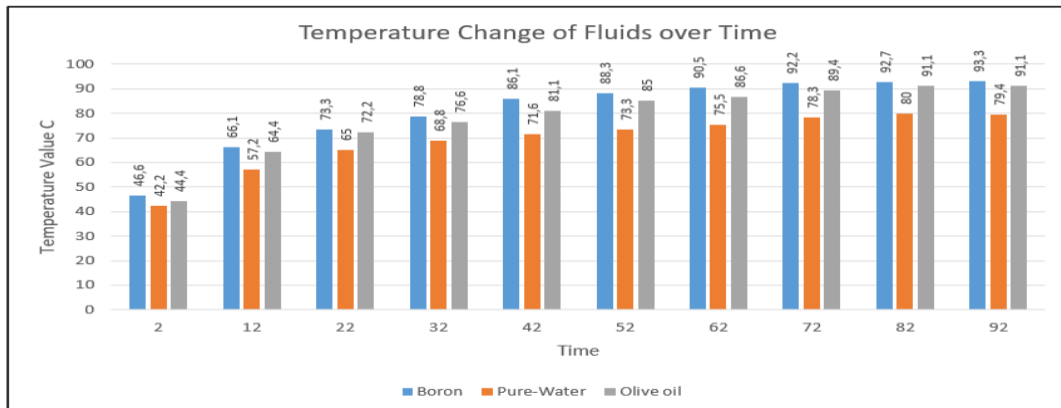


Figure 6. Comparison of the heat exchanger surface temperature values of boron oil, distilled water and olive oil fluids.

When the heat exchanger surface temperature values of boron oil, pure water, olive oil and sunflower oil fluids given in Figure 7 are compared, since the physical properties of water and sunflower oil, which are their specific heat capacities, are higher than other fluids, the temperature values of these fluids are lower than other fluids.

The specific heat capacity values we found in the experiments are $C_{p \text{ water}} = 1.004 \text{ kcal/kg K}$, $C_{p \text{ boron}} = 0.53 \text{ kcal/kg K}$, $C_{p \text{ olive oil}} = 0.8607 \text{ kcal/kg K}$ and $C_{p \text{ sunflower}} = 0.94 \text{ kcal/kg K}$. When these values are examined, the effect of ordering the amount of energy required per unit mass according to the specific heat capacity value is seen.

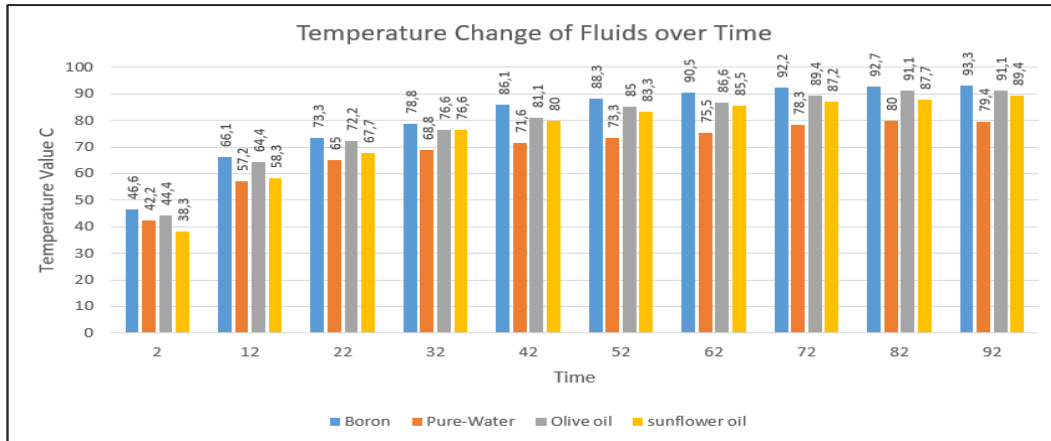


Figure 7. Comparison of the heat exchanger surface temperature values of boron oil, distilled water, olive oil and sunflower oil fluids. (Boron, Pure-Water-Olive Oil-Sunflower Oil)

When the heat exchanger surface temperature values of boron oil, pure water, olive oil, sunflower oil and motor oil fluids given in Figure 8 are examined, it is seen that the specific heat capacities of the fluids are inversely proportional. The specific heat capacity values we found in the experiments are $C_{p \text{ water}} = 1.004 \text{ kcal/kg K}$, $C_{p \text{ boron}} = 0.53 \text{ kcal/kg K}$, $C_{p \text{ olive oil}} = 0.8607 \text{ kcal/kg K}$, $C_{p \text{ sunflower}} = 0.94 \text{ kcal/kg K}$ and $C_{p \text{ engine oil}} = 0.5 \text{ kcal/kg K}$. When Figure 8 is examined, since the specific heat capacity of engine oil is low in the specific heat capacity of other fluids, the temperature increase has occurred due to the energy equality given to this fluid.

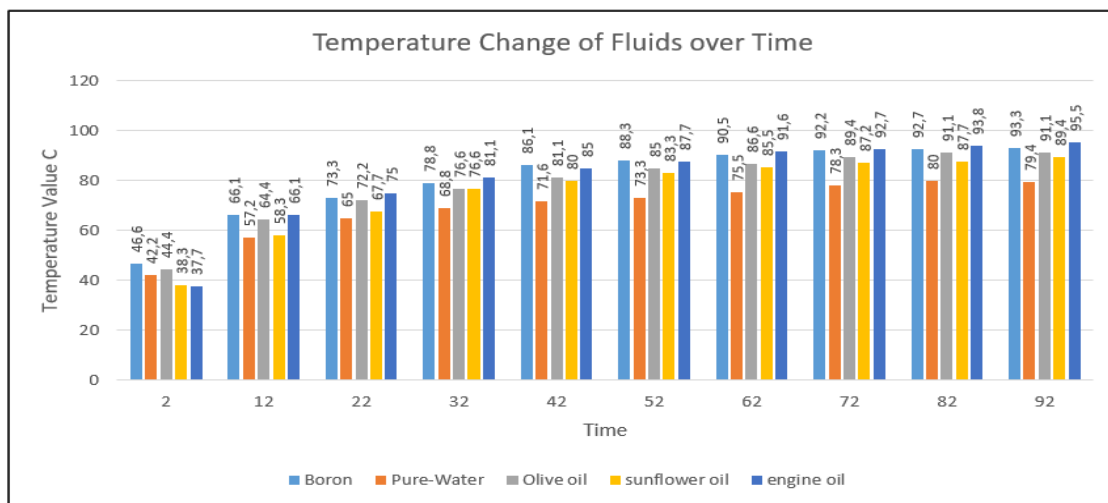


Figure 8. Comparison of the heat exchanger surface temperature values obtained as a result of the measurements of the fluids (Boron, Pure-Water-Olive Oil-Sunflower Oil-Engine Oil)

When the fluids in question are circulated in the electromagnetic induction system at 700 rpm in the heat exchanger system, when their temperature values are measured and examined, it is seen that the fluids are ranked according to the amount of energy required per unit mass, according to the specific heat capacity value, which is one of the physical properties of the fluids.

5. DISCUSSION

In line with the results obtained, a research was conducted to determine the appropriate fluid to be used in order to convert the energy obtained by using electromagnetic induction technology into heat energy. In addition, the relationship between the specific heat capacity values of the fluids and the thermal behavior of the fluids was investigated.

Within the scope of the study, an experimental system was created by using electromagnetic induction circuit, thermocouples, DC motor and circulation pump. The experiments consist of 92 minutes of thermal measurements for each fluid. For fluids passing through the heat exchanger; The heat exchanger surface temperature (T1), the fluid temperature of the pipe end connected to the fluid system leaving the electromagnetic induction system (T2), the beaker temperature (T3) and the ambient temperature (T4) were measured.

In the research, composite fluids consisting of boron oil, pure water, olive oil, sunflower oil, motor oil and boron-pure water mixture were investigated. In the research, the boron oil temperature values were 46.6 °C in the second minute, 86.1 °C in the 42nd minute and 93.3 °C in the 92nd minute, which is the shortest time. The temperature values of pure water are 42.2 °C in the 2nd minute, 71.6 °C in the 42nd minute and 79.4 °C in the 92nd minute. Olive oil temperature values are 44.4 °C at the 2nd minute, 81.1 °C at the 42nd minute and 91.1 °C at the 92nd minute, Sunflower oil temperature values are 38.3 °C at the 2nd minute, 80 °C at the 42nd minute and 89 °C at the 92nd minute. The temperature values of the engine oil composite mixture are 37.7 °C at the 2nd minute, 85 °C at the 42nd minute and 95.5 °C at the 92nd minute. The fluid forming the boron-pure water composition is 36.7 °C at the 2nd minute, 75 °C at the 42nd minute and 88.3 °C at the 92nd minute.

From these data, it has been seen that engine oil and boron oil are the most suitable fluids for heating with electromagnetic induction technology.

In the experimental system we prepared using fluids consisting of boron oil, pure water, olive oil, sunflower oil, motor oil and boron-pure water, the heat flux formed by the electromagnetic field effect; When T1, T2, T3, T4 are compared, it is seen that the differences are related to the specific heat capacities, which are the physical properties of these six fluids.

REFERENCES

- [1] Çetin, S. (2005). *Bir fazlı bir indüksiyon ısıtma sistemi analizi ve dizaynı*. Pamukkale Üniversitesi Fen Bilimleri Enstitüsü.
- [2] Bayerl, T., Duhovic, M., Mitschang, P., & Bhattacharyya, D. (2014). The heating of polymer composites by electromagnetic induction—A review. *Composites Part A: Applied Science and Manufacturing*, 57, 27–40.
- [3] Dou, Q. (2022). Summary of Research on Electromagnetic Induction Heating Temperature Control Method under the Background of Internet Convergence. 2022 4th International Conference on Inventive Research in Computing Applications (ICIRCA), 38–41.

- [4] <https://aismuhendislik.com/induksiyon-isitma-sistemleri>
- [5] Kucukkomurler, A. (2009). Environmental, low cost, energy efficient, electromagnetic indoor induction space heating system design. *IEEE EUROCON 2009*, 1604–1606.
- [6] DALCALI, A., ÖZBAY, H., & Selim, Ö. (2020). İndüksiyon Isıtmada Çalışma Frekansının Isıtma Derinliğine Etkisi. *Mühendislik Bilimleri ve Araştırmaları Dergisi*, 2(1), 43–49.
- [7] YILMAZOĞLU, M. Z. (2010). Isı enerjisi depolama yöntemleri ve binalarda uygulanması. *Politeknik Dergisi*, 13(1), 33–42.
- [8] Aytekin, B. (2008). *Endüksiyon ocak elektronik kontrol sistem tasarımı*. İstanbul Teknik Üniversitesi Fen Bilimleri Enstitüsü.
- [9] Russell, C. A. (2000). *Michael Faraday: physics and faith*. Oxford University Press.
- [10] Ho-Ttecke, D. (2000). How and what can we learn from replicating historical experiments? A case study. *Science & Education*, 9, 343–362.
- [11] Kucukkomurler, A., & Selver, R. (2012). *A Preliminary Experimental Assessment of the Utility of Magnetic Oil for Incrementally Improving the Energy Efficiency of an Induction Heating System*.
- [12] Waples, D. W., & Waples, J. S. (2004). A review and evaluation of specific heat capacities of rocks, minerals, and subsurface fluids. Part 1: Minerals and nonporous rocks. *Natural resources research*, 13(2), 97–122.
- [13] Biçer, A. (2009). *Bazı yağ asidi esterlerinin sentezi, karakterizasyonu ve enerji depolama özelliklerinin belirlenmesi*. Gaziosmanpaşa Üniversitesi Fen Bilimleri Enstitüsü.



Research Article

EXPERIMENTAL ANALYSES OF EMI NOISE SEPARATOR FOR THE CISPR25 STANDART

Authors: Samet Yalçın , Tuna GÖKSU , Selami KESLER , Okan BİNGÖL 

To cite to this article: Yalcin, S. , Göksu, T. , Kesler, S. & Bingöl, O. (2023). Experimental Analyses of EMI Noise Separator for CISPR25 . International Journal of Engineering and Innovative Research ,5(2), p150-160 . DOI: 10.47933/ijeir.1250416

DOI: 10.47933/ijeir.1250416

To link to this article: <https://dergipark.org.tr/tr/pub/ijeir/archive>



International Journal of Engineering and Innovative Research

<http://dergipark.gov.tr/ijeir>

EXPERIMENTAL ANALYSES OF EMI NOISE SEPARATOR FOR THE CISPR25 STANDART

Samet Yalçın¹ , Tuna GÖKSU¹ , Selami KESLER² , Okan BİNGÖL¹ 

¹Department of Electrical and Electronics Engineering, Faculty of Technology, Isparta University of Applied Sciences

²Department of Electrical and Electronics Engineering, Engineering Faculty, Pamukkale University

*Corresponding Author: sametyalcin@isparta.edu.tr

(Received: 13.02.2023; Accepted: 28.03.2023)

<https://doi.org/10.47933/ijeir.1250416>

ABSTRACT: In energy transmission systems, devices must be able to work safely with each other. Therefore, electromagnetic emission and susceptibility of the converting systems are expected to be in a certain range. electromagnetic propagation, especially by radiation and conduction, cannot be neglected in power electronics such as electric vehicle, microgrid, and aerospace technologies. In order to examine and reduce the noise emitted by the devices, the noise should be separated into common mode and difference mode components. In this study, Shou Wang modeling, which is used to separate the noise components into related components, has been examined in order to analyze the noise components within the framework of the CISPR25 standard used for electric vehicles and redesigned. Circuit simulation and design were done and the results were compared. Thanks to these results, it has been seen that the circuit works efficiently up to 90 MHz and gives 8 dB $|S_{11}|$ reflection parameter at the 108MHz threshold level. In addition, the separator circuit was used in a bidirectional DC-DC converter with a known EMI level of 1KW and the noise components obtained were compared with the components of the converter. As a result, it has been seen that the results obtained using the noise separator circuit are almost the same as the real results. In the 18 - 42 MHz range, only the results obtained with the noise separator are up to 8dBuV higher than the real results, other than that the results are exactly the same.

Keywords: Electromagnetic Interference; Interference Analyses; Noise Separation; Common Mode, Differential Mode, Electrical Vehicles, CISPR25.

1. INTRODUCTION

Importance of power electronics, grid technology and solar power systems is increasing with carbon problems and global warming [1, 2]. Due to the increasing importance of electric vehicles and the importance of smart grid technologies, high-power systems have to work together with sensitive communication technologies and complex control mechanisms. For this reason, electromagnetic interferences emitted by high-power systems appear as factors that must be combated. Understanding and optimizing EMC in switch-mode power supplies is an important problem. The switching action of semiconductor devices causes current pulses at the input and output of power supplies. For CCM operation, PWM converters have rectangular current and voltage waveforms with short rise and fall times as well as high rated di/dt and dv/dt . Therefore, these waveforms exhibit a wide and strong harmonic spectrum. For DCM, PWM converters have triangular current and nearly rectangular voltage waveforms. Cross-conduction of current in transistors connected in series generates very narrow and high current spikes[3].

There are two types of electromagnetic interference (EMI) propagation types. The first of these is emission by radiation, which the EMI source interferes with through the air [4-10], and the second is the emission by transmission, where the source interferes over the line to which it is connected [11, 12]. The form of conducted emission noise is defined by modes in systems. These mode components are divided into two as common mode (CM) and difference mode (DM). CM currents are expressed as the sum of the noise currents flowing from the phase and neutral lines to earth. The reasons for this component are the capacitive effects of MOSFET heatsinks and inductive pulses that may occur on both lines due to switching operations. DM is the noise generated by the difference between the phase and neutral voltages. The main reason for this noise is the interaction between the circuit elements or the circuits themselves [13, 14]. Due to high frequency switching elements, CM noise becomes a much more important problem than DM noise [15].

In order to analyze the EMI of the source of conducted emission, the EMI values are measured with the Line Impedance Stabilization Network (LISN) under the test, over the Spectrum analyzer. When measuring conducted and radiated emission, LISN must be used to prevent noise from the main line and affect the reliability of the test, and to fix the measurement ports at 50 Ω. With such a measurement, the relationship between the device under test (DUT) and CM and DM mode noises is shown in the EMI equivalent circuit in Figure 1.

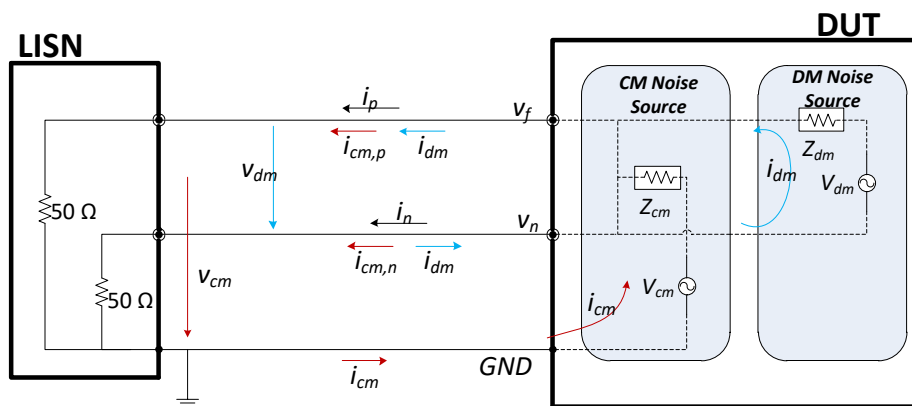


Figure 1: EMI Equivalent Circuit

CM and DM noise modes must be analyzed properly in order to reduce the noise generated in conducted emission at the noise source or propagation path. However, measurements made with LISN do not give any information to the designer about this issue. For that reason, noise modes need to be correctly identified and analyzed for correct suppression [16, 17].

1.1. Differential Mode Noise

DM noise is the noise mode that follows the normal energy path on the lines. The voltage, that is independent of the ground line created by the current flowing from one cable in one direction and from the other cable in the opposite direction, is the difference mode voltage as shown in Figure 2. In other words, the DM noise travels in the same direction as the power in the power line. Thus, interferences in the form of DM flow in the opposite direction on the phase-neutral lines with equal intensity. The main reason for the DM noise is that the circuit components in the device interact with each other and create unwanted voltage differences.

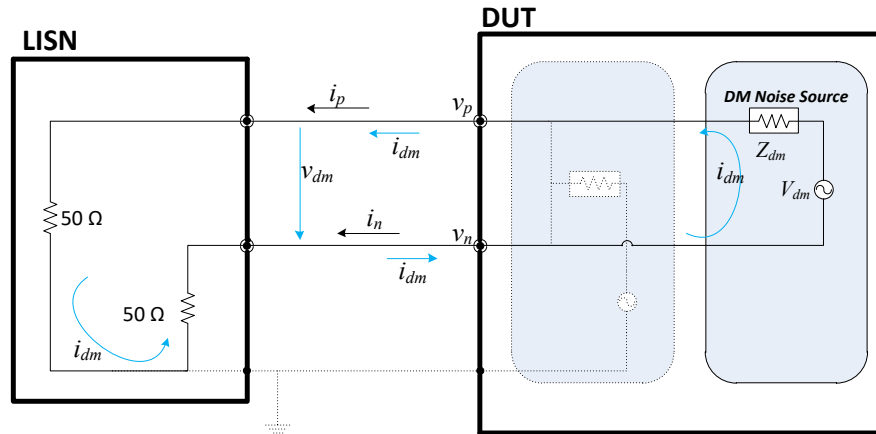


Figure 2: Schematic drawing of EMI DM voltage current

DM current is half of the difference between phase and neutral line currents as given in Eq (1).

$$i_{dm} = \frac{i_p - i_n}{2} \tag{1}$$

The DM voltage is expressed as the difference between the phase and neutral line voltages as given in Eq (2).

$$v_{dm} = v_p - v_n \tag{2}$$

Therefore, the relationship between DM noise voltage and current is defined as follows [11, 18-19]:

$$v_{dm} = v_p - v_n = 50\Omega i_p - 50\Omega i_n = 2 \times 50\Omega \frac{i_p - i_n}{2} = 100\Omega \times i_{dm} \tag{3}$$

1.2. Common Mode Noise

CM noise voltage is a voltage that affects all power lines in the same direction. This voltage occurs between the lines (phase - neutral) and ground as shown in Figure 3. CM noise usually enters the system through a parasitic capacitance and travels to the ground through the system conductors. The main causes of CM noise are inductive tripping pulses that occur in switching operations in power supplies. In addition, undesirable currents at certain frequencies are sent to the ground by the filter capacitors in the power supplies and the heat sinks in the switching device circuit act as capacitors. This may cause CM noises. Another example of common mode currents is noise from EM pulses caused by nuclear effects and lightning [18].

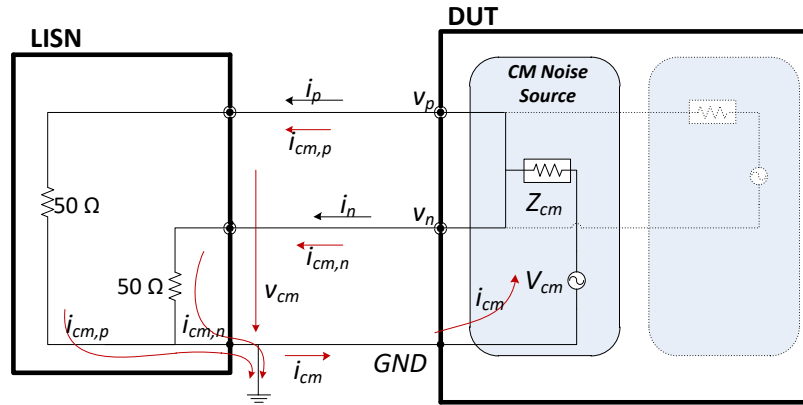


Figure 3: Schematic drawing of EMI CM current

CM currents go from the lines to the ground as shown in Figure 3. It is seen that the CM current is not equal to the phase or neutral line current, but is the sum of the phase and neutral currents as given in Eq (4). The biggest cause of CM currents is parasitic capacitance effects due to circuit structure or ground faults. Because of voltage resulting from this capacitance, CM current flows towards ground. In practice, it is not possible that the impedances of the phase and neutral lines to be equal. For this reason, the common mode current due to the parasitic capacitance cannot be evenly distributed across these lines.

CM currents travel from the lines to the ground as shown in Figure 3. It is understood that the CM current is not equal to the phase or neutral line current, however is the sum of the phase and neutral currents as given in Eq (4). The main cause of CM currents is parasitic capacitance effects due to circuit structure or ground faults. Due to the voltage resulting from this capacitance, CM current flows toward the ground. In practice, it is not possible that the impedances of the phase and neutral lines to be equal. For this reason, the common mode current due to the parasitic capacitance cannot be evenly distributed across these lines.

$$i_{cm} = i_p + i_n \tag{4}$$

In terms of CM noise, the noise presents in the phase and in the neutral line is the same with respect to ground line. Therefore, the CM noise voltage is the arithmetic mean of the phase and neutral voltage as shown in Eq (5). Thus, since one end of the LISN circuit will be terminated with a 50 Ω EMI receiver and the other end with a 50 Ω terminating resistor, the relationship between CM current and voltage will be as shown in Eq (6) [19].

$$v_{cm} = \frac{v_p + v_n}{2} \tag{5}$$

$$v_{cm} = \frac{v_p + v_n}{2} = \frac{50\Omega \times i_p + 50\Omega \times i_n}{2} = \frac{50\Omega}{2} (i_p + i_n) = 25\Omega \times i_{cm} \tag{6}$$

1.3. Electromagnetic Noise Separator

Determining the levels of the CM and DM noise components in switched-mode power supplies is important to reduce EMI. These components can be evaluated via the EMI receiver. In order to analyze the noise components on the receiver, the noise components must be separated.

Five methods are given in the literature for tests to be carried out on noise voltage measurement. These methods are listed as Paul-Hardin circuit, power combiner, Nagel circuit, Caponet circuit, and Shou Wang circuit.

The sum or difference of two input ports from a single output port can be analyzed with the noise separator designed by C. Paul and K. Hardin [20], which is the oldest built using a wideband transformer. However, input impedance of the circuit depends on voltage. This situation creates a great disadvantage for the design.

In another circuit structure designed by Guo [21], the sum or difference of the two input ports is transferred to the output port with the help of phase difference. The results of the design show that the transmission and suppression ratios are very successful. However, in the related article, the (power combiner) equivalent circuit is given as a sum of lines, and the circuit is more complex as it is designed within the subject of microwave engineering.

Another circuit structure was proposed by A. Nagel [22]. This structure is the first transformer-based circuit to deal with the input impedance problem. However, although the CM and DM resistors provide the desired 25 and 100 Ω values as expected, the expected values decrease due to the capacitive noises occurring between the primer and seconder windings of the T1 transformer.

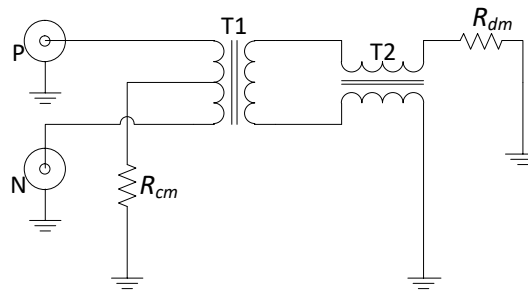


Figure 4: Nagel EMI Separator

Another transformer-based proposal was proposed by C. Caponet and F. Profumo in 2001 and 2002 [23, 24]. However, testing of the proposed circuit is done by measuring the input of the other port, considering that one port input is terminated with a 50 Ω source impedance. This measurement is inaccurate because the source impedance may not be 50 Ω in practice and the terminated port may affect the designed port impedance [25]

Shou Wang developed a proposal with an improved version of Nagel's circuit in 2005 [25]. In the circuit shown in Figure 4, parasitic capacitances between the windings are prevented by not using the second winding in T1.

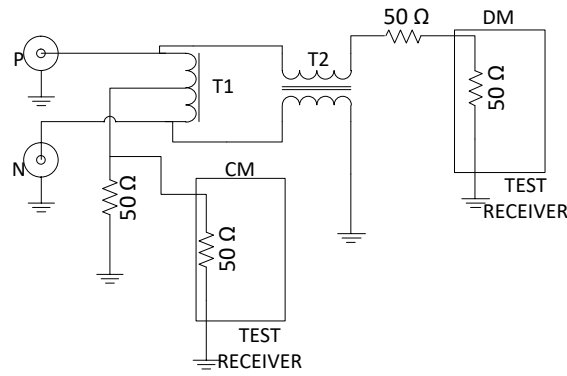


Figure 5: Shou Wang EMI Separator

Kostov's research on methods of separating conducted and radiated emission components [26] reported that Shou Wang's transformer-based noise separator is the method that gives the best results as a passive circuit after the current probe.

EMI receivers have a $50\ \Omega$ terminal load. Therefore, the noise separator circuits must also be terminated with $50\ \Omega$. In this way, one line of the noise separator is terminated with an EMI receiver at $50\ \Omega$, while the other line is terminated with $50\ \Omega$ so that it can be of the same value. The noise separator circuit was originally designed for use in the $150\ \text{kHz} - 30\ \text{MHz}$ range for CISPR 16. However, there is no noise separator trial performed within the bandwidth of the CISPR 25 standard in the literature. In this study, since the analysis bandwidth is in the range of $150\ \text{kHz} - 108\ \text{MHz}$, the capability of microwave transformers to be used in circuit design at this level is analyzed and the actual measurement results are shown. In section II, the noise separator has been decided is explained and design with schematic, PCB and actual design. In section III, the result of the design is presented and compared with the calculated CM noise. Then the deviation between the calculated CM noise with the CM noise received via the noise separator is analyzed mathematical deviation methods. Finally, in section IV, the results of measurements are evaluated and it is decided that this noise separator can be used for analyzing CM noise of any circuit.

2. NOISE SEPARATOR DESIGN

For the design of Shou Wang's circuit, the design is carried out on the KiCad program as given in Figure 6. Paying attention to Figure 6(a), it can be seen that Eq (3) and Eq (6) are correctly applied by making the CM port in parallel with a $50\ \Omega$ resistor and the DM port in series with a $50\ \Omega$ resistor.

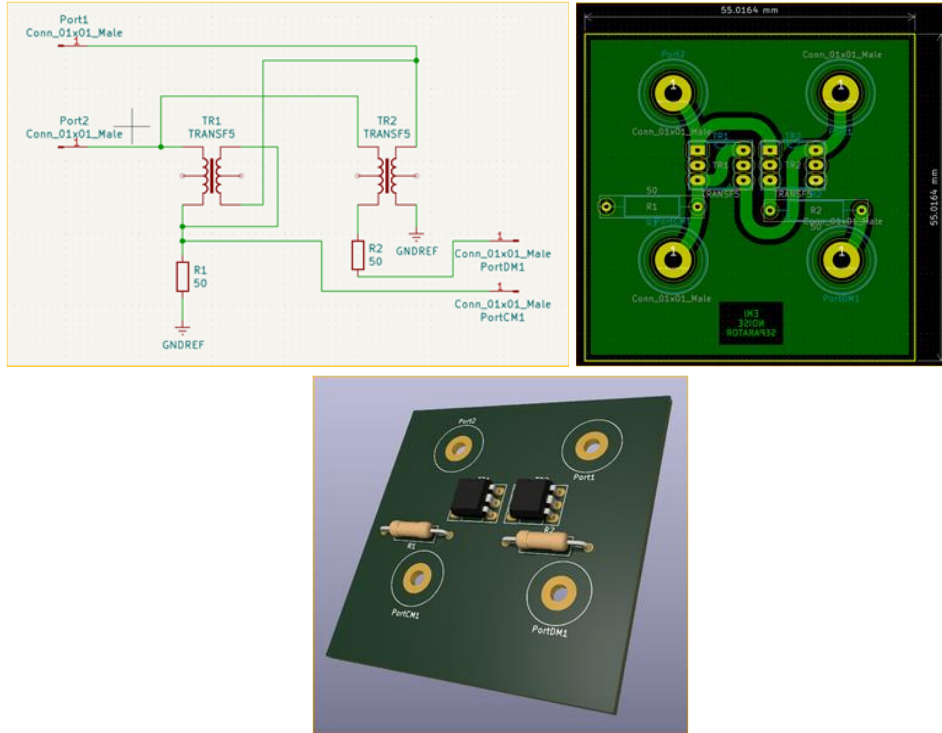


Figure 6: Noise Separator Design

Coilcraft brand wb1010 model broadband RF transformers and N type connectors are used to design the noise separation circuit. The designed circuit is fabricated for experimental analysis as shown in Figure 7.

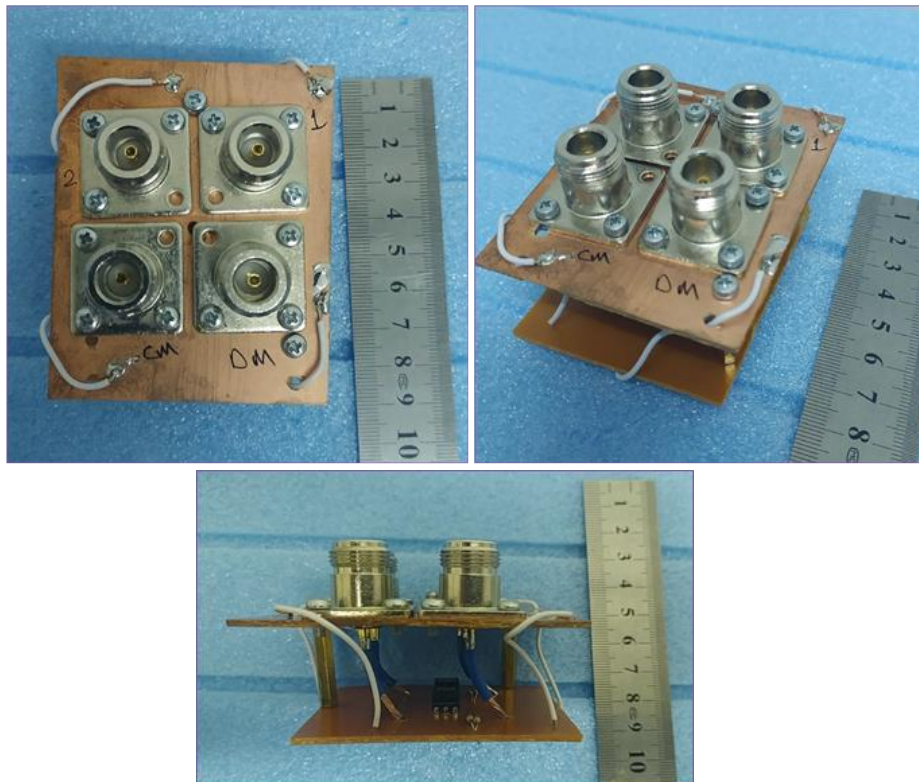


Figure 7: Noise Separator

3. EXPERIMENTAL RESULTS

In order to examine the transmission and reflection ratios of the circuit, the scattering parameter (S-parameter) is examined. Measurements are made by Keysight N9912A Fieldfox Network Analyzer. Figure 8 shows the S-parameter graph. Here, $|S_{11}|$ and $|S_{21}|$ are the reflected wave, and S_{31} and S_{41} are the transmitted wave. The graphics are perfectly compatible with Shou Wang's circuit up to 30 MHz. However, no measurements were found in the literature above 30 MHz. When the circuit is examined with a bandwidth of 150 kHz to 108MHz, it is seen that the transmission and reflection of the circuit approach each other towards the end. When the result in Figure 8, because of the parasitic equivalent parallel capacitor (EPC) of the RF transformer, measurement accuracy is decreasing. But when we examine Figure 10, it is seen that the noise separator can give the actual results.

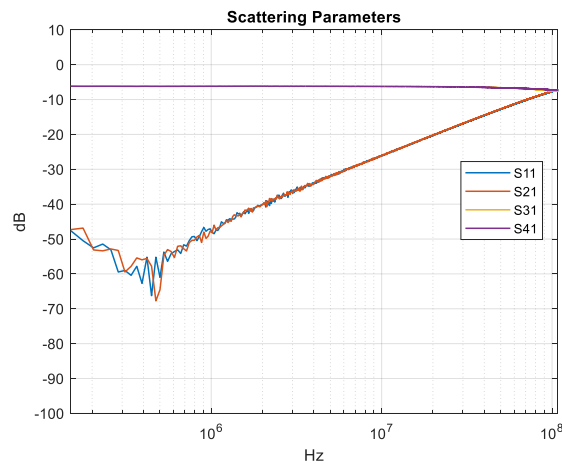


Figure 8: Noise Separator Scattering Parameters

The noise separator circuit, whose scattering parameters were examined, was then used in the real test environment. First, a sample DUT circuit was tested in a laboratory environment established in accordance with CISPR25 standards. This test environment was created as shown in Figure 9. With the help of LISN shown in Figure 9(b), the phase and neutral noise values of the circuit were taken with the Tektronix RSA5126B Spectrum analyzer shown in Figure 9(c), and CM mode and DM mode noise voltages were calculated by applying Eq (2) and Eq(5). Then, the designed noise separator circuit is connected to the LISN port1 and port2 outputs and the CM noise value is taken from the spectrum analyzer.



Figure 9: Conducted Emission Lab Test Bench, LISN and Spectrum Analyzer

The comparison of the calculated CM noise with the CM noise received by the noise separator is shown in figure 10. It is seen that the graphs obtained are almost exactly the same, only the separator measures higher noise in the 18-40 MHz range. But this is not preventing the determination of the EMI values that need to be suppressed.

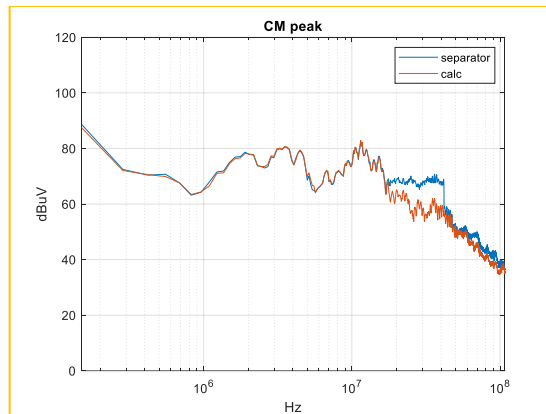


Figure 10: Comparison of CM Noise Separator Result and Calculated CM Noise Result

Deviation in the graphs given in Figure 10 is analyzed mathematically for comparison of the obtained results correctly. Root Mean Square Error (RMSE) and Mean Absolute Deviation (MAD) methods [27, 28] are used to make the comparison.

The RMSE is generally given as

$$RMSE = \sqrt{\frac{1}{n} \sum_{t=1}^n (A_t - B_t)^2} \tag{7}$$

where A_t and B_t are the noise values measured and calculated with the noise separator at each frequency value, respectively. n is the sum of the points received in the frequency base between 150 kHz and 108 MHz.

The MAD method generally calculates the static distribution. The terms used in the equation for the MAD method, whose formula is explained below, are the same as those for the RMSE method.

$$MAD = \frac{1}{n} \sum_{t=1} |A_t - B_t| \quad (7)$$

The deviation rates of the noise graphs, whose graphs are given in Figure 10, are calculated by RMSE and MAD methods. As a result of the calculation, the deviation between the graphs was 9.44% according to the RMSE method and 6.83% according to the MAD method

4. CONCLUSION

For successful suppression of EMI, it is essential to analyze and separate the interference into CM and DM components. In order to examine high-power electronic systems, especially used in electric vehicles, within CISPR 25, the noise components must be known. Separation of interference can be done by some methods. In this study, noise separation methods are discussed and the most suitable method is selected.

A noise separator circuit designed in accordance with the chosen method has been designed in the KICAD program by making certain changes. After performing the circuit, the scattering parameters of the noise separator circuit were analyzed with the help of vector network analyzer and the S_{11} - S_{41} parameters were examined in the range of 150kHz – 108MHz. It has been analyzed that the reflection parameter of the circuit increases as the frequency increases. However, the noise separator is also tested with a 1 kW DC-DC converter which EMI and CM-DM mod values were known. The EMI values are compared with the values obtained with the separator. The deviation between noise values are calculated as 6.83% using MAD method. It is shown that the noise separator circuit works successfully and the separator can be used EMI measurements.

ACKNOWLEDGEMENTS

This study was supported by Isparta University of Applied Sciences Scientific Research Projects Coordination Unit (BAP) with BTAP 2020-BTAP2-0091.

REFERENCES

- [1] M. R. Sancar and A. B. Bayram, "Modeling and Economic Analysis of Greenhouse Top Solar Power Plant with Pvsyst Software," *International Journal of Engineering and Innovative Research*, vol. 5, no. 1, pp. 48 - 59, 2023.
- [2] M. R. Sancar and M. Altinkaynak, "Comparison of Photovoltaic Systems Designed for Different Roof Types for Isparta Province," *European Journal of Science and Technology*, pp. 1024-1028, 2021.
- [3] MARIAN K. KAZIMIERCZUK, "Pulse-Width Modulated DC-DC Power Converters", John Wiley & Sons, Ltd, 2016.
- [4] A. Genc, H. Dogan, I. B. Basyigit and S. Helhel, "Heatsink Preselection Chart to Minimize Radiated Emission in Broadband on the PCB," in *IEEE Transactions on Electromagnetic Compatibility*, vol. 63, no. 2, pp. 419-426, April 2021, doi: 10.1109/TEMC.2020.3019958

- [5] H. Dogan, I. B. Basyigit, A. Genc and S. Helhel, "Parametric Study of the Radiated Emission From the Plate-Fin CPU Heatsink at 2–8 GHz," in *IEEE Transactions on Electromagnetic Compatibility*, vol. 62, no. 6, pp. 2401-2410, Dec. 2020, doi: 10.1109/TEMC.2020.2980773
- [6] I. B. Basyigit, A. Genc, H. Dogan, S. Helhel, "The effect of fin types of the heatsinks on radiated emission on the printed circuit board at S-C band", *Microwave and Optical Technology Letters*, Volume 62, Issue 10 p. 3099-3106, 2020.
- [7] H. Dogan, I. B. Basyigit and A. Genc, "Variation of Radiated Emission from Heatsinks on PCB according to Fin Types," 2019 3rd International Symposium on Multidisciplinary Studies and Innovative Technologies (ISMSIT), Ankara, Turkey, 2019, pp. 1-4, doi: 10.1109/ISMSIT.2019.8932797.
- [8] I. B. Basyigit, A. Genc, H. Dogan, F. A. Şenel, S. Helhel, "Deep learning for both broadband prediction of the radiated emission from heatsinks and heatsink optimization", *Engineering Science and Technology, an International Journal*, Volume 24, Issue 3, 2021, Pages 706-714, <https://doi.org/10.1016/j.jestch.2021.01.006>.
- [9] A. B. Karaman, A. Kocakusak, A. Genç and S. Helhel, "The Effect of Feeding Point on Electromagnetic Emission Due to Heat Sink," 2019 Photonics & Electromagnetics Research Symposium - Spring (PIERS-Spring), Rome, Italy, 2019, pp. 368-371, doi: 10.1109/PIERS-Spring46901.2019.9017476.
- [10] A. Genç, S. Helhel, "The Comparison of EM Characteristics of the Heatsinks with Equal Base Area Depending on the Various Geometries", 10th International Symposium on Intelligent Manufacturing and Service Systems, Sakarya, Turkiye, 2019.
- [11] S. Maniktala, *Switching Power Supplies A - Z*, Oxford: Elsevier, 2012.
- [12] S. Yalçın, T. Göksu, S. Kesler and O. Bingöl, "Determination of conducted emi in sic based dual active bridge converter," *International Journal of Applied Mathematics Electronics and Computers*, pp. 241-244, 2020.
- [13] L. Tihanyi, *EMC in Power Electronics*, Florida: IEEE Press, 2004.
- [14] R. Ozenbaugh, *Emi Filter Design Second Edition*, New York: Markel Dekker, Inc., 2001.
- [15] M. Montrose and E. Nakauchi, *Testing For EMC Compliance Approaches and Techniques*, Canada: A JOHN WILEY & SONS, INC., PUBLICATION, 2004.
- [16] S. Yalçın, Ş. Özen and S. Helhel, "EMI filter design based on the separated electromagnetic interference in switched mode power supplies," *Turkish Journal of Electrical Engineering & Computer Sciences*, p. 3033 – 3043, 2018.
- [17] P. S. Niklaus, M. M. Antivachis, D. Bortis and J. W. Kolar, "Analysis of the Influence of Measurement Circuit Asymmetries on Three-Phase CM/DM Conducted EMI Separation," *IEEE Transactions on Power Electronics*, pp. 4066 - 4080, 2021.
- [18] D. Bockelman ve W. Eisenstadt, «Combined Differential and Common-Mode Scattering Parameters: Theory and Simulation,» *Microwave Theory and Techniques*, *IEEE Transactions on*, Cilt %1 / %20018-9480 , no. 5035123, pp. 1530 - 1539, 1995.
- [19] K. S. Kostov, S. Schroth, F. Krismer, M. Pricinsky, H. -P. Nee and J. W. Kolar, "The Input Impedance of Common-Mode and Differential-Mode Noise Separators," *IEEE Transactions on Industry Applications*, pp. 2352 - 2360, 2015.
- [20] C. Paul and K. Hardin, "Diagnosis and reduction of conducted noise emissions," *Electromagnetic Compatibility*, 1988. Symposium Record., *IEEE 1988 International Symposium*, 1988.
- [21] T. Guo, D. Chen and F. Lee, "Separation of the common-mode- and differential-mode-conducted EMI noise," *Power Electronics*, *IEEE Transactions*, vol. 11 , no. 3, pp. 480 - 488, 1996.
- [22] A. Nagel and R. W. D. Doncker, "Separating Common Mode and Differential Mode Noise in EMI Measurement," *European Power Electronics and Drives Journal*, pp. 27-30, 2000 .
- [23] M. Caponet, F. Profumo, L. Ferraris, A. Bertoz ve D. Marzella, «Common and differential mode noise separation: comparison of two different approaches,» *Power Electronics Specialists Conference*, 2001. PESC. 2001 IEEE 32nd Annual, cilt 3 , pp. 1383 - 1388, 2001.
- [24] M. Caponet ve F. Profumo, «Devices for the separation of the common and differential mode noise design and realization,» *Applied Power Electronics Conference and Exposition*, 2002. APEC 2002. Seventeenth Annual IEEE, cilt 1, no. 8, pp. 100 - 105, 2002.
- [25] S. Wang, F. Lee and W. Odendaal, "Characterization, evaluation, and design of noise Separator for conducted EMI noise diagnosis," *Power Electronics*, *IEEE Transactions*, vol. 20 , no. 4, pp. 974 - 982, 2005.
- [26] K. Kostov, *Design and Characterization of Single-Phase Power Filters*, HELSINKI, 2009.
- [27] A. Mehadi, M. Chowdhury, M. N. M., F. Faisal and M. M. Islam, "A software-based approach in designing a rooftop bifacial PV system for the North Hall of Residence," *Clean Energy*, p. 403–422, 2021.
- [28] M. R. SANCAR and A. K. YAKUT, "Comparative Analysis of SAM and PVsyst Simulations for a Rooftop Photovoltaic System," *International Journal of Engineering and Innovative Research*, pp. 60-76, 2022.



Research Article

BI-DIRECTIONAL CLASSIFICATION OF ROMAN PERIOD COINS BY DEEP LEARNING METHODS

Authors: Kıyas KAYAALP , Fehmi ÖZKANER 

To cite to this article: Kayaalp, K. & Özkaner, F. (2023). BI-DIRECTIONAL CLASSIFICATION OF ROMAN PERIOD COINS BY DEEP LEARNING METHODS . International Journal of Engineering and Innovative Research ,5(2),p161-169 . DOI: 10.47933/ijeir.1269680

DOI: 10.47933/ijeir.1269680

To link to this article: <https://dergipark.org.tr/tr/pub/ijeir/archive>



International Journal of Engineering and Innovative Research

<http://dergipark.gov.tr/ijeir>

BI-DIRECTIONAL CLASSIFICATION OF ROMAN PERIOD COINS BY DEEP LEARNING METHODS

Kıyas KAYAALP^{1*} , Fehmi ÖZKANER¹ 

¹Isparta University of Applied Sciences, Faculty of Technology, Department of Computer Engineering, Isparta, Turkey.

*Corresponding Author: kiyaskayaalp@isparta.edu.tr
(Received: 23.03.2023; Accepted: 27.05.2023)

<https://doi.org/10.47933/ijeir.1269680>

Abstract: In this study, the problem of classification of coins, which have historical importance and can only be distinguished by experts, is discussed with pre-learning deep learning algorithms. In the solution to the problem, the RRC-60 dataset, which consists of the images of the coins used in the Roman Republic period, was used. In this study, pre-learning Xception, MobileNetV3-L, EfficientNetB0, and DenseNet201 models were trained using the images on both sides of the coins in the data set. As a result of the training, the best values, Precision, Recall and F1-Score metrics in the MobileNetV3-L model were 98.2%, 96.8%, and 97.5%, respectively, and the test accuracy was 95.2%.

Keywords: Classification, CNN, Coin, Deep Learning.

1. INTRODUCTION

Money has been used as metal and paper since its first invention until today. Different metals are preferred for metal coins. When the coins are examined, a lot of information can be obtained about the period and the region used. When comparing today's coins with the coins used in the past, the old ones are more valuable because of the metals used. The value of these precious coins varies according to the century and the metal used. The determination of which century the coins belong to is carried out by the evaluation of experts in the field. In states that shaped history such as the Roman and Ottoman Empire, each sultan minted coins with his own figures such as seals, signatures, turra, or pictures when he ascended the throne. Therefore, it is very difficult to examine and classify the coins belonging to these periods.

Deep learning architectures, on the other hand, are used in many different fields, from the classification of images to military fields, from medical applications to education. For example; By examining the leaf image of the apple plant with deep learning methods, many examples can be given, such as detecting the disease in the plant [1], and classifying galaxies in space [2].

Some of the studies in the literature regarding the classification of coins belonging to ancient periods are as follows. Temiz et al. brought to the literature a data set consisting of 11080 coin images, consisting of 138 different classes and printed from 1924 to 2019. The authors, who used the ResNet50 deep learning algorithm in their work, achieved a 97.71% money recognition success rate by using the StyleGAN2 method for data duplication [3]. Aslan et al., in their study

using the RRC-60 dataset consisting of 6000 images, obtained a 97.00% coin classification success rate with semi-supervised learning methods called Graph Transduction Games [4]. Yılmaz et al. used the RRC-60 dataset to classify the reverses of Roman Republic coins. In the study, 91%, 91%, and 83% classification success rates were obtained with the pre-learned ResNet152, VGG16, and Inception deep learning models, respectively [5]. Anwar et al. illustrated a graphical user interface by classifying Roman coins into 60 classes and 600 images. In this study, a 98% classification success rate was obtained by using the reverse side of the coins [6]. Ma and Arandjelović reached an average classification performance of 74.25% with a tone-based random forest classifier in a study using 400 Roman coins used for four different denominations during the reign of the Roman emperor Dominican [7]. Anwar et al. developed a special neural network model called CoinNet for the data set consisting of 228 object classes. In the study, they obtained 81.33% classification success by separating the data for 70% train and 30% testing [8].

As the application of machine learning and computer vision in ancient coin analysis (mostly Ancient Roman coins) is a relatively new but rapidly growing field of research, this study addressed the problem of the Classification of Ancient Roman Republic Coins. For this purpose, a classification study was carried out by using pre-learning EfficientNet, DenseNet201, Xception, and MobileNetV3 deep learning models.

2. MATERIAL AND METHODS

3.1. Image Dataset

In the study, the first data set was determined as RRC-60 [9]. A data set was created from coins drawn with a white background. The data set was filed separately as Obverse and Reverse.

The purpose of Coinage Roman Republic Online (CRRO) is to offer an online version of Michael Crawford's Roman Republic Coin (RRC) publication from 1974, which is still the main typology used to describe different kinds of Roman Republican coins. Significant dating changes have been made since the series' 1974 publication as a result of the discovery of new successions, but no effort has yet been made to update the published typology to take these changes into account or make any other modifications. The descriptions of these coins were altered to comply with the requirements of the collection management system used by the British Museum, but they are still based on the type described in the RRC. Richard Witschonke of the American Numismatic Society (ANS) added new species to this catalog that are not part of the British Museum's holdings [10]. There are 60 classes in the data set where sample images are given in Figure 1.



Figure 1. Sample images from the RRC-60 dataset.

The time span of the coins in the dataset is 145 B.C. - 7 B.C. The coins here are Aces, Quadrans, Semis, Sextans, Triens, and Uncia, with the majority being dinars (denarius). The images of the gods Dioscuri, Hercules, Janus, Menerva, Mercury, Rome, and Saturn were embroidered on the coins, in which silver and bronze metals were used as materials. The starting point for the Roman Republic coins in the British Museum collection is the data set used in the research. These can be found in an online special catalog that was created in 2010 as a supplement to the 1910 catalog of Grueber's two collections. The Open Database License makes the coin type data accessible.

Performance evaluation is presented in the RRC-60 using gradually increasing size training sets and primarily training, validation, and test set sections were created (80%, 10%, and 10%). The data set was obtained from images consisting of 12000 RRC coins. The data set consists of 6000 Observes, 6000 Reverses.

In the experimental study for the classification of deep learning-based Roman coins, a data set consisting of 60 classes, 6000 observe and 6000 reverse images was used. As shown in Table 1, by applying the random selection process, 80% of the data set is divided into training, 10% validation and 10% test data.

Table 1. Training, validation and testing distribution of the dataset

Category	Remarks	Image	Distribution
RRC60-Observe	Train	4800	80%
	Validation	600	10%
	Test	600	10%
RRC60-Reverse	Train	4800	80%
	Validation	600	10%
	Test	600	10%

2.2. Deep Neural Networks

The number of deep learning methods used in many different fields, especially in the defense industry, health, space research and agriculture, and the number of studies used to classify images and detect objects from within the image is increasing day by day. Many deep learning algorithms such as Convolutional Neural Network (CNN), Long-Short Term Memory (LSTM), Autoencoder (AE), and Deep Belief Networks (DBN) are used and new ones are brought to the literature by researchers every day. Especially in the classification of images, CNN-based models give more successful results. For this purpose, EfficientNet, DenseNet201, Xception, and MobileNetV3 models, which are popular in this field, were preferred in the classification study of historical Roman coins and brief information about the models was given.

2.2.1. EfficientNet

To build up models simply but effectively, EfficientNet employs a method known as the compound coefficient. Rather than randomly scaling width, depth, or resolution, compound scaling scales each dimension equally with a given set of fixed scaling coefficients. Using the scaling method and AutoML, seven models of various sizes have been developed, most with cutting-edge accuracy and much higher efficiency than CNN. The EfficientnetB0 model was used in the study.

It is argued that scaling single dimensions helps improve model performance, while balancing the scale in all three dimensions (width, depth, and image resolution) best improves overall model performance, considering the variable resources available [11].

EfficientNet is based on the underlying network developed by neural architecture search using the AutoML MNAS framework. The mesh is fine-tuned to achieve maximum accuracy, but is also penalized if the mesh is too computationally heavy. It also penalizes for slow inference time when the network takes too much time to make predictions. The architecture uses a mobile inverted bottleneck convolution similar to MobileNetV2, but much larger in size due to the increase in FLOPS. This base model is scaled up to achieve the EfficientNets family.

2.2.2. DenseNet-201

Each layer is immediately connected to the others in a feed-forward fashion by the DenseNet architecture. The network's aggregated data for DenseNet includes a very small collection of feature maps and a very thin layer (12 filters per layer). Densenet's benefits include illuminating the gradient issue, promoting attribute reuse, and minimizing the number of parameters required to perform various functions [12].

A 201-layer CNN is called DenseNet-201. It loads a pre-trained mesh that has been learned on more than a million images using the ImageNet database. The network divides images into more than a thousand distinct object groups, including keyboards, mice, pens, and a wide range of animals. The network has therefore amassed vast feature representations for a variety of image types. The network's image entry size is 224×224 . We demonstrate that each layer includes convolution with a filter, ReLU activation, and bulk normalization (BN). The batch normalization step, which helps prevent over-learning during training, is the next step after each block receives an input in the shape of a matrix corresponding to an image pixel. ReLU activation for a value change if it is negative, but not if it is positive or vice versa. A preprocessed matrix value is produced by multiplying a matrix image that has successfully completed the ReLU activation phase by the convolution matrix using a filter [13].

2.2.3. Xception

It is possible to fully deconstruct the mapping of inter-channel correlations and spatial correlations in CNN feature maps. The suggested architecture is known as Xception, which stands for "Extreme Inception," because it is a more robust version of the underlying hypothesis of the original architecture.

The feature extraction basis of the network in the Xception architecture is composed of 36 convolutional layers. With the exception of the first and last modules, all of the 14 modules made up of the 36 convolutional layers have linear residual links surrounding them. In essence, the current Xception architecture is a linear stack of highly separable convolution layers connected together [14].

2.2.4. MobileNetV3

Recently, with the increase in portable devices and devices, transfer learning-based algorithms have developed. One of them is MobileNet based architectures. There are three different versions of the MobileNet architecture. One of them is the MobileNetV1 architecture. The MobileNetV2 architecture has been proposed with some changes such as the bottleneck

structure in the MobileNetV1 architecture. Another recently developed architecture based on MobileNet architectures is MobilnetV3 architecture. There are also two different versions of the MobileNetV3 architecture. The first of these is the MobileNetV3 Small and the other is the MobileNetV3 Large architecture. MobileNetV3 architecture is assisted by search optimization algorithms of NAS and NetAdapt networks. At the same time, it uses the h-swish activation function instead of the ReLU activation function, which is predominantly used in the MobileNetV2 architecture. The Swish function is an activation function like ReLU [15].

2.3. Performance Evaluation

When creating a CNN model, it is important to use the most appropriate loss function and to choose the right parameters for this loss function, and it directly affects the performance and the result of the training. The loss function is also called the cost function or the error function. In the training phase loss functions, a regulation is used to prevent over-learning, in other words, it has an important role in over-fitting the loss functions. The loss process is the stage that compares the test data and the predicted output values and measures the performance of the modeling in the training stage of the neural network. The training aims to minimize the loss between targets and forecast outputs and is updated to minimize the average loss with hyperparameters.

In a typical data classification problem, the evaluation metric is used in two phases, the training phase (learning process) and the testing phase. To put it another way, the evaluation metric is used to identify and choose the best answer that will result in a more precise estimate of the future evaluation of a specific classifier. The evaluation metric, meanwhile, was employed as an evaluator to assess the performance of the classifier created in the testing step when tested with hidden data. In Figure 2, the columns in Figure 2 show the actual class, while the rows represent the predicted class. From this confusion matrix, true positive (TP) or true positive and true negative (TN) or true negative indicates the number of correctly classified positive and negative samples. Meanwhile, false positive (FP) or false positive and false negative (FN) or false negative indicate the number of misclassified negative and positive samples, respectively.

		Actual	
		True Positive	False Positive
Predicted	True Positive	True Positive	False Positive
	False Negative	False Negative	True Negative

Figure 2. Confusion matrix

3. RESULT AND DISCUSSION

3.1. Experimental Procedure

Model training of experimental studies, model performance evaluation, which was trained with Tesla P100 as GPU, was made over Google Colab. Trainings on the classification of coins belonging to the Roman Republic Period were conducted with the pre-learning deep learning models MobileNetV3, EfficientNetB0, Densenet201 and Xception. Images of 224×224×3 dimensions were transferred to the inputs of the deep learning models. During the training phase, the base layers of the models are frozen. The hyperparameters used for model training

are given in Table 2. Logistic Regression was used in the tuning method of hyperparameters [15]. In the training of pre-learning models, 32 values from four different Batch size values, Adam from five different optimizers, Cross Entropy from two different loss functions, 100 from fifteen different Epochs, 0.2 from three different dropouts, and 0.001 as learning rate were used. The class value and activation function of the output layer of the models are also set as Softmax. Average training times of Xception, MobileNetV3-L, EfficientNetB0 and DenseNet201 models were measured as 59, 32, 33 and 71 minutes, respectively. After training the models, train and validation accuracies were obtained. Confusion matrix was used to evaluate the classification performance of test data.

Table 2. Training hyperparameters

Hyperparameter	Setting	Best Value
Batch size	16, 32, 64,128	32
Optimizer	Adam, Adamax, Nadam, Adagard, Adadelta	Adam
Loss function	Focal, Cross Entropy	Cross Entropy
Epochs	10, 20, 30, ...,150	100
Dropout	0.1, 0.2, 0.5	0.2
Learning rate	0.00001 - 0.01	0.001

4.2. Comparison of Performance of Deep Learning Models

Pre-learning Xception, MobileNetV3-L, EfficientNetB0 and DenseNet201 deep learning models were trained with the data set created for the study. Since there are 12000 images in the data set, no data augmentation was required. The accuracy and loss graphs obtained as a result of the training performed with the original data are given in Figure 3.

Lowest validation loss in training models; Values of 0.48 were obtained with EfficientNetB0, 0.34 with MobileNetV3-L, 0.46 with Xception and 0.22 with DenseNet201. The highest validation accuracy achieved in training models; EfficientNetB0 values 0.90, MobileNetV3-L 0.94, Xception 0.91 and DenseNet201 0.92 values.

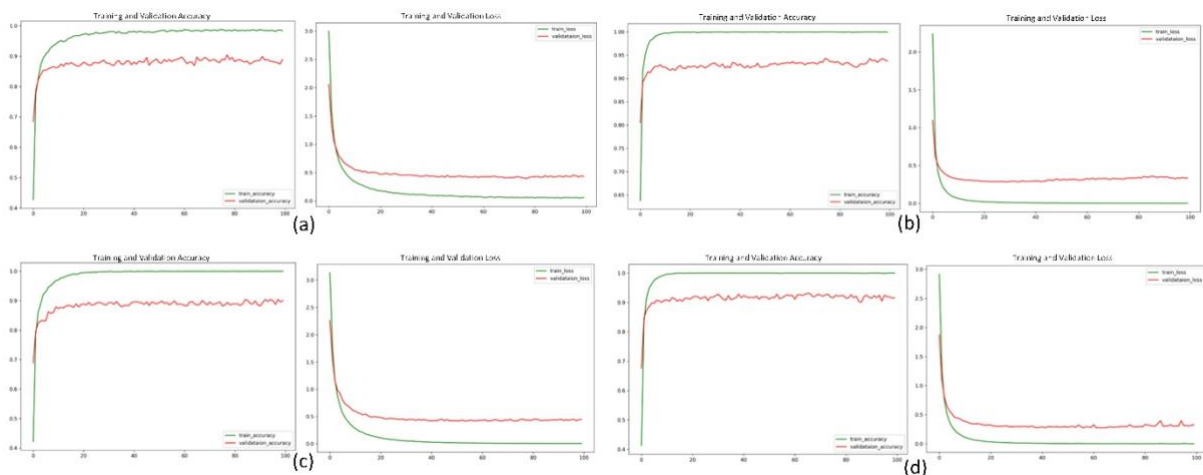


Figure 3. Training and validation loss-accuracy graphs of deep learning models (a)EfficientNetB0, (b)MobileNetV3-L, (c)Xception, (d)DenseNet201

Looking at the Precision values (Table 3) obtained from the test results of the models, it was observed that the highest value was obtained with MobileNetV3-L with 98.2% and the lowest value with the EfficientNetB0 model with 93%. According to the Recall metric, DenseNet201 has the best performance with 97.4%, while the EfficientNetB0 model has the lowest

performance, as in Precision. When F1-Scores are examined, the highest value was obtained with MobileNetV3-L with 97.5%, and the lowest value was obtained with EfficientNetB0 model with a margin of 4.61%. After the training phase of four different pre-trained deep learning models, the highest success rate was achieved with the MobileNetV3-L model with 95.2%, according to the accuracy values obtained by testing the models with images that had not been seen before. In the study, where an average of 91.92% test accuracy was obtained, the weakest performance was obtained with EfficientNetB0, which was 4.45% below the average.

Table 3. Performance evaluation results

Metrics	EfficientNetB0	MobileNetV3	Xception	DenseNet201
Precision	93	98.2	95.8	96
Recall	93.4	96.8	94.8	97.4
F1-Score	93.2	97.5	95.3	96.7
Accuracy	88	95.2	91	93.5

The confusion matrix can be used to perfectly analyze the potential of a classifier algorithm. The first diagonal in the confusion matrix shows the correctly classified results. Therefore, the values of the elements outside the first diagonal of the algorithm with the best classification performance are expected to be zero or close to zero. In the study, the confusion matrix obtained from the MobileNetV3-L model, which gives the best test accuracy as a result of the trainings made with the pre-learning deep learning models, is given in Figure 4.

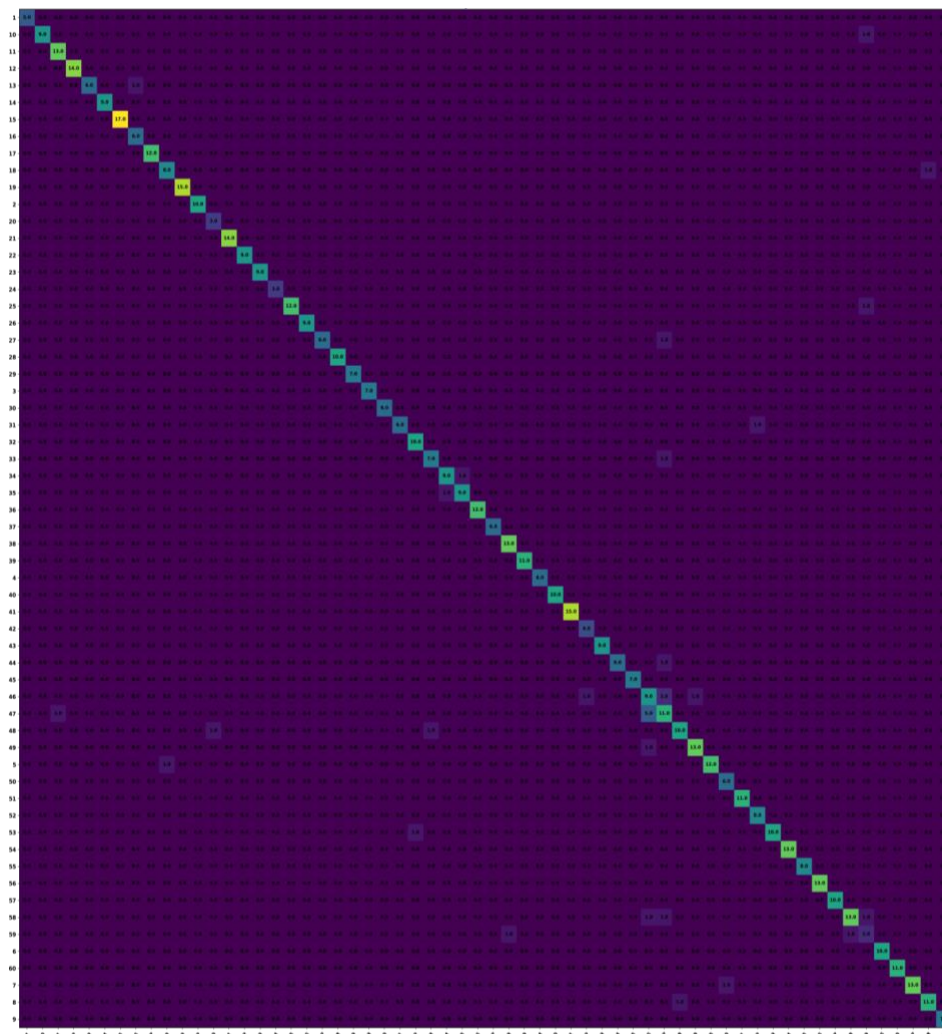


Figure 4. Confusion matrix from the MobileNetV3 model

When the confusion matrix is examined, it is observed that the coins with class numbers 46 and 47 are less successful in classifying than other labels. In the experimental study carried out, P. Sepullius Macer, BC. 44 (46) and P. Sepullius Macer, BC. 44 (47) coins are misclassified because the reverse motifs of the images are very similar (Figure 5).



Figure 5. Coins with class numbers 46 and 47

In Table 4, the previous studies using the data set used in the study and the differences of the proposed study are summarized. In the studies in the literature, classification processes were carried out using only the reverse part of the coins in the data set, and in the study, both sides of the coins were used for classification. A higher success rate than the one obtained in the study was obtained only by Anwar et al. [6] and Aslan et al. [4]. Anwar et al. [6] studied only 600 images and one face, while Aslan et al. [4] used 6000 images, one face and one classification algorithm. In the study, 12000 images, bidirectional and four different classification algorithms were used.

Table 4. A summary of the approaches used in the literature for the classification of Roman period coins

References	Techniques used	Side	Image No	Classes	Accuracy (%)
Aslan et al. [4]	ResNet152	Reverse	6000	60	97.00
Yılmaz et al. [5]	VGG-16, ResNet, Inception	Reverse	6000	60	91, 91, 83
Anwar et al. [6]	Image-based framework	Reverse	600	60	98
Ma and	Hue-based representation and	Reverse	400	4	74.25
Arandjelović [7]	A random forest classifier				
Anwar et al. [8]	CoinNet	Reverse	18000	228	81.33
Ours	EfficientNetB0, Xception, DenseNet201, MobileNetV3	Reverse-Observe	12000	60	88, 91, 93.5, 95.2

5. CONCLUSION

In daily life, people can only recognize coins in circulation. Numismatists and collectors related to the subject, on the other hand, can recognize coins with historical value with years of experience. In this study, coin classification was made using Xception, MobileNetV3-L, EfficientNetB0 and DenseNet201 pre-learning models used in image classification. In the classification process, the RRC60 dataset, which contains the coins used in the Roman Republic period, was used. Approximately 12000 images belonging to 60 classes in the dataset were divided into datasets for training, validation and testing of four different pre-learning models. The MobileNetV3-L model was the model that completed the 100 iterations of the training in the shortest time possible. Looking at the loss rate and Accuracy graphs, Densenet201 and MobileNetV3-L models became ideal in a very short time. In the performance evaluations of the models, only the EfficientNetB0 model was below 90% in the accuracy of the test data. Considering the confusion matrix of the MobileNetV3-L (95.2%) model, which has the most successful classification test accuracy, it is seen that the model's classes 46 (P. Sepullius Macer, BC 44) and 47 (P. Sepullius Macer, BC 44) are classified as their own. mixes between In future studies, it is aimed to develop deep learning-based web and smartphone applications for coin recognition, which will facilitate numismatists and collectors.

REFERENCES

- [1] A. I. Khan, S. M. K. Quadri, S. Banday, and J. L. Shah, "Deep diagnosis: A real-time apple leaf disease detection system based on deep learning," *Comput. Electron. Agric.*, vol. 198, p. 107093, 2022.
- [2] F. Şenel, "A Hyperparameter Optimization for Galaxy Classification," *Comput. Mater. Contin.*, vol. 74, no. 2, 2023.
- [3] H. Temiz, B. Gökberk, and L. Akarun, "TurCoins: Turkish republic coin dataset," in *2021 29th Signal Processing and Communications Applications Conference (SIU)*, 2021, pp. 1–4.
- [4] S. Aslan, S. Vascon, and M. Pelillo, "Two sides of the same coin: Improved ancient coin classification using Graph Transduction Games," *Pattern Recognit. Lett.*, vol. 131, pp. 158–165, 2020.
- [5] A. G. YILMAZ, Ç. SAYGILI, and V. NABIYEV, "Roma Dönemi Madeni Paralarının Derin Öğrenme Tabanlı Sınıflandırılması."
- [6] H. Anwar, S. Sabetghadam, and P. Bell, "An Image-Based Class Retrieval System for Roman Republican Coins," *Entropy*, vol. 22, no. 8, p. 799, 2020.
- [7] Y. Ma and O. Arandjelović, "Classification of ancient roman coins by denomination using colour, a forgotten feature in automatic ancient coin analysis," *Sci*, vol. 2, no. 2, p. 37, 2020.
- [8] H. Anwar, S. Anwar, S. Zambanini, and F. Porikli, "Deep ancient Roman Republican coin classification via feature fusion and attention," *Pattern Recognit.*, vol. 114, p. 107871, 2021.
- [9] G. Ciaburro and B. Venkateswaran, *Neural Networks with R: Smart models using CNN, RNN, deep learning, and artificial intelligence principles*. Packt Publishing Ltd, 2017.
- [10] M. Crawford, "Coinage of the Roman Republic Online," 2021. <http://numismatics.org/crro/>.
- [11] M. Tan and Q. Le, "Efficientnet: Rethinking model scaling for convolutional neural networks," in *International conference on machine learning*, 2019, pp. 6105–6114.
- [12] G. Huang, Z. Liu, L. Van Der Maaten, and K. Q. Weinberger, "Densely connected convolutional networks," in *Proceedings of the IEEE conference on computer vision and pattern recognition*, 2017, pp. 4700–4708.
- [13] A. Jaiswal, N. Gianchandani, D. Singh, V. Kumar, and M. Kaur, "Classification of the COVID-19 infected patients using DenseNet201 based deep transfer learning," *J. Biomol. Struct. Dyn.*, vol. 39, no. 15, pp. 5682–5689, 2021.
- [14] F. Chollet, "Xception: Deep learning with depthwise separable convolutions," in *Proceedings of the IEEE conference on computer vision and pattern recognition*, 2017, pp. 1251–1258.
- [15] A. Howard *et al.*, "Searching for mobilenetv3," in *Proceedings of the IEEE/CVF international conference on computer vision*, 2019, pp. 1314–1324.



Research Article

EXAMINING THE IMPORTANCE OF ARTIFICIAL INTELLIGENCE IN THE SINGULARIZATION OF BIG DATA WITH THE DEVELOPMENT OF CLOUD COMPUTING

Authors: Serkan KESKİN , Ali Hakan IŞIK 

To cite to this article: Keskin, S. & Isik, A. H. (2023). EXAMINING THE IMPORTANCE OF ARTIFICIAL INTELLIGENCE IN THE SINGULARIZATION OF BIG DATA WITH THE DEVELOPMENT OF CLOUD COMPUTING . International Journal of Engineering and Innovative Research ,5(2),p170-180 . DOI: 10.47933/ijeir.1261330

DOI: 10.47933/ijeir.1261330

To link to this article: <https://dergipark.org.tr/tr/pub/ijeir/archive>



International Journal of Engineering and Innovative Research

<http://dergipark.gov.tr/ijeir>

EXAMINING THE IMPORTANCE OF ARTIFICIAL INTELLIGENCE IN THE SINGULARIZATION OF BIG DATA WITH THE DEVELOPMENT OF CLOUD COMPUTING

Serkan KESKİN¹, Ali Hakan IŞIK²

¹Burdur Mehmet Akif Ersoy University, Institute of Science and Technology, Department of Computer Engineering, Burdur, Turkey.

²Burdur Mehmet Akif Ersoy University, Faculty of Architecture-Engineering, Department of Computer Engineering, Burdur, Turkey

*Corresponding Author: serkankeskin@isparta.edu.tr
(Received: 07.03.2023; Accepted: 22.05.2023)

<https://doi.org/10.47933/ijeir.1261330>

ABSTRACT: Big data is a huge amount of structured or unstructured data that cannot be processed, managed and analyzed by traditional data methods. This data often comes from multiple sources and of different types. With the emergence of big data, it has become difficult to process data with the algorithms used to process data. Therefore, new algorithms and technologies have been developed. One of the most important of these technologies is data deduplication. Data deduplication is a process in which data from different data sources are grouped according to their similarities in order to reduce repetitive data and prevent inconsistencies. In this way, it aims to save storage space by storing only one copy of many repeated data. The most commonly used deduplication architectures are inline deduplication, post-process deduplication and hybrid deduplication. Using these architectures, 90% data savings can be achieved in deduplication. Thus, data occupies less space in storage units. Today, artificial intelligence technologies are advancing very rapidly and their application areas are expanding. Therefore, artificial intelligence will continue to be a very important technology for the industry and our lives in the future. The aim of this study is to give an idea about the relationship between deduplication technology and artificial intelligence by examining various deduplication systems and algorithms. In addition, in the light of detailed information about deduplication, the importance of the contributions of today's deduplication systems to information systems is also explained.

Keywords: Cloud computing, artificial intelligence, big data, deduplication.

1. INTRODUCTION

Today, with the introduction of big data, technologies have started to evolve and transform. On the way from desktop computers to a mobile life, our devices have shrunk. In the opposite direction of this shrinkage, there has been a serious growth in our data. Although we use the term "big data", what is actually happening is 'unstructured' data. The vast majority of the source of unstructured data is the internet. This big data has caused the storage areas to fill up over time and new storage areas are needed. This situation has also led to storage costs. The increase in storage space and costs has led to the development of new technologies. Technologies such as Thin Provisioning, Automated Tiering, Snapshot, Virtual Storage Management, Archiving, Deduplication, Compression help to close the gaps of storage systems that have difficulty in

catching up with the growth rate of data. Thanks to these technologies, our data does not take up as much space as before. Deduplication, one of the most important of these technologies, aims to save storage space by storing a single copy of repeated data on a file or block basis.

Deduplication is also known as single instance storage, intelligent compression, data reduction or common factorization. Deduplication is a technology that storage device manufacturers rely on to use storage space more efficiently. Another storage technology is data compression. This feature is often lumped into a larger category called data reduction. All these systems help achieve the same goal - data efficiency for increased storage space. With proper deduplication techniques, businesses can efficiently store more data than their overall storage capacity can offer. Deduplication will always have a huge positive impact on overall storage utilization and reduce costs. But it is important to know which type of deduplication method is required to maximize efficiency in the right way.

Artificial intelligence systems, especially those using machine learning algorithms, require large amounts of high quality data for training and prediction. By using deduplication, the AI system is able to process a dataset that is refreshed and free of redundant data. This aims to provide a cleaner and more accurate dataset for training. The relationship between deduplication and AI is that deduplication is often used as a pre-processing of data before it is fed into an AI system to improve the quality of the data and make working with it more manageable. At the same time, AI models can use deduplication within their tasks to make the process more efficient.

2. RELATED WORKS

In this section, we discuss deduplication technology and studies that examine big data issues. Studies in the literature examining deduplication algorithms, data security, deduplication in the cloud system and artificial intelligence are analyzed. As a result of the analysis, it shows that data deduplication provides significant savings in storage space, the importance of data security, artificial intelligence and deduplication are used as a whole. The prominent studies in the literature review are presented.

In the study by Keles and Nevcihan, the issue of deduplication of rapidly and uncontrollably increasing data in a hotel database was addressed. Various text similarity algorithms were used for text similarity. Distance regularization based similarity, token based similarity, sequence based similarity algorithms and fuzzy string matching algorithms were examined. At the end of the study, a hybrid model using fuzzy string matching algorithm and Jaro Winkler distance is proposed. In the comparison on the test dataset, the model achieved 94% accuracy on the easy dataset and 83% accuracy on the difficult dataset [1].

Pg et al. present an approach to solve the problem of wasted storage space due to the large amount of data. It develops a new method that uses Convergent and Modified Elliptic Curve Cryptography algorithms on a cloud environment to create secure deduplication systems. The performance analysis confirms that the proposed system has 96% security. This result is higher than other existing methods. The evaluation result reveals that the proposed system is highly secure and effective for deduplication for an integrated cloud environment [2].

The study by Jiang et al. investigated data privacy and property management issues for deduplication. In this work, a scheme that resists the poison attack and the recursive forgery attack of cross-user file-level deduplication is used. For this, a new proof of ownership scheme

using the Bloom filter is designed. As a result, the security analysis conserved bandwidth for deduplication. The proof of ownership verification process was used to achieve mutual proof of ownership verification. It has been shown that the proposed schemes can guarantee security requirements other than side channel attack [3].

In the study by Yang et al. existing deduplication schemes were used to resist brute force attacks. It is understood that schemes are designed to ensure efficiency and data availability. However, it is explained that it is not valid for both conditions. In this study, a three-tier cross-domain architecture is investigated. A cloud-efficient and privacy-preserving big data deduplication is envisioned. Decision tree algorithms are utilized. Improved privacy protection, data availability, and accountability capability are shown to outperform the current state of the art while resisting brute force attacks [4].

Barik et al. describe that with the rapid expansion of the Internet of Things (IoT), IoT devices are generating enormous amounts of big data. It is explained that traditional cloud computing systems are not efficient enough to process large volumes of data simultaneously. In order to build a big data deduplication scheme, this paper designs a new GeoBD 2 scheme that defines a geographic deduplication structure. According to the experimental results, it is found that the proposed scheme has minimum overhead cost compared to the existing big data deduplication scheme [5].

Vijayalakshmi and Jayalakshmi, in a research paper, discuss the deduplication techniques used to deduplicate big data generated by connecting many devices to the internet. The main purpose of this paper is to give a good idea about deduplication techniques by examining sufficient information and available data [6].

In the study by Manogar and Abirami, it was seen that the increase in data such as text, images, audio, video, data centers and backup data in recent years has caused many problems in both storage and retrieval process. For this reason, location-based deduplication, time-based deduplication, and chunk-based deduplication techniques are examined and it is explained that it is aimed to determine the best result. Among these techniques, variable dimensional deduplication within the scope of stack-based deduplication technique was found to give better results compared to other deduplication techniques. As a result, it was found that variable dimensional deduplication technique increases storage efficiency and increases the performance of storage resources by allowing more data to be transferred and processed [7].

Aiming to improve storage efficiency, Leesakul et al. propose a dynamic deduplication scheme in cloud storage systems that aims to preserve redundancy for fault tolerance. Deduplication mechanisms in cloud systems imply a static scheme that limits their applicability to the dynamic nature of the data in this system. Therefore, it emphasizes the need to strike a balance between changing storage efficiency and fault tolerance requirements. Furthermore, a dynamic deduplication scheme for cloud storage is proposed to improve performance in cloud storage systems. The number of copies of files is dynamically changed according to the changing Quality of Service (QoS) level. Experimental investigations show that the performance of the proposed system is significantly improved and can cope with the scalability problem [8].

Fan et al. consider an encrypted deduplication mechanism that enables the cloud storage server to eliminate duplicate ciphertexts and improve privacy protection. A feasible encrypted deduplication mechanism is proposed where all data is stored in the form of a cipher structure consisting of a control block, a transformation block, an activation block and a cipher block.

The cloud storage server can define duplicate cipher structures with control blocks. It is then mentioned that it can transform duplicate activation blocks. Each data owner of duplicate cipher structures corresponding to the same plaintext can share the same copy of the cipher blocks. As a result, the cloud storage server can avoid wasting storage space by storing only one copy of the duplicate cipher block [9].

In a study by Park et al. on neural networks and deduplication, a new reference search technique, DeepSketch, was used. In this way, an average of 21% more success was achieved compared to the delta compression technique [10].

In a study by Tarun et al. on machine learning and deduplication in distributed systems, it was reported that repeated data entry of stored data poses a major problem for query processing and data analysis. To minimize this problem, an advanced machine learning based algorithm is proposed to detect repeated data entries and improve efficiency [11].

3. METHODS

3.1. Cloud computing, Data Storage, Data Security, Multi-Device Access and Cost Effectiveness

Cloud computing refers to the provision of services over the internet. Depending on a cloud computing service provider, users can access many different services over the internet for a fee. These services include software as a service (SAAS), infrastructure as a service (IAAS) and platform as a service (PAAS). IaaS allows users to create their own virtual machines and storage. This allows users to install their own operating systems and applications. PaaS provides a platform for users to develop and deploy their own applications. Thus, users can use the infrastructure provided by the cloud computing service provider while developing their own applications. SaaS aims to enable users to use applications over the internet. These applications are usually accessible through a browser and do not need to be downloaded or installed by users [12]. Examples include applications such as Google Docs or Microsoft Office 365.

Data storage is the general name given to the process of storing and retaining information. Data storage systems are physical devices and software used to store users' data. Data storage systems have features such as keeping data secure, fast access and management. Cloud computing services also include data storage services. Users can store their data for a certain fee, connected to cloud computing service providers over the internet [13].

The use of cloud computing services brings some risks in terms of data security. These risks include the ability to transmit and store data over the internet, the inability to control access to data, the possibility of damaging data, and the loss of data [4]. Therefore, it is necessary to take precautions regarding data security when using cloud computing services. Measures that can be taken for data security include encryption, authentication, authorization, backup and update [9]. It is also important to investigate the security measures and data protection policies of the cloud computing service provider and to choose a reliable service provider in this regard [14].

Cloud computing services allow users to access their data from any device over the internet thanks to data storage systems. In this way, users can access their data from any device with an internet connection from their home, workplace or even while traveling [15]. This is referred to as data multi-device access. Data multi-device access aims to make it easier and faster for users to access their data. Data multi-device access is made possible through the use of cloud

computing services. Users can benefit from data storage services over the internet for a certain fee depending on the cloud computing service provider [16]. Thus, users can access their data from any device over the internet. However, data multi-device access brings some risks in terms of data security. Therefore, it is necessary to take precautions for data security when using data multi-device access.

Cloud computing allows a software or service to be used over the internet. Instead of purchasing their own software and hardware, this method enables organizations to outsource services by paying a fee for use when needed. With this method, organizations can use software and hardware without having to invest upfront. The cost-effectiveness of cloud computing is a major advantage for organizations. For example, if an organization purchases its own software and hardware, it will only use a portion of that investment and the rest may be idle. However, when using cloud computing, the organization can use the software and hardware by paying only when needed. In this way, organizations can benefit from services in a less costly way instead of making upfront investments. Cloud computing also reduces additional costs for organizations such as maintenance and updates. Cloud providers maintain and update the software and hardware themselves and offer these services to organizations for a fee [5]. Thus, organizations can use resources such as time and money allocated to the maintenance and updating of their own software and hardware in other areas.

3.2. Artificial Intelligence and Data Analytics

Artificial Intelligence aims for a machine or program to have the ability to think and learn like a human. Machine learning is the ability of a machine to improve itself using data. It enables machine learning systems to become more effective and deliver better results throughout the learning process. This goal involves automating the processes of data collection, learning and decision making. Data analysis is the process of collecting, organizing and making sense of data and producing usable information. Data analysis is used to understand data collected from many different data sources and to generate meaningful information. Data analytics is often based on technologies such as artificial intelligence and machine learning. There are important differences between these two concepts [17]. This data can take various forms. However, the most used data types are tables and graphs. Data analysis is usually done using advanced data analysis techniques. These techniques include regression, clustering and classification. Artificial intelligence and data analysis are used in many different industries and play an important role in these fields. For example, in a healthcare company, data analytics can be used to predict the spread of diseases and take preventive measures. Likewise, in a retail company, data analytics can be used to predict customer behavior and take preventive measures.

3.3. Integration of Artificial Intelligence and Cloud Computing

Artificial intelligence and cloud computing are technologies that match each other very well. They can be used by integrating with each other. If an AI application needs data processing, it is possible to store and process that data with cloud computing services. It can enable the application to meet its data processing requirements and continue to operate without the need for more data processing power as it grows. Furthermore, AI applications often work with large data sets and require large data centers to store and process this data [18]. Cloud computing is ideal for meeting these data processing needs. This is because data processing services can be accessed without the need to own data centers. Cloud computing aims to meet the data processing needs of AI applications and enable them to continue to operate without the need for more data processing power as they grow.

3.4. Big Data and Types

Big data refers to large, complex data sets that are difficult to process with traditional data management tools and methods. This is because these tools and methods are inadequate due to factors such as the volume, velocity or variety of data. [19]. These datasets often come from a variety of sources, including social media, transactional data, and sensors [20]. The data can be structured or unstructured. The term big data is often used to describe the challenges and opportunities of working with large datasets, as well as the tools and technologies used to store, process and analyze them [12].

There are several types of big data, each with its own characteristics and challenges. Some common types of big data are; Structured data: Data that is organized in tabular form and can be easily processed. Unstructured data: Data that does not have a specific order. Semi-structured data: Data that is a combination of structured and unstructured data. Examples include emails or web pages. Multimedia data: Refers to data in the form of pictures, videos or audio recordings. Sensor data: Refers to data generated by sensors or devices such as IoT devices, wearables [5]. Transaction data: Data generated as a result of transactions, such as financial or retail data.

3.5. Deduplication of Big Data and Deduplication Architectures

Deduplication is the process of identifying and removing duplicate records from a dataset. This is often an important step in the process of working with big data, as large datasets can contain a significant number of duplicate records. Deduplication can be useful for a variety of purposes, including reducing the storage space required for a dataset, improving the accuracy of analytics and machine learning models, and simplifying the process of analyzing data [21].

Deduplication architectures can be divided into three classes. Inline Deduplication: In this architecture, data is deduplicated as it is written to the storage system. The system compares incoming data with existing data in real time and eliminates duplicates before the data is stored. This approach requires more processing power and can impact system performance. However, it ensures the most efficient use of storage space. Post-Process Deduplication: In this architecture, data is stored in its original form and deduplication is performed later in a separate process. This approach requires fewer resources than inline deduplication but may require more storage. It can result in longer backup and restore times. Hybrid Deduplication: This architecture combines inline and post-process deduplication. Inline deduplication is used for data that is accessed or written frequently, while post-process deduplication is used for data that is accessed less frequently.

Deduplication works by identifying and removing duplicate records from a dataset. There are several different approaches to deduplication depending on the characteristics of the data and the goals of the deduplication process. A common approach to deduplication is record linkage, which involves identifying records that refer to the same real-world entity, even if the records do not match exactly. It can be done using various techniques such as matching records based on common attributes such as name and address, or using more advanced techniques such as machine learning to identify patterns in the data that indicate that two records refer to the same entity [22]. Another approach to deduplication is hash-based deduplication, which involves creating a unique hash value for each record and comparing the hash values to identify duplicates. It can be an effective way to identify duplicates. However, it is important to ensure

that the hash function used is sufficient to distinguish all unique records in the dataset. Ordered list deduplication involves sorting the records in a dataset and then identifying and removing duplicates based on the sorted order. This method can be an effective way to identify duplicates and requires sorting the entire dataset. This can be time-consuming for large datasets. Probabilistic deduplication involves using statistical techniques to identify and remove duplicates based on the probability that two records refer to the same real-world entity [22], [23]. As such, it can be an effective way to identify duplicates. However, it may not be as accurate as other approaches as it relies on statistical estimates rather than exact matches. In general, the most effective approach to deduplication will depend on the characteristics of the dataset and the goals of the deduplication process.

3.6. How Data Deduplication Works

If a user stores the same file in multiple locations, deduplication stores only one copy of the file and all other copies are saved as references to this copy. This means that when backing up or storing data, much less data is sent and storage space is used more efficiently. Technically, deduplication eliminates duplicate blocks of data. It stores unique data blocks at the 4KB block level within a volume and across all volumes in the aggregate. It then relies on unique digital signatures for all 4 KB data blocks. The deduplication engine examines the newly incoming blocks, develops a digital signature, and stores it in a hash store of the digital signature when data is written to the system. After the digital signature is calculated, a search is performed on the hash store. The block of data that matches the repeated digital signature is examined in the cache in case it matches a digital signature in the hash store [24]. If a match is detected, a byte-by-byte comparison between the valid data block and the digital signature is performed as verification. The receiving block is shared with the matching digital signature without writing the receiving block to disk during verification. Only the metadata is updated to keep track of the sharing details. If the transmitting block is not found in the cache, it is pre-cached from disk and compared byte-by-byte to ensure an exact match. Without actually writing to disk, the receiving block is marked as a duplicate during verification. Metadata is updated to keep track of sharing details. Likewise, the background deduplication engine runs. It searches all data blocks in bulk and removes duplicates by comparing block digital signatures and performing byte-by-byte comparison to eliminate false positives [25]. This method also ensures that no data is lost during the deduplication process. Figure 1 visually illustrates how deduplication works.

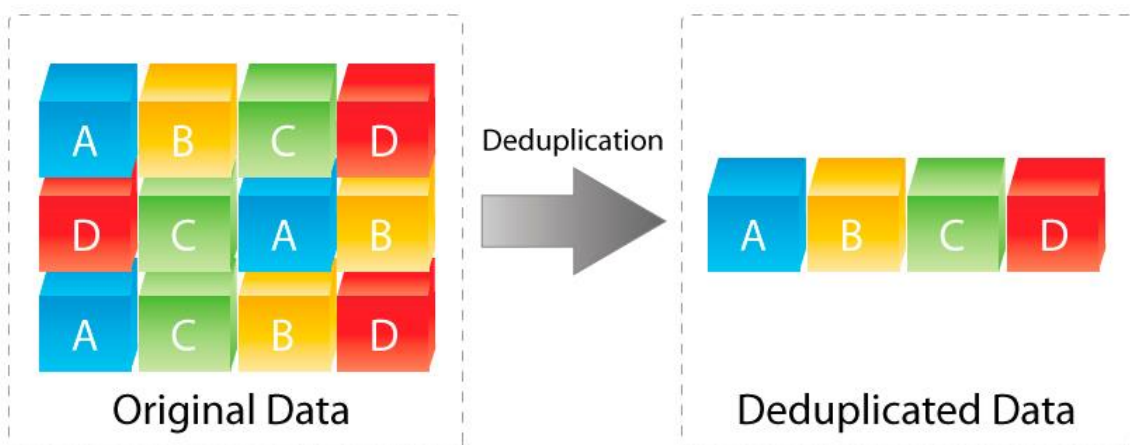


Figure 1. Example of data deduplication [26]

4. RESULTS AND DISCUSSION

Today, deduplication is very important. Because it reduces your storage requirements, saves you money and reduces the amount of bandwidth used to move data to and from remote storage sites. While deduplication can reduce storage requirements by up to 95% in some cases, it can be affected by factors such as the type of data you are trying to deduplicate. Even if your storage requirements are less before deduplication than after deduplication, it can reduce your cost of data storage and significantly increase your bandwidth availability.

Once the deduplication process is complete, it is possible to use the deduplicated dataset to build predictive models. The most appropriate type of model will depend on the nature of the data and the objectives of the analysis. Some common types of predictive models that can be built from de-duplicated data can be categorized into 4 groups. If we briefly discuss these models; Regression models: Can be used to predict continuous outcomes based on a set of input variables. Classification models: Can be used to predict categorical outcomes based on a set of input variables. Clustering models: These models can be used to identify groups of similar records in the data. Anomaly detection models: Can be used to identify unusual or unexpected patterns in data.

Prediction models created by combining artificial intelligence and big data are models that aim to predict future events or outcomes by analyzing large data sets. These prediction models are created using artificial intelligence methods and big data technologies. For example, a prediction model can analyze a large dataset of customer buying behaviors to predict when and what a customer will buy in the future. These prediction models can be used in a variety of different fields. Finance: A finance company can use AI and big data to predict the future payment behavior of customers. Health: A healthcare company can use AI and big data to predict future health issues. Marketing: A marketing company can use AI and big data to predict customer buying behavior. Energy: An energy company can use AI and big data to predict future energy demand. Forecasting models built using AI and big data are often very comprehensive and powerful and can analyze large data sets collected from a wide range of different data sources. As a result, these models can often predict future events and outcomes with very high accuracy.

As can be seen from the comparison in Table 1, a comparison of the performance of machine learning algorithms based on artificial intelligence is given. The reasons for the different performances are due to the fact that the data sets used in the study were not used with the correct machine learning techniques. It is thought that the success rate will increase with the development of machine learning algorithms and artificial intelligence.

Table 1. Success comparison table on different studies.

Author	Methodology	Performance
Keleş ve Nevcihan [1]	Deduplication by text similarity	Medium
Pg ve ark. [2]	Deduplication with convergent and modified elliptic curve cryptography algorithms	Medium
Jiang ve ark. [3]	Creating a new proof of ownership scheme using the Bloom filter	Medium
Yang ve ark. [4]	Deduplication with decision tree algorithm	High
Barik ve ark. [5]	Unification with GeoBD 2 schema	High
Vijayalakshmi ve Jayalakshmi [6]	Deduplication techniques	Low
Manogar ve Abirami [7]	Stack-based deduplication	Medium
Leesakul ve ark. [8]	Dynamic deduplication	Medium
Fan ve ark. [9]	Deduplication of duplicate passwords	Medium
Park ve ark. [10]	Deduplication with DeepSketch technique	High
Tarun ve ark. [11]	Deduplication using machine learning algorithms	High

5. CONCLUSIONS

Deduplication and artificial intelligence are two increasingly important technologies used in almost all industries today. Deduplication and AI complement each other in a number of ways, notably in improving data quality, reducing storage costs and enhancing data analytics. Deduplication is the process of processing and analyzing large amounts of data and extracting meaningful information. Artificial intelligence is the ability of computer systems to think and make decisions in a human-like manner. An AI system continuously scans the dataset and can detect and automatically eliminate multiple copies of the same data. This is a crucial step in the deduplication process. In the AI deduplication process, various methods can be proposed that can be used to process and understand the dataset. An AI system can identify which data is important in the dataset and by highlighting them, it can optimize the deduplication process. By transforming the data obtained in the deduplication process into meaningful information, AI can facilitate the understanding and use of the data. Artificial intelligence can quickly access large amounts of data using deduplication algorithms. Thus, it can make the process more efficient and effective. From another perspective, deduplication helps AI models find similar or identical information in the data sets used during training. This method helps to organize and clean the data sets. This leads to better results when training AI models. Deduplication is especially important for very large data sets. Duplication of information can slow down the training process of AI models and reduce the likelihood of accurate results. Deduplication helps to eliminate such repetitive information. In this way, the training of AI models can be faster and more accurate. In addition to improving the accuracy and efficiency of deduplication, AI can

also improve data analysis by identifying relationships and correlations between data points that human analysts may not immediately recognize. This can help organizations extract more value from their data, leading to more informed decision-making and better business outcomes. As you can see, artificial intelligence and data deduplication feed off each other and are inseparable. If we use a program to analyze a data set, it must have deduplication and artificial intelligence in the background. Today, these two are among the constants of data analysis. Today, as the size of our data increases, we need new storage spaces. It becomes important to reduce the volume of our data in storage areas. It is possible to achieve this with data deduplication. This study aims to provide a different perspective to researchers who will study the importance of deduplication and artificial intelligence against each other. In future studies, it is aimed to experimentally study how important deduplication is.

REFERENCES

- [1] Keleş, Ü., & Nevcihan, D. U. R. U. (2021). Metin Benzerliği Algoritmaları ile Veri Tekilleştirme: Oteller Veri Tabanında Bir Uygulama. *Türkiye Bilişim Vakfı Bilgisayar Bilimleri ve Mühendisliği Dergisi*, 14(2), 86-98.
- [2] PG, S., RK, N., Menon, V. G., Abbasi, M., & Khosravi, M. R. (2020). A secure data deduplication system for integrated cloud-edge networks. *Journal of Cloud Computing*, 9(1), 1-12.
- [3] Jiang, S., Jiang, T., & Wang, L. (2017). Secure and efficient cloud data deduplication with ownership management. *IEEE Transactions on Services Computing*, 13(6), 1152-1165.
- [4] Yang, X., Lu, R., Choo, K. K. R., Yin, F., & Tang, X. (2017). Achieving efficient and privacy-preserving cross-domain big data deduplication in cloud. *IEEE transactions on big data*, 8(1), 73-84.
- [5] Barik, R. K., Patra, S. S., Patro, R., Mohanty, S. N., & Hamad, A. A. (2021, March). GeoBD2: Geospatial big data deduplication scheme in fog assisted cloud computing environment. In *2021 8th International Conference on Computing for Sustainable Global Development (INDIACom)* (pp. 35-41). IEEE.
- [6] Vijayalakshmi, K., & Jayalakshmi, V. (2021, April). Analysis on data deduplication techniques of storage of big data in cloud. In *2021 5th International Conference on Computing Methodologies and Communication (ICCMC)* (pp. 976-983). IEEE.
- [7] Manogar, E., & Abirami, S. (2014, December). A study on data deduplication techniques for optimized storage. In *2014 Sixth International Conference on Advanced Computing (ICoAC)* (pp. 161-166). IEEE.
- [8] Leesakul, W., Townend, P., & Xu, J. (2014, April). Dynamic data deduplication in cloud storage. In *2014 IEEE 8th International Symposium on Service Oriented System Engineering* (pp. 320-325). IEEE.
- [9] Fan, C. I., Huang, S. Y., & Hsu, W. C. (2015, May). Encrypted data deduplication in cloud storage. In *2015 10th Asia Joint Conference on Information Security* (pp. 18-25). IEEE.
- [10] Park, J., Kim, J., Kim, Y., Lee, S., & Mutlu, O. (2022). {DeepSketch}: A New Machine {Learning-Based} Reference Search Technique for {Post-Deduplication} Delta Compression. In *20th USENIX Conference on File and Storage Technologies (FAST 22)* (pp. 247-264).
- [11] Tarun, S., Bath, R. S., & Kaur, S. (2021, December). A Scheme for Data Deduplication Using Advance Machine Learning Architecture in Distributed Systems. In *2021 International Conference on Computing Sciences (ICCS)* (pp. 53-60). IEEE.
- [12] Dokuz, A. Ş., & Çelik, M. (2017). Bulut Bilişim Sistemlerinde Verinin Farklı Boyutları Üzerine Derleme. *Niğde Ömer Halisdemir Üniversitesi Mühendislik Bilimleri Dergisi*, 6(2), 316-338.
- [13] Çelik, K. (2021). Bulut Bilişim Teknolojileri. *Bartın Üniversitesi İktisadi ve İdari Bilimler Fakültesi Dergisi*, 12(24), 436-450.
- [14] Jamsa, K. (2022). *Cloud computing*. Jones & Bartlett Learning.

- [15] Hurwitz, J. S., & Kirsch, D. (2020). *Cloud computing for dummies*. John Wiley & Sons.
- [16] Singhal, S., Sharma, P., Aggarwal, R. K., & Passricha, V. (2018). A global survey on data deduplication. *International Journal of Grid and High Performance Computing (IJGHPC)*, 10(4), 43-66.
- [17] Alonso, J. M., & Casalino, G. (2019, June). Explainable artificial intelligence for human-centric data analysis in virtual learning environments. In *International workshop on higher education learning methodologies and technologies online* (pp. 125-138). Springer, Cham.
- [18] Gill, S. S., Tuli, S., Xu, M., Singh, I., Singh, K. V., Lindsay, D., ... & Garraghan, P. (2019). Transformative effects of IoT, Blockchain and Artificial Intelligence on cloud computing: Evolution, vision, trends and open challenges. *Internet of Things*, 8, 100118.
- [19] Demirel, D., Das, R., & Hanbay, D. (2019, September). Büyük veri üzerine perspektif bir bakış. In *2019 International Artificial Intelligence and Data Processing Symposium (IDAP)* (pp. 1-9). IEEE.
- [20] Süzen, A. A., & Kayaalp, K. (2019). Büyük Verilerde Gizlilik Tabanlı Yaklaşım: Federe Öğrenme. *International Journal of 3d Printing Technologies and Digital Industry*, 3(3), 297-304.
- [21] Xu, L. J., Hao, R., Yu, J., & Vijayakumar, P. (2021). Secure deduplication for big data with efficient dynamic ownership updates. *Computers & Electrical Engineering*, 96, 107531.
- [22] Premkamal, P. K., Pasupuleti, S. K., Singh, A. K., & Alphonse, P. J. A. (2021). Enhanced attribute based access control with secure deduplication for big data storage in cloud. *Peer-to-Peer Networking and Applications*, 14(1), 102-120.
- [23] Kumar, N., & Jain, S. C. (2019). Efficient data deduplication for big data storage systems. In *Progress in Advanced Computing and Intelligent Engineering* (pp. 351-371). Springer, Singapore.
- [24] Savić, I., & Lin, X. (2021, November). The Analysis and Implication of Data Deduplication in Digital Forensics. In *International Symposium on Cyberspace Safety and Security* (pp. 198-215). Springer, Cham.
- [25] Wu, H., Wang, C., Fu, Y., Sakr, S., Zhu, L., & Lu, K. (2017). Hpdedup: A hybrid prioritized data deduplication mechanism for primary storage in the cloud. *arXiv preprint arXiv:1702.08153*.
- [26] URL-1 (2022). <https://www.hsb.nl/the-importance-of-deduplication-and-adjudication-in-identity-management-solutions/> (Erişim tarihi 12.02.2022)



Research Article

UTILIZING DEEP LEARNING AND DATA AUGMENTATION FOR EARLY DETECTION OF EYE DISEASES IN PETS

Authors: Nilgün Şengöz 

To cite to this article: Şengöz, N. (2023). UTILIZING DEEP LEARNING AND DATA AUGMENTATION FOR EARLY DETECTION OF EYE DISEASES IN PETS . International Journal of Engineering and Innovative Research ,5(2) , p112-122 . DOI: 10.47933/ijeir.1227798

DOI: 10.47933/ijeir.1227798

To link to this article: <https://dergipark.org.tr/tr/pub/ijeir/archive>



International Journal of Engineering and Innovative Research

<http://dergipark.gov.tr/ijeir>

UTILIZING DEEP LEARNING AND DATA AUGMENTATION FOR EARLY DETECTION OF EYE DISEASES IN PETS

Nilgün Şengöz^{1*} 

¹Burdur Mehmet Akif Ersoy University, MAKÜ-BAKA Technopark, Burdur, Turkey.

*Corresponding Author: nilgunsengoz@mehmetakif.edu.tr
(Received: 01.01.2023; Accepted: 12.03.2023)

<https://doi.org/10.47933/ijeir.1227798>

ABSTRACT: This paper presents a deep learning algorithm for the diagnosis of eye diseases, which is taken from cats and dogs, using data augmentation. The database of eye images was collected from cell phone cameras, and with data augmentation techniques were used to increase the number of samples. The performance of the algorithms was evaluated on the original dataset of 146 diseased and 255 healthy images. The results showed that the VGG16 algorithm achieved a classification accuracy of 99.25% before data augmentation, which was significantly higher than the accuracy of existing methods. Furthermore, after the data augmentation again VGG16 model has significant performance metrics that are 99.9% than other algorithms. The proposed algorithm can be used to accurately diagnose various eye diseases, which can potentially improve the quality of care for patients.

Keywords: Classification, Eye disease, Deep Learning, Data augmentation.

1. INTRODUCTION

Deep learning is a type of artificial intelligence that involves the use of neural networks to learn from and make predictions about data. It is a subset of machine learning and is based on the idea of artificial neural networks, which are modeled after the neurons and synapses of the human brain. Deep learning algorithms are used in various areas, including computer vision, natural language processing, voice recognition, and robotics. Deep learning algorithms are designed to learn from large amounts of data, and can be used to identify patterns and make predictions. For example, deep learning algorithms can be used to identify objects in images, recognize spoken words, and even control robots.

Deep learning is also used to improve the accuracy and speed of other machine learning algorithms, such as those used in computer vision and natural language processing. Deep learning algorithms use layers of neurons to process data. Each layer of neurons is connected to the next layer and learns from the data that it receives. As the data passes through each layer, the neurons are adjusted so that the deeper layers learn more complex features of the data. This allows the algorithm to learn more complex patterns and make better predictions. Deep learning algorithms have been used in many applications, such as recognizing images, understanding natural language, and controlling robots. Deep learning algorithms are becoming increasingly powerful and are able to learn from large amounts of data quickly and accurately, making them an ideal tool for many applications.

Eye diseases, which are frequently seen in cats and dogs, are an alarming and early diagnosis is an extremely important issue. Animals can suffer from a variety of eye diseases, ranging from

minor irritations to life-threatening conditions. The most common cause of eye diseases in animals is trauma. Injuries, such as scratches, bruises, or foreign objects in the eye, can lead to infection or other complications. In addition, there are numerous infectious diseases of the eye, such as conjunctivitis, that can be passed between animals. Allergies, genetic conditions, and exposure to toxins can also lead to eye problems.

When it comes to eye diseases in cats and dogs, there are a few potential issues that pet owners should be aware of to help keep their pets healthy. Cats are more prone to feline herpesvirus-1 (FHV-1) and feline calicivirus (FCV). FHV-1 is a viral infection that can cause severe inflammation and ulceration of the cornea. FCV is a highly contagious virus that causes inflammation of the conjunctiva and cornea, which can lead to ulceration. Both FHV-1 and FCV can cause blindness if left untreated. Dogs, on the other hand, can be affected by a variety of eye conditions, including glaucoma, dry eye, and cataracts. Glaucoma is a condition that occurs when fluid pressure in the eye increases and damages the optic nerve. Dry eye occurs when the tear glands do not produce enough tears to keep the eyes lubricated. Cataracts are caused by a buildup of proteins in the lens of the eye, which can lead to vision loss. Treatment for eye diseases in pets may include antibiotics, anti-inflammatory medications, or even surgery. It is important for pet owners to have their pets regularly examined by a veterinarian to check for any signs of eye disease. Early diagnosis and treatment are key to preventing vision loss or blindness [1].

The symptoms of eye diseases in animals vary depending on the condition, but some of the most common signs include redness, swelling, squinting, discharge, and excessive tearing. If your pet is exhibiting any of these symptoms, it is important to seek veterinary care as soon as possible, as some eye diseases can progress rapidly and cause permanent damage.

In this context, it has become necessary to develop a user-oriented system for the early diagnosis of diseases that affect the quality of life of our friendly friends, whom we consider as members of our family, and the early diagnosis of some diseases that may be the precursors of some serious diseases.

With the developing technology, mobile phone cameras can now take professional camera image quality shots up to 50 megapixels. At this point, this situation constitutes the main idea of the study. In other words, it is planned to classify the disease by using the deep learning algorithm of the photos taken with the mobile phone camera.

The main subject of this study is the use of diseased and healthy eye photos of cats and dogs, collected by mobile phone cameras from veterinary clinics, in deep learning algorithms. In the study, both an original dataset is used and the images collected with a mobile phone camera are used in deep learning.

In the original dataset, 146 photographs were taken for the diseased class and 255 photographs were taken for the healthy class. As it is known, deep learning algorithms work with a large number of data sets and produce meaningful results. In this context, some data augmentation methods were followed in this study.

What makes the study different is that first of all, different deep learning algorithms were tried without increasing the data and the results were recorded. Afterwards, using the TensorFlow data augmentation library, the number of diseased eye photos was replicated from 146 to 354 using data augmentation techniques and reached 500. The same data augmentation processes

were also applied to healthy eye photographs, and 245 photographs were produced from 255 original photographs and the number reached 500 again. In summary, 500 photographs were obtained for each class using data duplication techniques.

As stated before, a comparison was made between deep learning algorithms applied without data augmentation techniques and the same algorithms applied using data augmentation techniques. At this point, the effect of data replication processes on deep learning algorithms has been observed. The deep learning algorithms used in this study are VGG16, InceptionV3, ResNet50, Xception, DenseNet121, and EfficientNetB0.

Shan and Li [2] proposed a two-layer stacked sparse autoencoder model for automatic detection of microaneurysm in images of the posterior part of the eye (fundus). In the proposed model, they used the unsupervised learning method to obtain high-level features from the pixel level. In a model, binary classification can be performed with logistic regression. However, in cases where the model needs more class labels, the softmax algorithm, which is the generalized version of logistic regression, can be used in supervised learning methods as well as in learning unsupervised features together with deep learning methods.

An Extreme Learning Machine-ELM based model consisting of four stages based on macro and micro feature extraction was proposed for Diabetic Retinopathy detection by Deepa et al. [3]. The performance of the proposed model is compared with the performance of ANN and KNN based classifier models.

Güldemir et al., in their study in 2021, OCT- Optical Coherence Tomography images used for Age Related Macular Degeneration (AMD) disease was detected using Xception, VGG16, InceptionV3 and ResNet50 deep neural network models trained with Convolutional Neural Network (CNN) architecture [4]. In another study, Tasmin et al., suggested the use of MobileNetV2, ResNet50 and Xception deep neural network models in the classification of normal, Drusen, AMD, Diabetic Macular Edema (DME) of the retina based on CNN architecture using OCT images [5].

As seen in the literature studies, images taken with professional devices were used in deep learning algorithms. And yet, with the user-oriented and developing technology, it has been determined that the photos taken using a mobile phone camera have not been used in deep learning architectures before. The different aspects of this study make an important contribution to the literature by using both eye diseases in cats and dogs and photographs taken with a mobile phone camera.

The article is organized as follows; In the second part, focuses on dataset studies on the subject. Section 3 focuses on deep learning methods applied for disease classification. Sections 4 and 5 include results and discussion. Section 6 contains the conclusion part.

2. METHODS

Different deep learning algorithms have been used in this study, emphasizing the importance of data augmentation techniques. There are 146 data belonging to the diseased class and 255 data belonging to the healthy class from the images originally taken with the mobile phone camera.

Samsung A50 mobile phone was used to obtain the original dataset. Eye photos taken with the permission of cat and dog owners are divided into two classes; diseased and healthy. This study is not subject to any ethics committee permission as it is only a photo shoot.

As stated in the introduction, the original dataset was first used in deep learning algorithms in the study. Afterwards, 354 pieces of data were augmented in the diseased class and 245 in the healthy class using data augmentation techniques, and these were used again in deep learning algorithms and the results were compared. Using the Tensorflow data augmentation library, the data augmented were 500 in the healthy class and 500 in the diseased class. The methods used from the Tensorflow data augmentation library are as follows; Flip left right, 90-degree rotation and Saturation techniques.

Flip left right operation which is augmentation technique, randomly flips an image from left to right, allowing for more diverse data to be used in a machine learning model. This is especially useful when training a model to recognize objects in images that may appear in different orientations. It is also useful when training a model to recognize objects in a scene that may appear from different points of view. By performing Flip Left Right data augmentation, the model will be better prepared to recognize objects in images regardless of the orientation of the image.

One of the most commonly used transformations is the 90-degree rotation. This transformation involves rotating an image by 90 degrees clockwise and counterclockwise. This transformation can be used to create new data points in the dataset without changing the object's original characteristics. Using the Tensorflow library, the 90-degree rotation data augmentation can be easily implemented. The library provides a function, which takes the image and rotates it by the specified angle. This function can be used to rotate the image by 90 degrees in either the clockwise or counterclockwise direction.

Saturation data augmentation is a type of data augmentation technique used to improve the accuracy of a deep learning model. It is a type of preprocessing technique used to increase the number of training samples by altering the saturation of the input images. Saturation data augmentation can be implemented using Tensorflow, a popular open-source library for deep learning. Saturation data augmentation can also be used to reduce overfitting in the model. By increasing the variation of the input images, the model is less likely to overfit on a single set of data. This helps the model to generalize better and to produce more accurate results. Saturation data augmentation is a powerful tool for improving the accuracy of deep learning models. It can be implemented using the Tensorflow library, which provides a number of preprocessing and augmentation functions that can be used to alter the saturation of input images.

2.1. VGG16 Algorithm

VGG16 is a convolutional neural network (CNN) architecture developed by the Visual Geometry Group (VGG) at Oxford University for the ImageNet Large Scale Visual Recognition Challenge in 2014 [6]. The network is 16 layers deep and consists of convolutional layers, pooling layers, and fully connected layers. It was one of the first CNNs to demonstrate good performance on the ImageNet dataset. VGG16 is a popular choice for transfer learning, which is the process of using a pre-trained model on a new dataset. VGG16 has been used in many applications, including image classification, object detection, and object recognition.

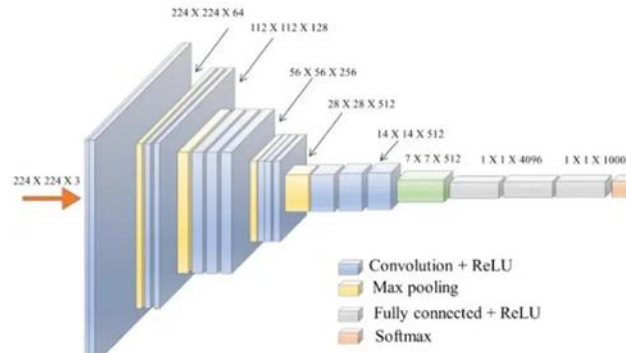


Figure 1. VGG16 Algorithm [7]

2.2. ResNet Algorithm

ResNet (Residual Network) is a type of deep learning neural network architecture designed to simplify the training of very deep networks. It was first introduced by Microsoft researchers in 2015 and has since become a widely used architecture for computer vision tasks such as image classification and object detection [8].

The key idea of ResNet is to introduce a "residual" connection between layers in a neural network. These residual connections are short-cuts that allow the network to learn more quickly and accurately. In addition, the residual connections help to reduce the vanishing gradient problem, which can occur when training very deep networks.

The basic building block of a ResNet is called a residual block. A residual block contains two convolutional layers, a batch normalization layer, and a ReLU activation layer. The output of the first convolutional layer is then added to the output of the second convolutional layer. This addition helps the network to learn more quickly and accurately by allowing gradients to flow more easily through the network.

The ResNet architecture can be used for a variety of computer vision tasks. It has been used to achieve state-of-the-art results in image classification and object detection tasks. In addition, it has been used for tasks such as semantic segmentation and image generation.

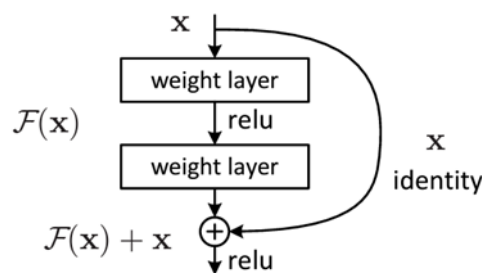


Figure 2. ResNet Algorithm

2.3. InceptionV3 Algorithm

InceptionV3 is a deep convolutional neural network (CNN) developed by Google and released in 2015 [9]. It is a class of deep learning architectures that are used for image recognition and object detection. InceptionV3 is the third incarnation of the Inception model, which is based on the concept of a "GoogLeNet" and uses "inception blocks" to reduce the number of parameters

in the network. It is one of the most accurate models for image classification and is the basis of many popular applications. InceptionV3 is trained using the ImageNet dataset and is able to identify over 1000 different objects. In addition to image classification, it can also be used for object detection, semantic segmentation, and image retrieval. The model is available for use in the TensorFlow library and can be used to develop new applications.

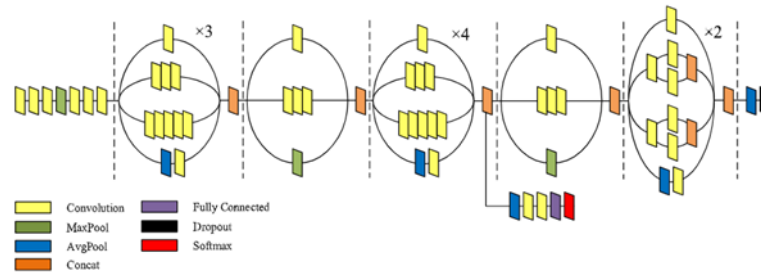


Figure 3. InceptionV3 Algorithm [10]

2.4. Xception Algorithm

Xception is a deep convolutional neural network architecture developed by François Chollet and published in the journal arXiv in 2016 [11]. It was developed as an improved version of the Inception architecture, which was widely used for image classification. Xception utilizes depthwise separable convolutions to reduce the number of parameters and computational cost, while still achieving high accuracy. Its primary benefit is that it requires fewer parameters and less computation than Inception, allowing it to train faster and more efficiently. Additionally, Xception is capable of training without requiring large amounts of memory. As a result, it has been widely used in many computer vision tasks, including object classification, segmentation, and object detection.

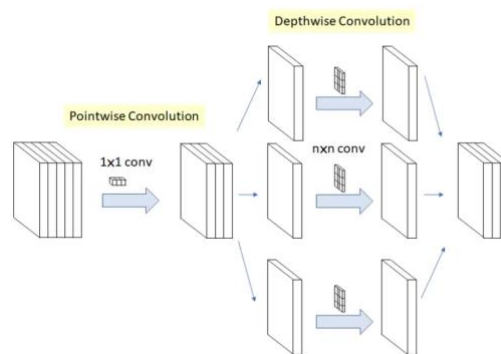


Figure 4. Xception Algorithm [11]

2.5. DenseNet121 Algorithm

DenseNet121 is a convolutional neural network architecture which is developed by Gao Huang, Zhuang Liu, Kilian Q. Weinberger, Laurens van der Maaten and Chen Change Loy [12]. DenseNet121 is a type of deep learning architecture that is used for image recognition tasks and is part of the DenseNet family of neural networks. The network is made up of 121 layers, with each layer connected to every other layer in a feed-forward fashion. The network is characterized by its dense connections between layers, which allow for a more efficient flow of information and better feature extraction. The network is trained on the ImageNet dataset, which is a large dataset of images of various objects. This allows the model to recognize objects in images and classify them accurately. The network is also used for transfer learning, which is

a technique that allows the model to be used for other tasks such as object detection, semantic segmentation, and so on.

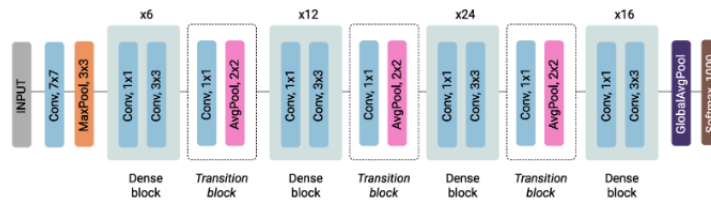


Figure 5. DenseNet121 Algorithm [13]

2.6. EfficientNetB0 Algorithm

EfficientNetB0 is a convolutional neural network (CNN) model developed by Google AI research team, which was introduced in 2019 [14]. The aim of the model is to improve the accuracy of the model while maintaining its efficiency. The model is based on a novel architecture called EfficientNet which incorporates three innovative techniques: compound scaling, depth-wise separable convolutions, and a global bottleneck.

Compound scaling adjusts the network width, depth, and resolution simultaneously, allowing the model to use fewer parameters while achieving higher accuracy. Depth-wise separable convolutions reduce the number of parameters without compromising accuracy, while the global bottleneck helps reduce the number of nodes in the network.

The model is trained on the popular ImageNet dataset and achieves a top-1 accuracy of 76.30% and a top-5 accuracy of 92.85%. It also performs well on other datasets like CIFAR-10, CIFAR-100, and SVHN. EfficientNetB0 is a great model for small-scale applications due to its efficient architecture and high accuracy. It also offers a good trade-off between accuracy and speed, making it suitable for real-time applications.

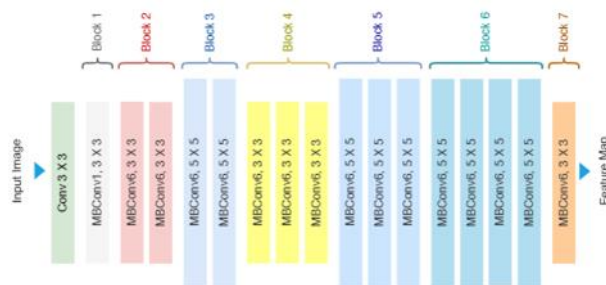


Figure 6. EfficientNetB0 Algorithm [15]

3. EXPERIMENTAL

The above-mentioned deep learning algorithms were first tested on the original dataset and the performance results were recorded. Afterward, the same deep learning algorithms were tried again on the dataset replicated with data augmentation techniques, and the results were recorded for comparison with the original dataset results. A confusion matrix was used to evaluate the results.

The confusion matrix is a matrix of true positive (True Positive-TP), true negative (True Negative-TN), false positive (False Positive-FP), and false negative (False Negative-FN) terms.

TP represents instances where the actual and estimated value is 1. TN refers to instances where the actual and estimated value is 0. The FP shows examples, where the true value is 0 and the estimated value, is 1. FN, on the other hand, indicates instances where the true value is 1 and the estimated value is 0. It is expressed by the performance metrics used in the evaluation of the performance of the eye disease diagnostic models created in the study and calculated according to the confusion matrix.

$$\text{Classification Accuracy} = \frac{TP+TN}{TP+TN+FP+FN} \quad (1)$$

$$\text{Sensitivity (Recall)} = \frac{TP}{TP+FN} \quad (2)$$

$$\text{Precision} = \frac{TP}{TP+FP} \quad (3)$$

$$\text{F1 Score} = \frac{2 * \text{Precision} * \text{Recall}}{\text{Precision} + \text{Recall}} \quad (4)$$

The performance of the proposed model for diagnosing eye disease and other models used in the study is measured by classification performance metrics such as accuracy, precision, recall, F1-score. Accuracy is a measure of how often the classifier guesses correctly. Precision refers to the proportion of samples belonging to the positive class and assigned to the positive class. The recall indicates how many of the values that should have been positively predicted were positively predicted. The F1-score provides a single score that simultaneously balances both recall and precision concerns by a single number.

4. RESULTS

The deep learning algorithms which are VGG16, InceptionV3, ResNet50, Xception, DenseNet121, and EfficientNetB0, are used in this study. Before data augmentation techniques, the original dataset is tested for those algorithms. Table 1 shows the result of the original dataset performance.

Table 1. Original Dataset Performance Evaluation

	AUC	F1 (%)	Precision (%)	Recall (%)	Classification Accuracy (%)	Total Elapsed Time (second)
VGG16	1.0	99.2	99.3	99.2	99.250	319.782
InceptionV3	0.789	79.3	85	81.5	81.530	881.014
ResNet50	0.517	23.6	17.1	39.9	39.884	678.843
Xception	0.768	75.7	82.3	78.6	79.598	564.006
DenseNet121	0.950	94.4	95.4	94.5	94.512	1076.078
EfficientNetB0	0.843	83.9	88.7	85.3	85.305	714.353

As seen in Table 1, when we look at the Classification Accuracy percentage in deep learning algorithms performed on the original dataset, the best-performing algorithm is VGG16. Considering the total elapsed time, the VGG16 algorithm again obtained the best accuracy rates in the least time (Figure 7). When we look at the data in the same table, the worst-performing algorithm was ResNet50. In terms of both classification accuracy and other values, this algorithm cannot correctly classify cat-dog eye pictures taken with a mobile phone camera.

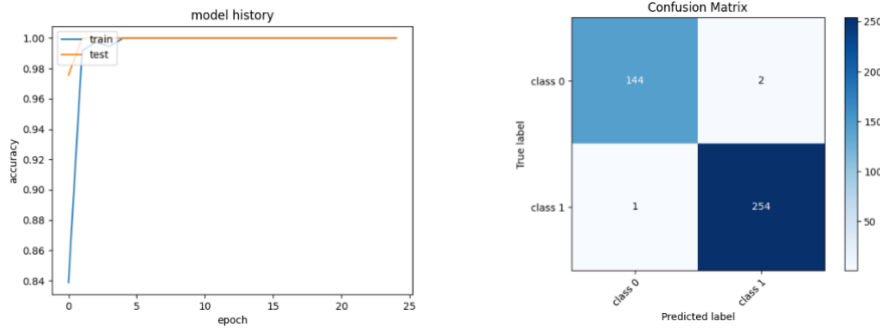


Figure 7. Model History and Confusion Matrix for VGG16 for Original Dataset

Table 2. After Augmented Dataset Performance Evaluation

	AUC	F1 (%)	Precision (%)	Recall (%)	Classification Accuracy (%)	Total Elapsed Time (second)
VGG16	1.0	99.9	99.9	99.9	99.9	747.194
InceptionV3	0.838	80.7	87.0	81.6	81.6	1414.395
ResNet50	0.510	33.5	25.3	50.0	50.0	1149.396
Xception	0.807	77.5	84.0	78.6	78.6	1030.830
DenseNet121	0.981	97.0	97.3	97.0	97.0	1670.396
EfficientNetB0	0.937	90.3	91.5	90.4	90.4	1163.967

When we look at Table 2, the performance values on the deep learning algorithms applied after the data augmentation processes show that the VGG16 algorithm has the highest value among all the performance criteria. But this value can be just as misleading. Compared to VGG16 architecture, DenseNet121 algorithm has the second-best classification accuracy compared to other algorithms because it is sensitive to over-fitting (Figure 8). But when the total elapsed time data is looked at, it unfortunately shows itself that it is one of the algorithms that process the most time. The ResNet50 algorithm also performed better after the data was replicated and the classification accuracy reached 50%.

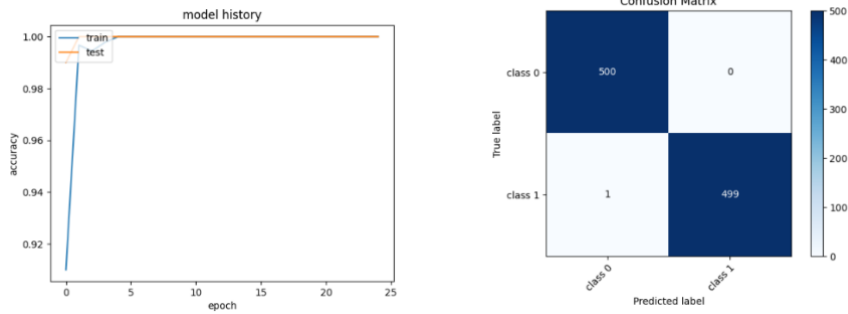


Figure 8. Model History and Confusion Matrix for VGG16 for Augmented Dataset

5. DISCUSSION

Data augmentation can be a powerful tool for improving machine learning models. By artificially increasing the size of the dataset, data augmentation can reduce the chance of the model memorizing the training data instead of learning from it. In addition, data augmentation can also help to reduce the variance of the model, as it enables the model to see more data and better generalize what it has learned. Furthermore, data augmentation can be used to increase the diversity of the dataset, thereby increasing the model's ability to learn robust features that are invariant to small variations in the data. Finally, data augmentation can help to reduce the amount of data preprocessing required, as the augmentation process can automatically create new data points with desirable properties. Data augmentation has been a useful tool for detecting eye diseases in the medical field. It has been used to improve the accuracy of computer-aided diagnosis systems, as well as to reduce the time and cost of manual data processing. By augmenting a dataset with additional data points, it is possible to increase the ability of the model to recognize patterns and be more accurate in its diagnoses.

Data augmentation can also help to reduce false positives, as increased data points can be used to provide more context and improve the accuracy of the results. Additionally, data augmentation can facilitate the training of models, reducing the need for large training datasets. Overall, data augmentation has been a beneficial tool for detecting eye diseases. It has the potential to reduce the cost of diagnosis and improve the accuracy of AI-based systems. It is important to note, however, that data augmentation should be used with caution, as it can also increase the risk of data bias. Therefore, it is important to ensure that any data augmentation techniques used are appropriate for the task at hand and do not introduce any bias into the system.

6. CONCLUSIONS

Special devices are used for the detection and diagnosis of eye diseases in academic studies. As the mobile phone camera features and image quality increase with the developing technology, it is now necessary to perform eye detection studies with mobile phone cameras as well. In this context, the images taken from cats and dogs with a mobile phone camera were divided into two as diseased and healthy. The original data set was first tested in deep learning algorithms, and then classification performance values were calculated over the same algorithms using data augmentation techniques. As can be seen in the performance result table, performance values increased after data augmentation.

Data augmentation can be a powerful tool for diagnosing and treating eye diseases. It enables doctors to analyze large amounts of data quickly and accurately, as well as to customize treatments for each individual patient. By leveraging the power of deep learning, data

augmentation can help doctors to identify patterns in the data that can lead to earlier diagnosis and personalized treatment plans. In the long run, data augmentation will help to improve patient outcomes and reduce the costs associated with eye diseases. Data augmentation can increase the accuracy of diagnosis by providing more data points to be analyzed, and can also reduce the time and cost required for diagnosis. Furthermore, it can also be used to reduce the variability in data and improve the generalizability of models. With its ability to generate more data points, data augmentation can help to increase the accuracy of diagnosis and lead to better treatment outcomes. In conclusion, data augmentation is an essential tool for the detection and diagnosis of eye diseases, and its use should be encouraged.

REFERENCES

- [1] Kirk N. Gelatt (2013), *Ocular Diseases of Companion Animals, Veterinary Ophthalmology*, 5th Edition
- [2] Shan, J., Li, L. (2016). A deep learning method for microaneurysm detection in fundus images, *IEEE First International Conference on Connected Health: Applications, Systems and Engineering Technologies (CHASE)*, Washington, DC, 357-358.
- [3] Deepa, V., Kumar, C. S., & Andrews, S. S. (2021). Fusing dualtree quaternion wavelet transform and local mesh-based features for grading of diabetic retinopathy using extreme learning machine classifier. *International Journal of Imaging Systems and Technology*, 31, 1625-1637
- [4] Güldemir, N.H., Alkan A., (2021), Derin Öğrenme ile Optik Koherens Tomografi Görüntülerinin Sınıflandırılması, *Fırat Üniversitesi Müh. Bil. Dergisi Araştırma Makalesi* 33(2), 607-615
- [5] Tasnim N, Hasan M, Islam I, (2019), Comparison study of Deep Learning approaches on Retinal OCT Image”, *arXiv preprint arXiv:1912.07783*
- [6] Szegedy, C., Liu, W., Jia, Y., Sermanet, P., Reed, S., Anguelov, D., Rabinovich, A., (2015), Going deeper with convolutions, *In Proceedings of the IEEE conference on computer vision and pattern recognition*, 1-9
- [7] Pandiyan, Vigneshwara & Tjahjowidodo, Tegoeh & Caesarendra, Wahyu and Murugan, Pushparaja. (2019). In-process virtual verification of weld seam removal in robotic abrasive belt grinding process using deep learning, *Robotics and Computer-Integrated Manufacturing*. 57. 477–487, 10.1016/j.rcim.2019.01.006
- [8] He, K.; Zhang, X.; Ren, S.; Sun, J. (2016), Deep residual learning for image recognition. *In Proceedings of the IEEE Conference on Computer Vision and Pattern Recognition*, Las Vegas, NV, USA, 27–30 June; pp. 770–778
- [9] Szegedy, C.; Vanhoucke, V.; Ioffe, S.; Shlens, J.; Wojna, Z. (2016), Rethinking the inception architecture for computer vision. *In Proceedings of the IEEE Conference on Computer Vision and Pattern Recognition*, Las Vegas, NV, USA, 27–30 June; pp. 2818–2826
- [10] N. Dong, L. Zhao, C.H. Wu, J.F. Chang, (2020), Inception v3 based cervical cell classification combined with artificially extracted features, *Applied Soft Computing*, Volume 93, <https://doi.org/10.1016/j.asoc.2020.106311>
- [11] Chollet, François, (2016) Xception: Deep Learning with Depthwise Separable Convolutions, *arXiv Preprint arXiv:1610.02357*
- [12] Gao Huang, Zhuang Liu, Kilian Q. Weinberger, Laurens van der Maaten, and Chen Change Loy, (2016), *Densely Connected Convolutional Networks*, *arXiv:1608.06993*
- [13] Marin, Ivana, Saša Mladenović, Sven Gotovac, and Goran Zaharija. (2021), Deep-Feature-Based Approach to Marine Debris Classification, *Applied Sciences* 11, no. 12: 5644. <https://doi.org/10.3390/app11125644>
- [14] Mingxing Tan, Quoc V. Le., (2019), EfficientNet: Rethinking Model Scaling for Convolutional Neural Networks, *In International Conference on Computer Vision (ICCV)*
- [15] Ahmed, T., Sabab, N.H.N., (2022), Classification and Understanding of Cloud Structures via Satellite Images with EfficientUNet. *SN COMPUT. SCI.* 3, 99 <https://doi.org/10.1007/s42979-021-00981-2>



Research Article

Designing a Solar PV–Battery based on Electric Vehicle Charging Station

Authors: Samatar ABDI YONIS , Ziyodulla YUSUPOV , Muhammet Tahir GÜNEŞER 

To cite to this article: Abdi Yonis, S. , Yusupov, Z. & Guneser, M. T. (2023). Designing a Solar PV-Battery based on Electric Vehicle Charging Station . International Journal of Engineering and Innovative Research , 5(2) ,p123-136 . DOI: 10.47933/ijeir.1231500

DOI: 10.47933/ijeir.1231500

To link to this article: <https://dergipark.org.tr/tr/pub/ijeir/archive>



International Journal of Engineering and Innovative Research

<http://dergipark.gov.tr/ijeir>

Designing a Solar PV–Battery based on Electric Vehicle Charging Station

Samatar ABDI YONIS^{1*}, Ziyodulla YUSUPOV¹, Muhammet Tahir GÜNEŞER¹

¹Karabük University, Institute of Graduate Programs, Department of Electrical and Electronics Engineering, Karabük, Turkey.

*Corresponding Author: saamabdi4f@gmail.com

(Received: 09.01.2023; Accepted: 24.03.2023)

<https://doi.org/10.47933/ijeir.1231500>

ABSTRACT: Increasing transport demand necessitates higher oil consumption, resulting in an increase in carbon dioxide (CO₂) emissions, which is a major cause of air pollution. The use of electric vehicles (EVs) is becoming more common around the world. Recent advancements in lithium-ion battery technology have increased the improvement of EVs. In this work, a solar photovoltaic (PV) battery-based EV charging station is designed. Meanwhile, the overall system comprises a battery energy storage system (BESS), solar PV module, grid and EV charging station. Thus, the primary source for the charging station is the PV source but due to less power during the night, we included battery storage as a backup. Grid source is also recommendable for an uninterruptable power supply. An artificial neural network strategy is developed in MATLAB/Simulink for proper power management of the solar PV-battery based EV charging station connected to the AC grid. Moreover, by employing an adaptive neuro-fuzzy inference system (ANFIS) and PI controller-based MPPT, the grid voltage and current, real/reactive grid power and the maximum output power are obtained. The overall system is evaluated under different scenarios of irradiance level and temperature with a state of charge (SOC) greater than 10 % for simulation purposes. The result shows that during the night hour due to less power from the PV source, an artificial neural network begins to regulate the grid power so that it supplies power to the stationary storage and EV battery.

Keywords: Solar PV, Electric vehicle, Stationary storage, ANFIS MPPT, PI controller, Neural network.

1. INTRODUCTION

Nowadays, EVs are gradually replacing typical IC engines [1, 2]. For instance, IC engines have several disadvantages, for example, high greenhouse gas (GHG) emissions that can be resolved by EVs. As mentioned in Ref [3], EVs promise more environmentally friendly, noise-free operation, greater energy efficiency and require less maintenance than IC engines. Additionally, renewable energy sources (RES) should be employed in EVs to provide electrical power to meet growing future needs. Amongst the different RES available such as; the solar PV system, fuel cell-based generation, hydropower and wind energy, solar PV generation is the most useful option for EV charging since it's available nearly everywhere regardless of whether the location is urban or rural [4-6].

Most of the research papers focus on issues like; (1) grid-connected solar PV based EV charging stations. (2) fast charging stations and control approaches for solar PV with AC grid. (3) an off-grid solar PV based EV charging stations, etc. Ref [7] demonstrated an effective design and power management approach of a PV-battery based EV charging station connected to an AC grid using MATLAB software. Ref [8] focuses on issues like; (1) energy management approach of converter control multi-port EV battery charging from solar PV source. (2) maintaining the dc bus voltage constant during overload in the grid power. (3) reducing the charging time. Ref

[9] demonstrates the design features and application of a modern PV-based level-2 EV charging station regulated by a type-1 vehicle connector using MATLAB and PROTEUS software. In Ref [10], the authors present a charging station strategy for fast DC charging using MATLAB software. Moreover, a DC bus is developed by connecting to the power grid through converter. Then the converter was developed to such a degree that the power factor was close to unity and the line current harmonics are maintained to a minimum. Ref [11] proposed, designed and presented an off-grid charging station for EV and hydrogen vehicles (HV) using GAMS and MATLAB software. In addition, both EV and HV are charged simultaneously. Ref [12] investigates an ideal PV-based EV charging station design from a technical and economical perspective under various irradiance using HOMER software. Ref [13] proposed an ideal charging and discharging management technique of V2G, G2V and BESS for EV charging station using a demand response (DR) program. It suggested that it's possible to reduce the challenges of an optimization problem by using a distributed computing system.

In this study, a solar PV-battery based EV charging stations connected to an AC grid has been designed. The characteristics of the implemented system, which employs ANFIS+PI controller-based MPPT, are specified in Table. 1. In addition, the entire model was simulated with different scenarios of irradiance level and temperature. At maximum irradiance, the PV power provides power to the stationary storage and EV battery. Then, the stationary storage discharges to fulfill EV demand when the PV power is low, especially during the night. Moreover, a neural network was developed in MATLAB for grid control purposes and to guarantee an uninterrupted power supply. Eventually, this paper is structured in such a way. Section 2 presents the system design. The control strategy is discussed in section 3. The simulation result is investigated in section 4. Conclusion remarks are stated in section 5.

2. SYSTEM DESIGN

This work presents a solar PV- battery to charge EVs that employs a boost converter using ANFIS and PI controller. The PV-battery is designed in a system with a 40 Ah lithium-ion battery rated capacity and 300 V open circuit voltage (V_{oc}). Figure 1 represents the overall block diagram of a PV-battery based EV charging station. Hence, the block diagram comprises; (1) a PV module along with the DC-DC converter and MPPT algorithm. (2) stationary storage (BESS) with a bi-directional DC-DC converter and voltage controller. (3) grid supply and (4) EV battery with DC-DC converter.

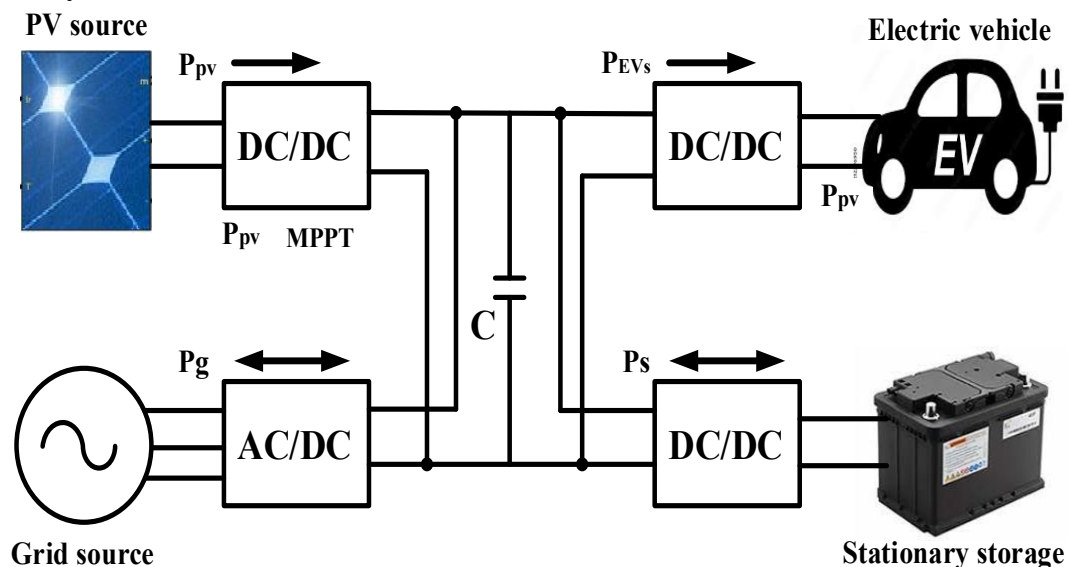


Figure 1. Block diagram of PV-battery based EV charging station.

Thus, the primary source for the charging station is the PV source. Therefore, the power available in the PV goes to charge the stationary storage element and EV battery. If power generation is unavailable in the PV source, the stationary storage provides power to the EV battery. Besides, a grid source is also recommendable for an uninterruptable power supply.

2.1. Photovoltaic Module

Solar systems use PV panels to concentrate solar radiation to generate sunlight into electricity [14]. In this work, the PV system is directly linked to a load (EVs) or stationary battery via DC-DC converter. Hence, the system’s operational point is crossing between the I-V curve of the PV and the load line. Normally, these operational points are not at the maximum power of the PV system. Therefore, a neural network-based ANFIS MPPT and PI controller are applied to achieve the maximum power available from the PV array. The generalized circuit diagram of the PV system is represented in Figure 2 and the output current can be given as [15].

$$I_A = N_p I_{ph} - N_p I_s \left\{ \exp \left[\frac{q \left(\frac{V}{N_s} + I \frac{R_s}{N_p} \right)}{nKT} \right] - 1 \right\} - \left[\frac{V \left(\frac{N_p}{N_s} \right) + I R_s}{R_{sh}} \right] \tag{1}$$

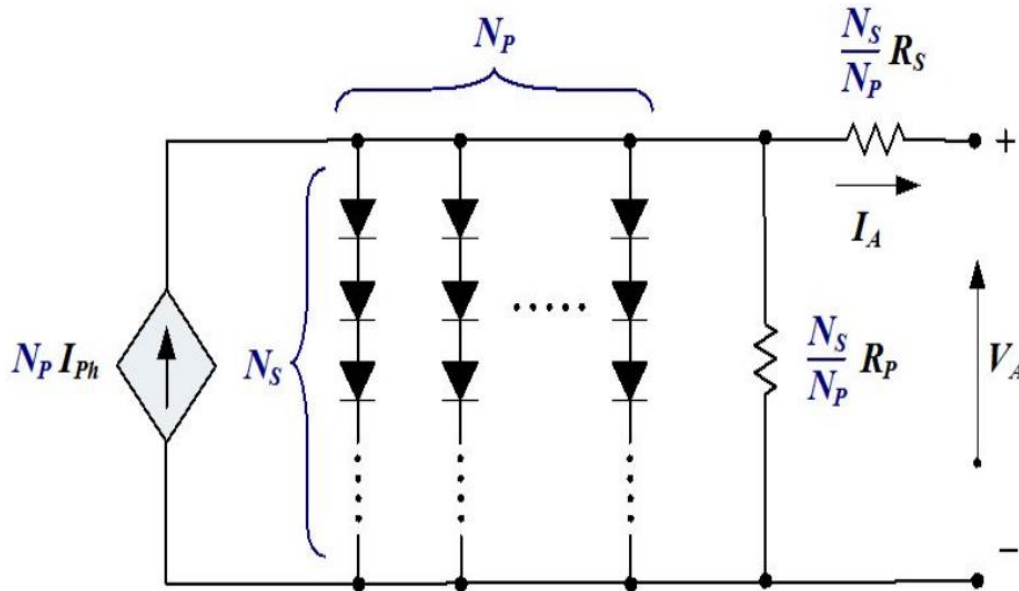


Figure 2. Generalized circuit diagram of the PV array [15].

where N_s and N_p are the number of cells connected in series and parallel. I_A and V are the PV module output current (A) and voltage (V). I_{ph} is the photon current. I_s is the saturation current equal to 3.2328×10^{-10} A. K is Boltzmann’s constant. n is the ideality factor equal to 1.045. q is the number of charges of electrons equal to 1.602×10^{-19} C. R_s and R_{sh} are series and shunt resistance equal to 0.22828 and 47.9694 ohms respectively [16].

Figure 3 represents the I-V and P-V curve of the PV system and maximum output power (P_m) can be given as [17]:

$$P_m = V_m I_m \tag{2}$$

where, V_m is the maximum voltage and I_m is the maximum current.

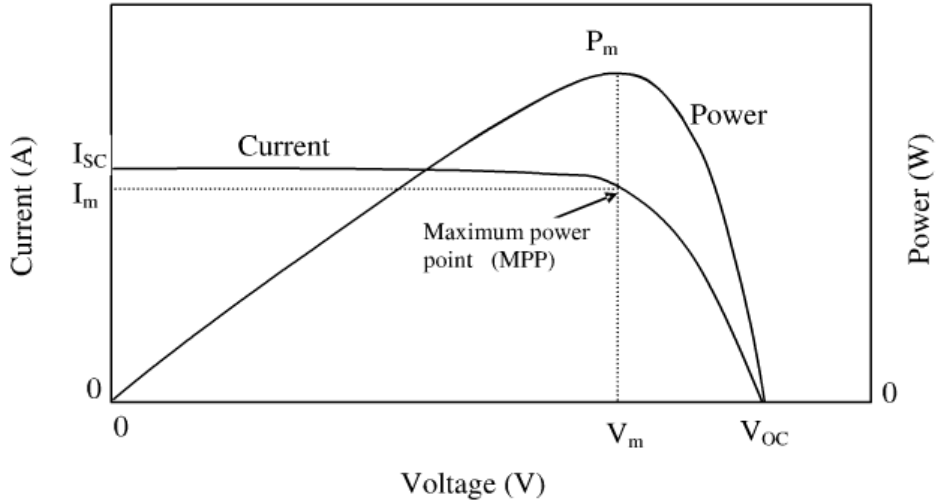


Figure 3. I-V and P-V curve of the PV array [17].

2.2. Stationary Storage with Bidirectional DC-DC Boost Converter

Normally, bidirectional DC-DC converters allow energy storage for the battery [18]. There are two types of bidirectional converters: isolated and non-isolated type [19]. In this work, the power from the PV is stored in stationary storage, which charges the EV battery during the night. Moreover, a 240 V, 40 Ah, li-ion battery is selected for the stationary battery. Equivalent circuit diagram of DC-DC boost converter is represented in Figure 4.

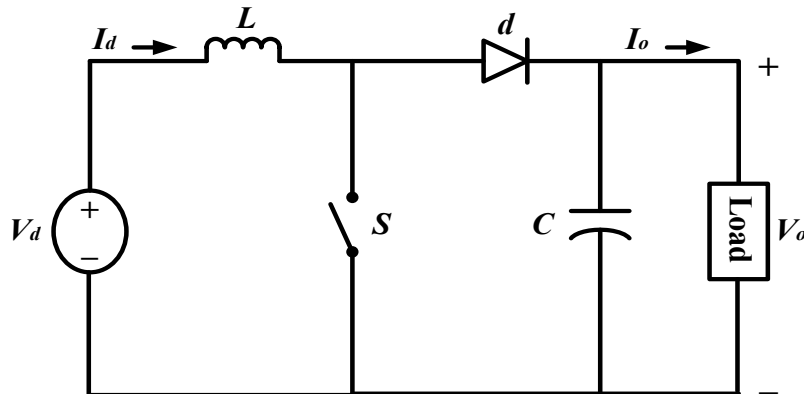


Figure 4. Equivalent circuit diagram of the DC-DC boost converter.

Here, the design of ripple current, inductor and capacitor can be represented as follows:

$$D = 1 - \frac{\eta V_i}{V_o} \tag{3}$$

where D is the duty ratio, η is the efficiency, V_i and V_o are the input and output voltage. Here, ripples current equation will be formulated as:

$$\Delta I_L = \frac{D V_i}{L f_s} \tag{4}$$

where f_s is the switching frequency and Inductor (L) is designed as follows:

$$L = \frac{V_i(V_o - V_i)}{\Delta I_L f_s V_o} \tag{5}$$

The capacitor equation can be obtained as:

$$C = \frac{DI_o}{\Delta V_o f_s} \tag{6}$$

where I_o is the output current of the system.

2.3. EV Battery

Batteries are a source of electric power that is used to store electrical energy. Here, the EV battery is considered as a load. Among the different types of rechargeable batteries, lithium-ion batteries are considered in this study. Therefore, a 240 V, 40 Ah, li-ion battery with SOC greater than 10 % is chosen for the EV battery. Hence, the energy in the battery is represented as WH and it's given as follows:

$$WH = V \times AH \tag{7}$$

with EV battery calculated as:

$$EV_{bat} = \frac{V \times SOC \times AH}{100} \tag{8}$$

Where V is the nominal voltage, SOC is the initial state of charge and AH (ampere-hour) is the battery's rated capacity.

3. CONTROL STRATEGY

This paper uses an artificial neural network concept for grid control. Moreover, the study uses ANFIS MPPT and PI controllers, to achieve the maximum output power from the PV source.

3.1. Neural Network Strategy

Neural network (NN) is a type of data processing system composed of several basic and interconnected nodes known as neurons, which are similar to human brain cells [20, 21]. The hidden neurons are trained by applying the Levenberg-Marquardt algorithm.

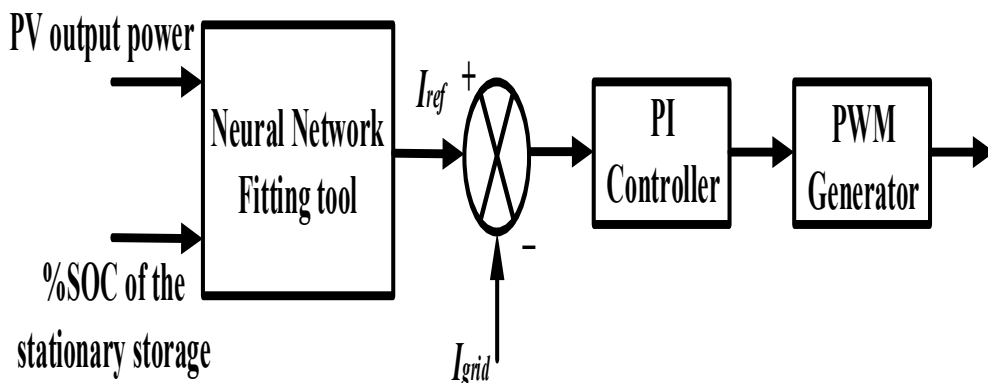


Figure 5. Neural network current controlled structure.

As mentioned earlier, this study uses neural network to control the grid or inverter current flow. Hence, PV output power and SOC of the stationary storage are two input variables of the neural network and an output of reference current. In addition, the reference and inverter currents are

compared to be processed by the PI-controller, to produce pulse width modulation (PWM) for the inverter. Figure 5 represents neural network current controlled block.

3.2. ANFIS and PI Controller-based MPPT

This system (ANFIS) is designed to simulate the characteristics of neural–fuzzy inference systems (FIS). In addition, an adaptive neural network lacks synaptic weights, however, it contains both adaptive and non-adaptive nodes. Its name "adaptive network", comes from the fact that it is easily converted into a neural network structure with a typical feedforward topology [22]. Figure 6 indicates five layered ANFIS structures.

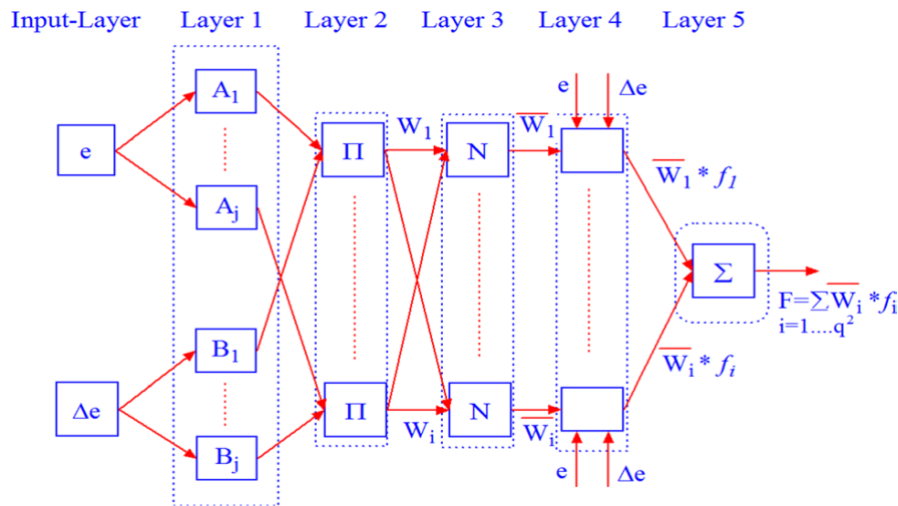


Figure 6. Structure of five-layer ANFIS model.

Layer 1: The parameters of the adaptive node (*i*) in layer 1 are called non-linear variables of the ANFIS network. The equation of each node can be given as follows:

$$\begin{cases} L_{1,i} = \mu A_i(e) \\ L_{1,i} = \mu B_i(\Delta e) \end{cases} \text{ for } i = 1, 2 \dots j \tag{9}$$

where A_i and B_i are membership functions (MF) of each node. e and Δe are inputs. Typically, the Gaussian MF is applied to each node to disperse the input elements. Here, the function of the Gaussian MF can be represented as follows:

$$f(x; \sigma, c) = e^{-\frac{(x-c)^2}{2\sigma^2}} \tag{10}$$

where σ and c are width and center of Gaussian MF. Further, σ and c are non-linear variables and can be adjusted during the learning process.

Layer 2: The fixed node (Π) is obtained from the outcome of layer 1 node signal and it's equation can be formulated as follows:

$$L_{2,i} = W_i = \mu A_i(e) \mu B_i(\Delta e) \text{ for } i = 1, 2 \dots j^2 \tag{11}$$

Here, the outcome of each node of layer 2 corresponds to the firing power of a rule basis.

Layer 3: The output of fixed node (N) is solved by dividing the value of each node by the total value of all nodes which is represented as follows:

$$L_{3,i} = \bar{W}_i = \frac{W_i}{\sum_{i=1}^{j^2} W_i} \quad (12)$$

Layer 4: the function of adaptive node can be given by:

$$L_{4,i} = \bar{W}_i f_i = \bar{W}_i (p_i e + q_i \Delta e + r_i) \quad (13)$$

where \bar{W}_i is the measured firing strength from layer 3. p_i, q_i, r_i are the subsequent variables of ANFIS network, which is modified using least-square technique.

Table 1. System Parameters.

Characteristics	Value
Module name	1Soltech 1STH-350-WH
Array data	Parallel strings, 1; series connected cells, 6
Open circuit voltage (V_{oc})	51.5 V
Voltage at maximum power point (V_{mpp})	43 V
Short circuit current (I_{sc})	9.4 A
Current at maximum power point	8.13 A
Maximum power (P_m)	350 W
Stationary storage	Lithium-ion, 240 V, 40 Ah
EV battery	Lithium-ion, 240 V, 10 Ah
Capacitances (C1, C2, C3, C4)	4.07 μ F, 8.98 μ , 100 μ F, 6.01 μ F
Inductances (L1, L2, L3, L4)	0.0153 H, 0.0069 H, 0.0072 H, 0.0012 H

Layer 5: The output of this node (Σ) is determined by using weighted average method and is formulated as:

$$L_{5,i} = \sum_{i=1}^{j^2} \bar{W}_i f_i = \frac{\sum_{i=1}^{j^2} W_i f_i}{\sum_{i=1}^{j^2} W_i} \quad (14)$$

In this study, to achieve the maximum output power, ANFIS+PI controller-based MPPT is used. In addition, a five-layer is used to reach maximum power point (MPP), as shown in Figure 7. Temperature (T) and irradiance (G) are two input parameters of the ANFIS+PI controller and single output voltage. Figure 8 shows the developed ANFIS structure. The ANFIS input MF for both irradiance and temperature are given in Figure 9 and Figure 10, respectively.

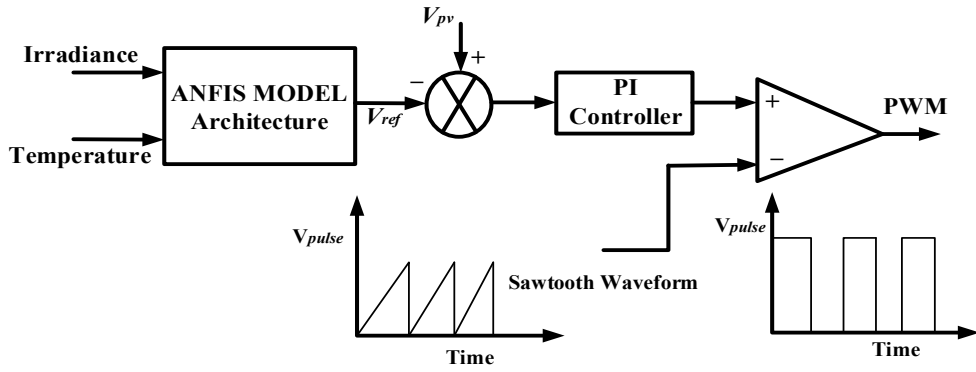


Figure 7. Block diagram of ANFIS and PI controller-based MPPT.

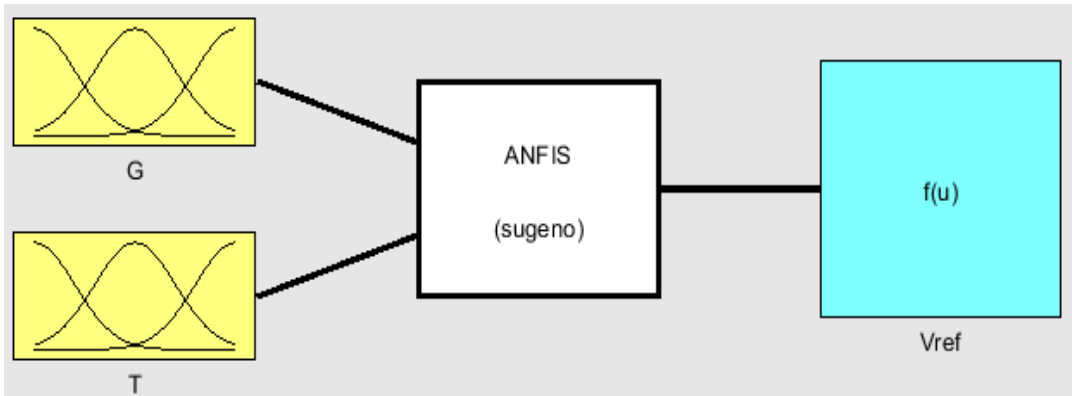


Figure 8. Developed ANFIS system.

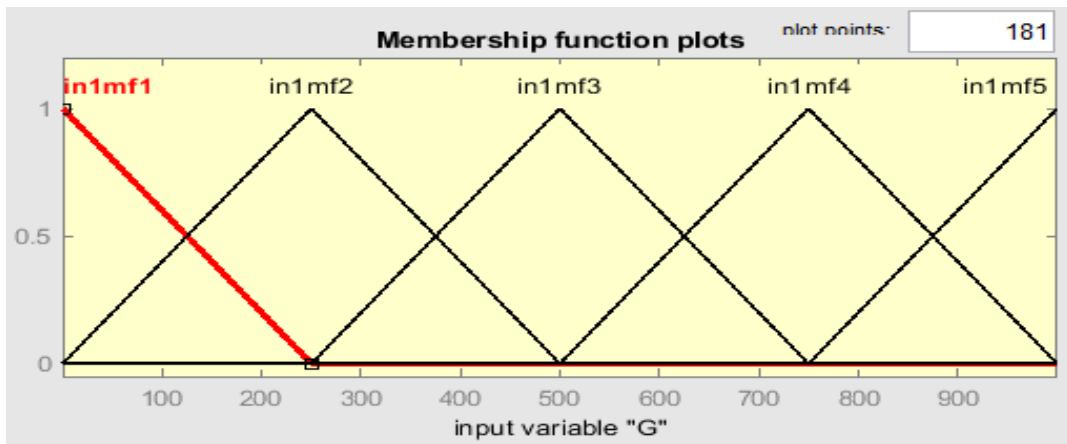


Figure 9. ANFIS input MF for irradiance.

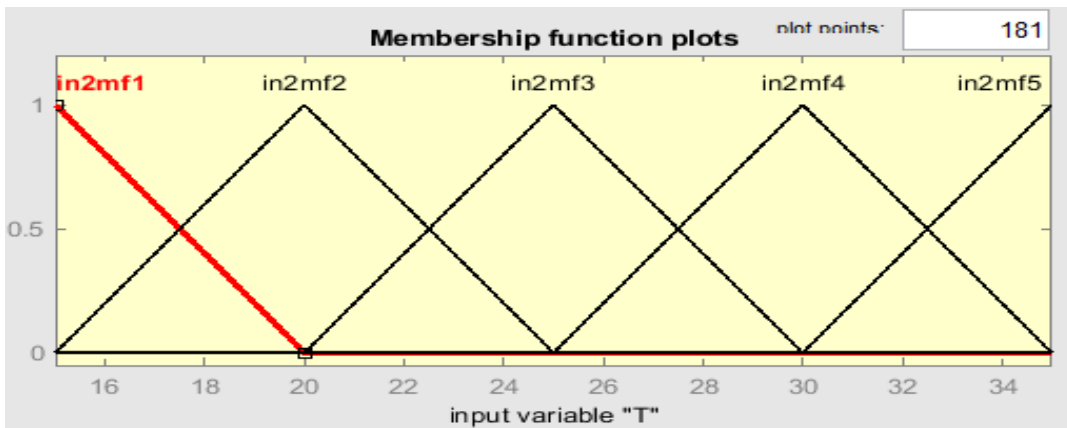


Figure 10. ANFIS input MF for temperature.

4. RESULT AND DISCUSSION

In this paper, a standalone PV system integrated with DC-DC boost converter based on a neural network concept is executed in MATLAB. Additionally, the characteristics of the implemented system, which employs ANFIS+PI controller-based MPPT, are shown in Table 1.

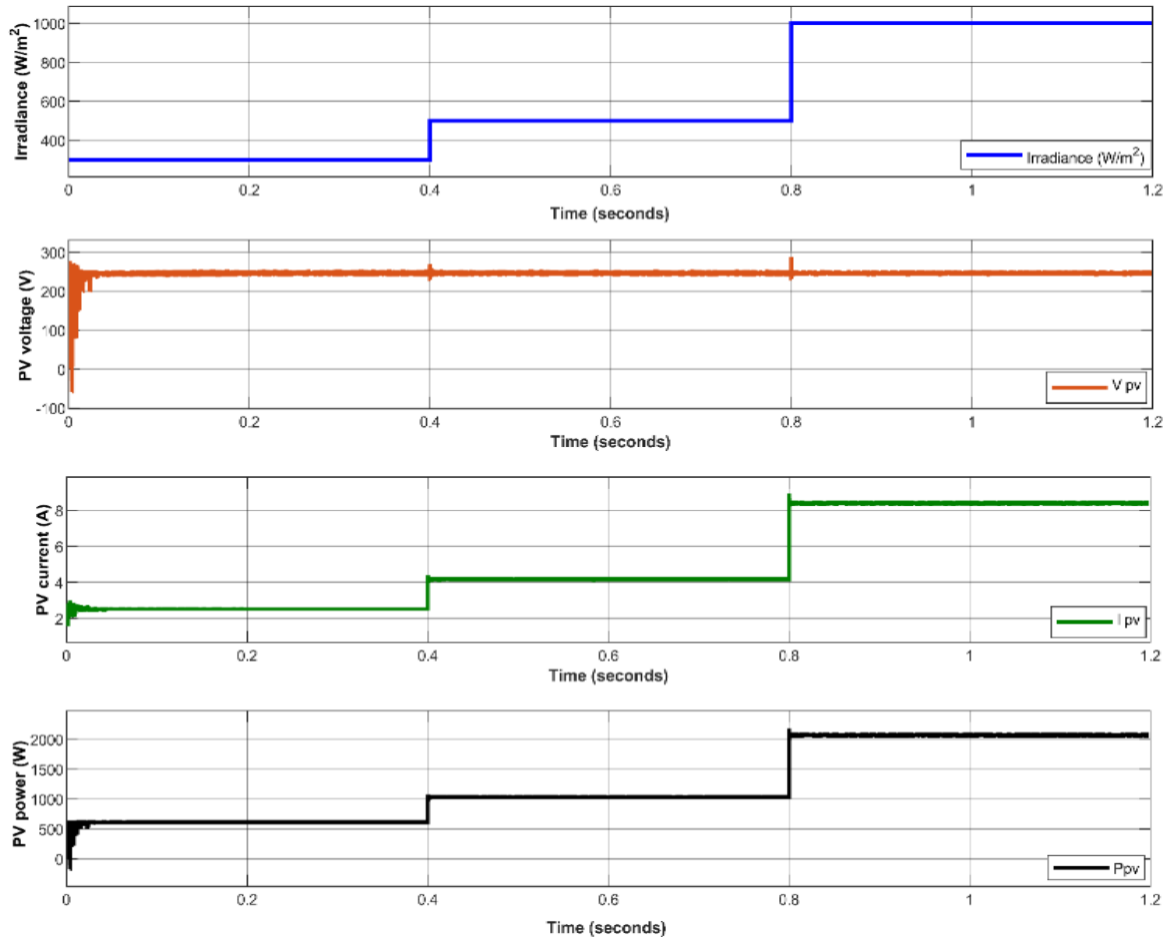


Figure 11. PV voltage, current and power with varying irradiance.

This study simulated the voltage and current of both EV battery and stationary storage, Dc bus voltage, real/reactive grid power and the maximum output power. The overall system has been evaluated under different scenarios of irradiance and temperature. Figure 11 represents the result of PV voltage, current and power with variable irradiance. ANFIS model is first created in MATLAB. The model builds a single output Sugeno-FIS and modifies the system specifications using the input-output training data set. In addition, the ANFIS element is instantly generated using grid partitioning. Afterward, the ANFIS element is trained with 121 Epochs by applying hybrid learning technique. Finally, the ANFIS object is tested with the trained data. The simulation results of the entire system are evaluated under different scenarios such as under standard test condition (STC), under varying irradiance level and charging and discharging modes of EV battery and stationary storage.

First, the simulation starts with constant temperature and varying irradiance. At 1000 W/m² irradiance, the PV power improves to 2.1 kW. Further, as the irradiation modifies, the PV power and current also change to a new operating point with constant PV voltage, which allows the PV system to achieve the maximum output power. Moreover, with varying irradiance level and temperature, the PV power also modifies as shown in Figure 12.

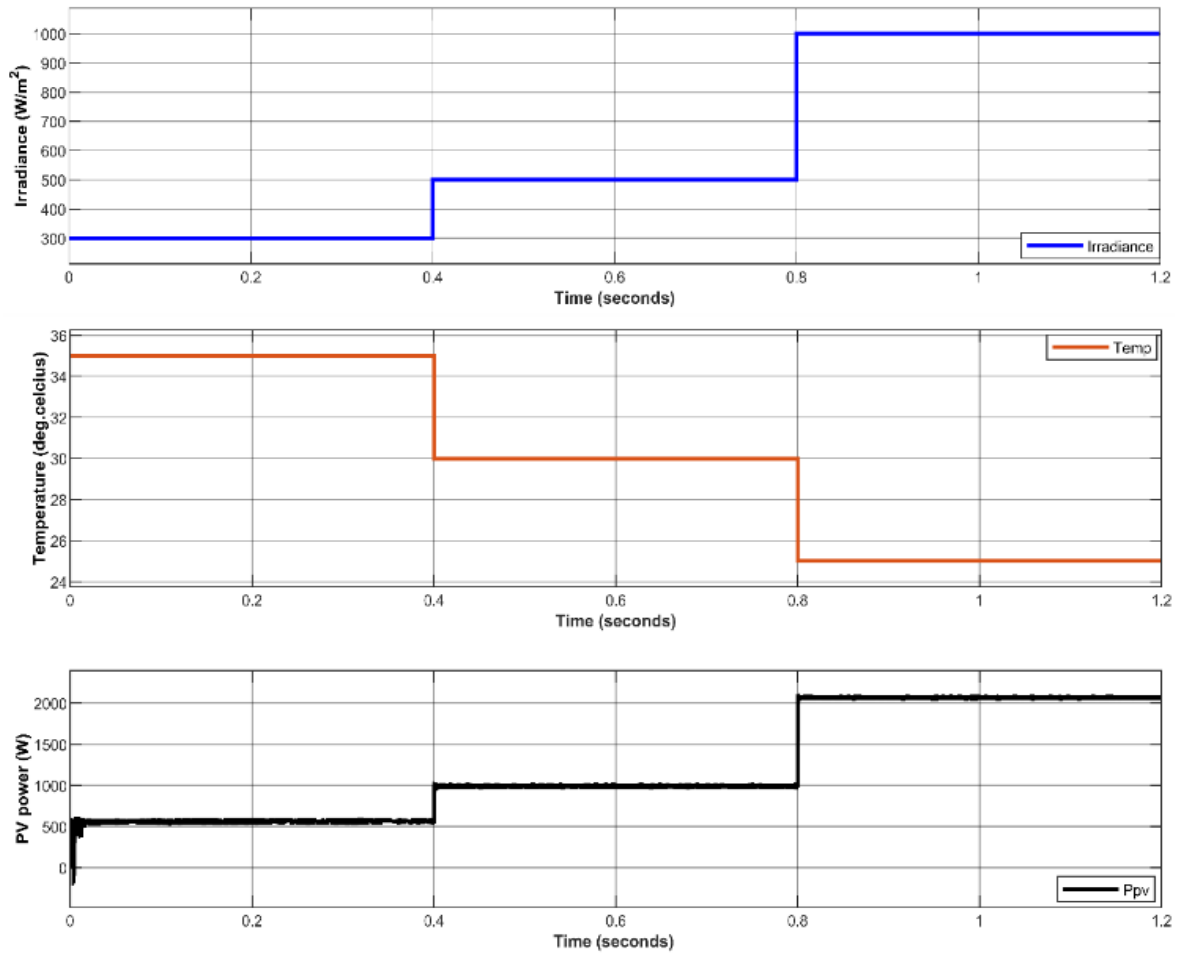


Figure 12. PV power with variable irradiance and temperature.

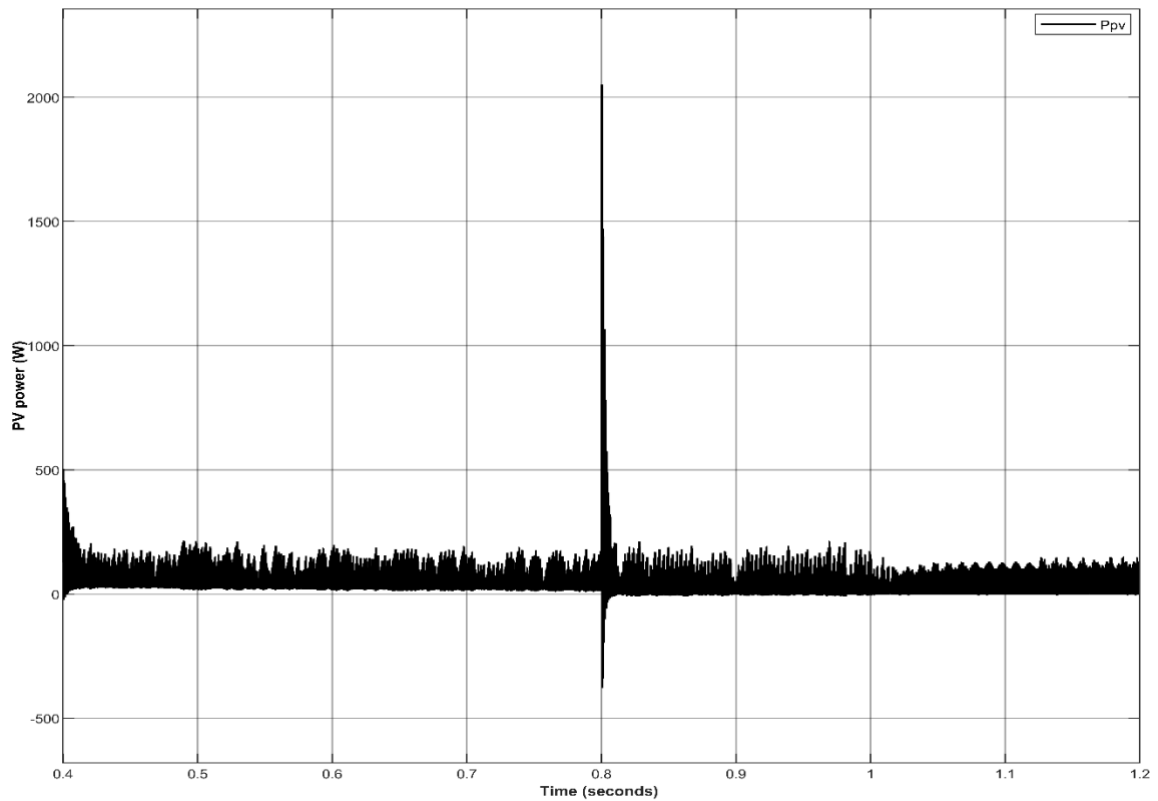


Figure 13. PV power during the night.

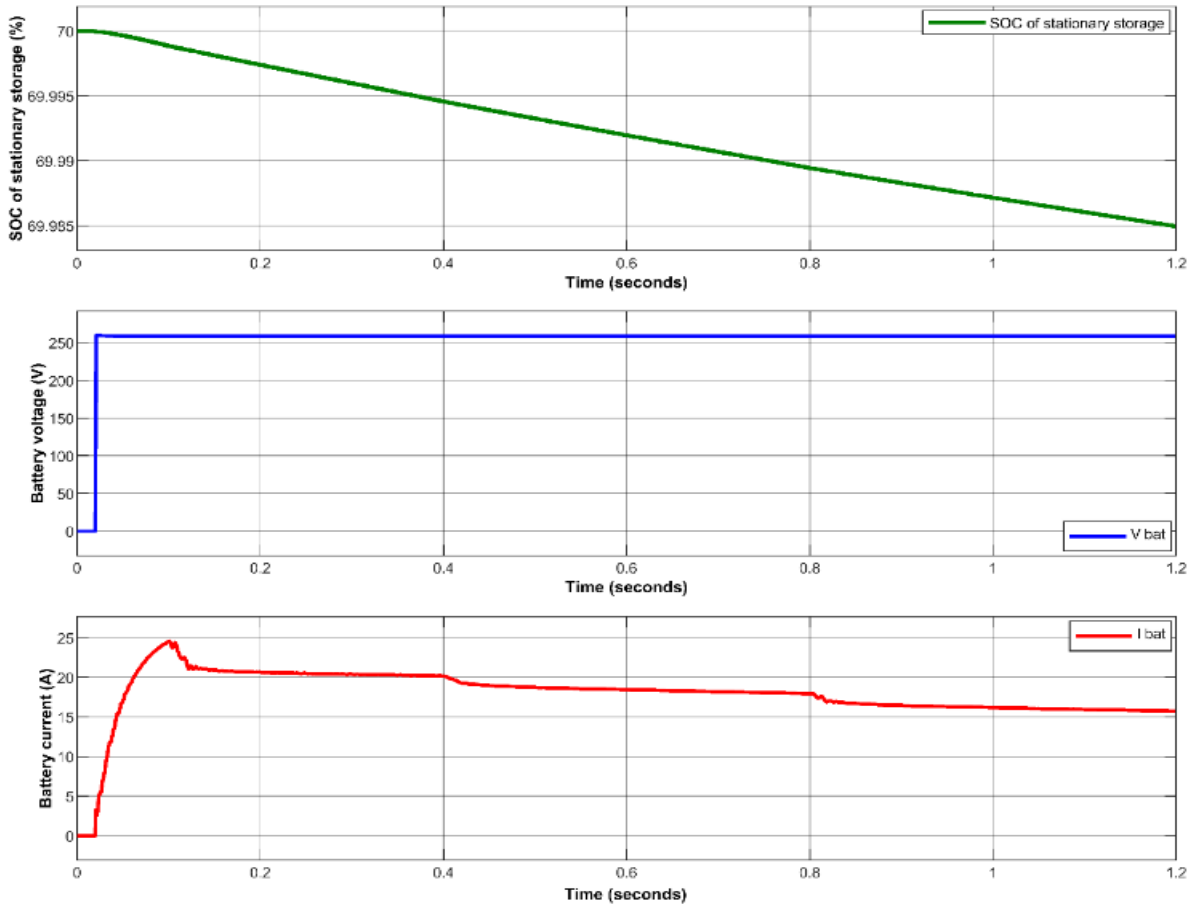


Figure 8. SOC, voltage and current of the stationary storage.

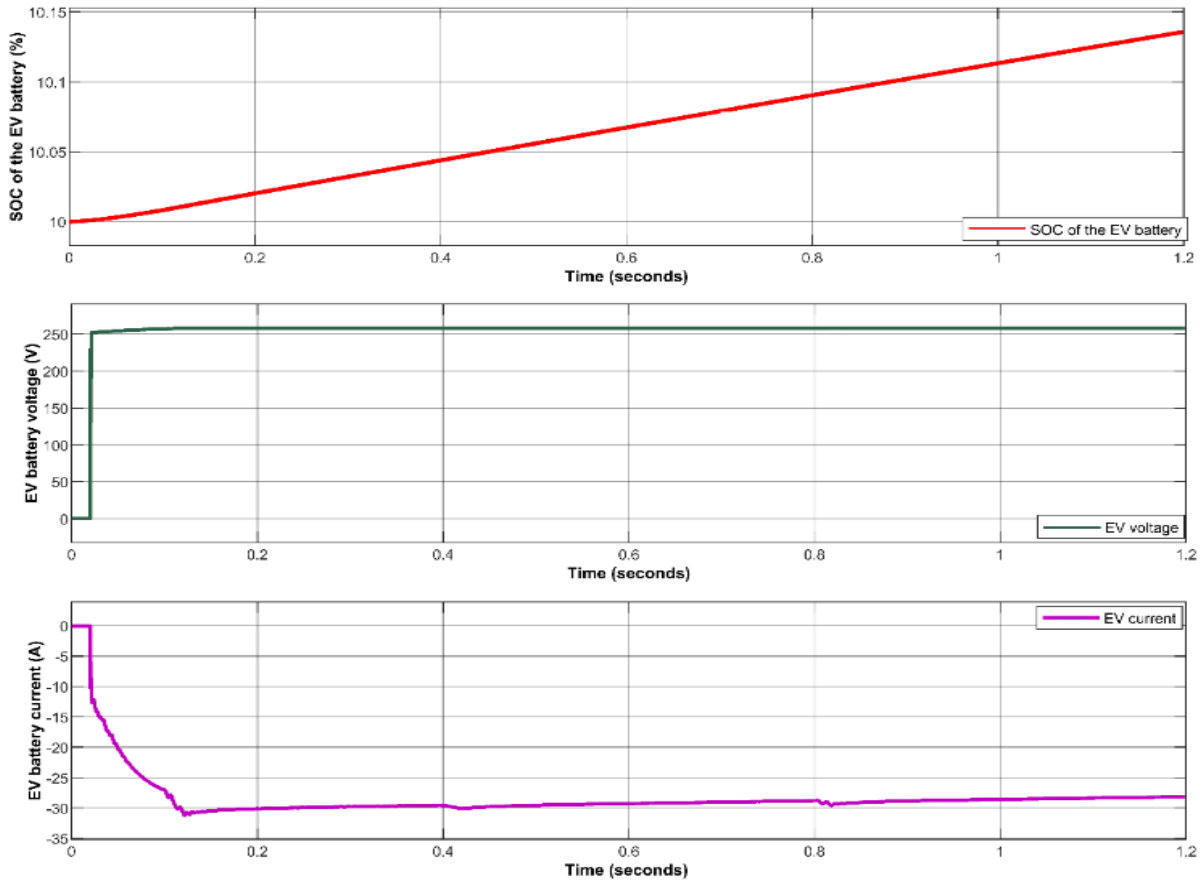


Figure 9. SOC, current and voltage of the EV battery.

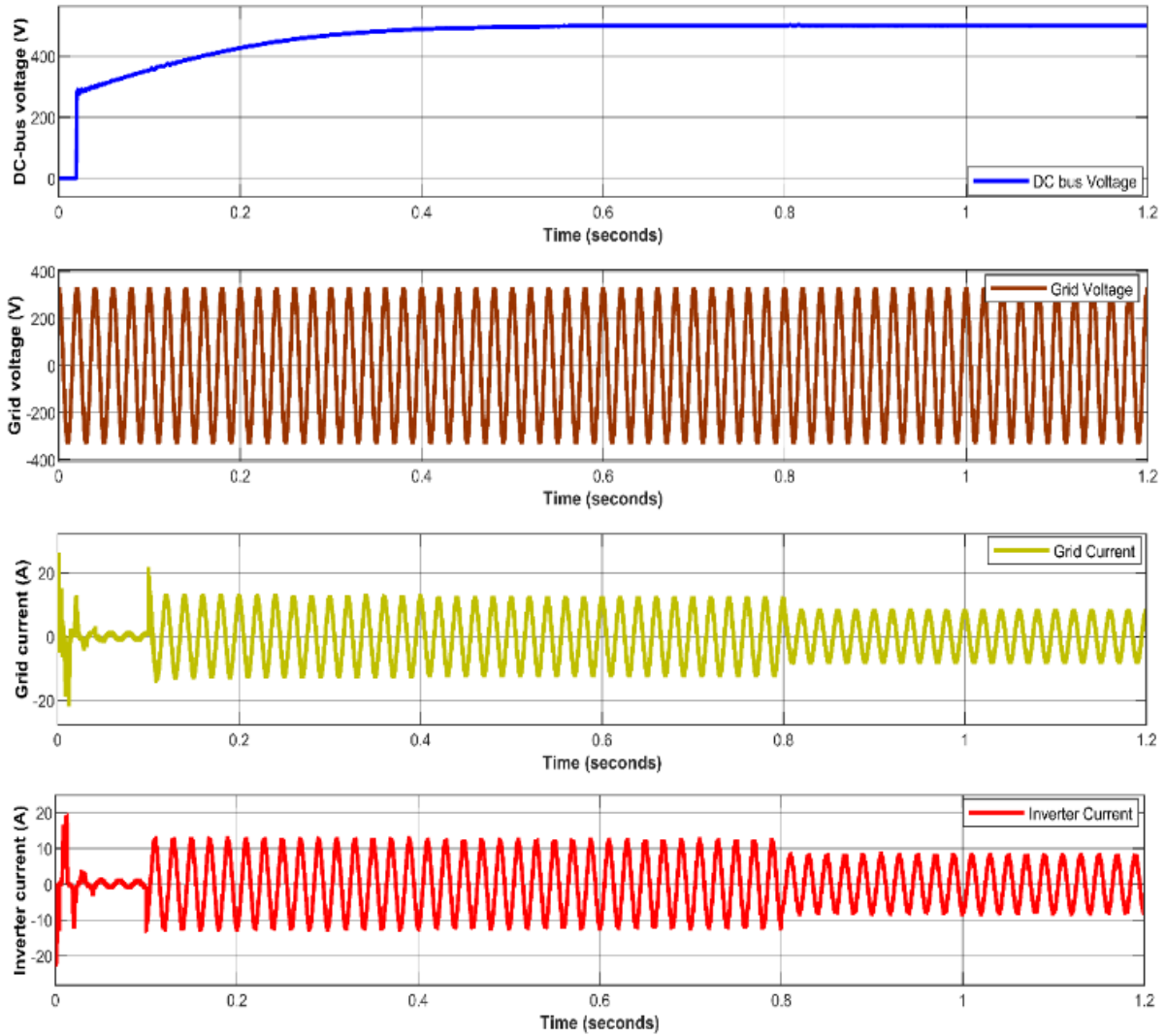


Figure 10. Performances of the dc bus voltage, grid voltage and current.

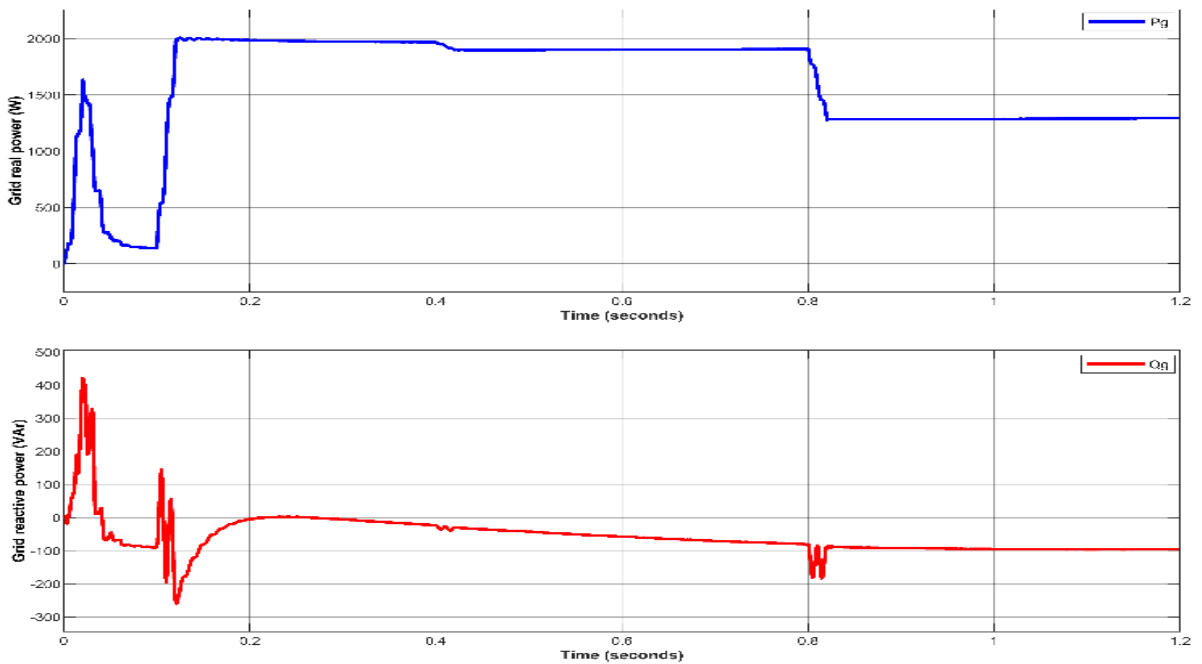


Figure 11. Performances of real and reactive grid powers.

In addition, Figure 14 represents the SOC of the stationary storage, its voltage and current. Since the SOC of the stationary storage decreases from 70 %, thus, the battery current operates in discharging mode. On the other hand, the SOC of the EV battery is increasing from 10 % as considered, accordingly, the EV battery current is around -30 A, which shows that it's in charging mode as indicated in Figure 15. A capacitor element attaches between the solar PV–EV battery and stationary storage as given in Figure 1. Additionally, the purpose of the capacitor is to keep the dc-bus voltage constant and it's maintaining 500 V as illustrated in Figure 16. Further, the grid voltage, current and inverter are working properly. Figure 17 represents the performances of real and reactive grid powers.

In this work, the grid voltage and current, real/reactive grid power and maximum output power were mainly discussed. In the literature, the design features and application of a modern PV-based level-2 EV charging station regulated by a type-1 vehicle connector was developed [9]. A charging station strategy for fast DC charging has been presented in [10]. Moreover, a dc-bus was developed by connecting to the power grid through converter. Then the converter was developed to such a degree that the power factor was close to unity and the line current harmonics were maintained to a minimum. In Ref [11], an off-grid charging station for EV and HV has been proposed. In addition, both EV and HV are charged simultaneously. Ref [12] investigates an ideal PV-based EV charging station design from a technical and economical perspective under various irradiance level. However, most of this literatures focused on the limitation of charging stations architectures and its dependency on the electrical grid. When compared the above literatures with this study, a novel ANFIS+PI controller was developed, to achieve the maximum output power from the PV system. Furthermore, a five-layered ANFIS model was used to reach at MPP. Then the PV power provides power to the EV battery and stationary storage. During night-hour, the power from the PV source is less (see Figure 13), as a result, a NN begins to regulate the grid power. Afterward, the grid power supplies power to the stationary storage and EV battery.

5. CONCLUSION

In this work, a novel ANFIS+PI controller-based MPPT strategy for solar PV-battery based on EV charging stations connected to an AC grid was designed. The entire system has been simulated under different scenarios of irradiance level and temperature. Thereafter, an appropriate controller (NN concept and ANFIS-PI controller) was chosen and integrated into the system. During the day, the PV power goes to charge the stationary storage and EV battery. Similarly, stationary storage discharges to fulfill EV demand when the PV power is low, especially during the night. Moreover, during this time, a NN concept starts to regulate the grid power, to supply power to the stationary storage.

The simulation results will be compared with the experimental results in the future work, to enhance the reliability of the system.

Conflict of Interest

No conflict of interest was declared by the authors.

REFERENCES

- [1] Khalid, M. R., Alam, M. S., Sarwar, A., Asghar, M. S. J. (2019). A Comprehensive review on electric vehicles charging infrastructures and their impacts on power-quality of the utility grid. *eTransportation*, 1, 100006.

- [2] Sun, X., Li, Z., Wang, X., Li, C. (2019). Technology development of electric vehicles: A review. *Energies*, 13, 1, 1–29.
- [3] Khan, S., Ahmad, A., Ahmad, F., Shafaati Shemami, M., Saad Alam, M., Khateeb, S. (2018). A Comprehensive Review on Solar Powered Electric Vehicle Charging System. *Smart Sci.*, 6, 1, 54–79.
- [4] Ismael, S. M., Abdel Aleem, S. H., Abdelaziz, A. Y., Zobaa, A. F. (2019). Probabilistic hosting capacity enhancement in non-sinusoidal power distribution systems using a hybrid PSO-GSA optimization algorithm. *Energies*, 12, 6, 1018.
- [5] Omar, A. I., Sharaf, A. M., Abdel, A. S. H., Mohamed, A. A., El-Zahab Essam, EA. 2019. Optimal Switched Compensator for Vehicle-To-Grid Battery Chargers Using Salp Optimization. *21st International Middle East Power Systems Conference (MEPCON)*, 139-144.
- [6] Singh, B., Verma, A., Chandra, A., Al-Haddad, K. (2020). Implementation of solar PV-battery and diesel generator based electric vehicle charging station. *IEEE Transactions on Industry Applications*, 56, 4, 4007-4016.
- [7] Biya, T. S., Sindhu, M. R. (2019). Design and power management of solar powered electric vehicle charging station with energy storage system. *3rd International conference on Electronics, Communication and Aerospace Technology (ICECA)*, 815-820.
- [8] Savio, D. A., Juliet, V. A., Chokkalingam, B., Padmanaban, S., Holm-Nielsen, J. B., Blaabjerg, F. (2019). Photovoltaic integrated hybrid microgrid structured electric vehicle charging station and its energy management approach. *Energies*, 12, 1, 168.
- [9] Shariff, S. M., Alam, M. S., Ahmad, F., Rafat, Y., Asghar, M. S. J., Khan, S. (2019). System design and realization of a solar-powered electric vehicle charging station. *IEEE Systems Journal*, 14, 2, 2748-2758.
- [10] Khan, W., Ahmad, F., Alam, M. S. (2019). Fast EV charging station integration with grid ensuring optimal and quality power exchange. *Engineering Science and Technology, an International Journal*, 22, 1, 143-152.
- [11] Mehrjerdi, H. (2019). Off-grid solar powered charging station for electric and hydrogen vehicles including fuel cell and hydrogen storage. *International journal of hydrogen Energy*, 44, 23, 11574-11583.
- [12] Minh, P. V., Le Quang, S., Pham, M. H. (2021). Technical economic analysis of photovoltaic-powered electric vehicle charging stations under different solar irradiation conditions in Vietnam. *Sustainability*, 13, 6, 3528.
- [13] Liao, J. T., Huang, H. W., Yang, H. T., Li, D. (2021). Decentralized V2G/G2V scheduling of EV charging stations by considering the conversion efficiency of bidirectional chargers. *Energies*, 14, 4, 962.
- [14] Solar Energy (2022). Energy efficiency & renewable energy, from <https://www.energy.gov/eere/solar/how-does-solar-work> [Access Date: 06.12.2022].
- [15] Kadeval, H. N., Patel, V. K. (2021). Mathematical modelling for solar cell, panel and array for photovoltaic system. *Journal of Applied and Natural Science*, 13, 3, 937-943.
- [16] K. Kachhiya, "MATLAB / Simulink Model of Solar PV Module and MPPT Algorithm," Natl. Conf. Recent Trends Eng. Technol., vol. 13, 2011, p. 5.
- [17] Mohammed, S. S., Devaraj, D. (2014). Simulation and analysis of stand-alone photovoltaic system with boost converter using MATLAB/Simulink. *International Conference on Circuits, Power and Computing Technologies [ICCPCT-2014]*, 814-821.
- [18] Singh, V. K., Sahu, Y., Mishra, P. K., Tiwari, P., Maurya, R. (2020). Charging of Electric Vehicles Battery Using Bidirectional Converter. *International Conference on Electrical and Electronics Engineering (ICE3)*, 82-88.
- [19] Khedekar, V. G., Anandh, N., Paragond, L. R. S., Kulkarni, P. (2019). Bidirectional on-board EV battery charger with V2H application. *Innovations in Power and Advanced Computing Technologies (i-PACT)*, 1, 1-5.
- [20] Salman, S., Ai, X., Wu, Z. (2018). Design of a P-&O algorithm based MPPT charge controller for a stand-alone 200W PV system. *Protection and Control of Modern Power Systems*, 3, 1, 1-8.
- [21] Rai, A. K., Kaushika, N. D., Singh, B., Agarwal, N. (2011). Simulation model of ANN based maximum power point tracking controller for solar PV system. *Solar Energy Materials and Solar Cells*, 95, 2, 773-778.
- [22] Premkumar, K., Manikandan, B. V. (2014). Adaptive Neuro-Fuzzy Inference System based speed controller for brushless DC motor. *Neurocomputing*, 138, 260-270.
- [23] Barker, T., Ghosh, A. (2022). Neural Network-Based PV Powered Electric Vehicle Charging Station. *IEEE Delhi Section Conference (DELCON)*, 1-6.
- [24] Güneşer, M. T., Erdil, E., Cernat, M., Öztürk, T. (2015). Improving the energy management of a solar electric vehicle. *Advances in Electrical and Computer Engineering*, 15, 4, 53-62.